

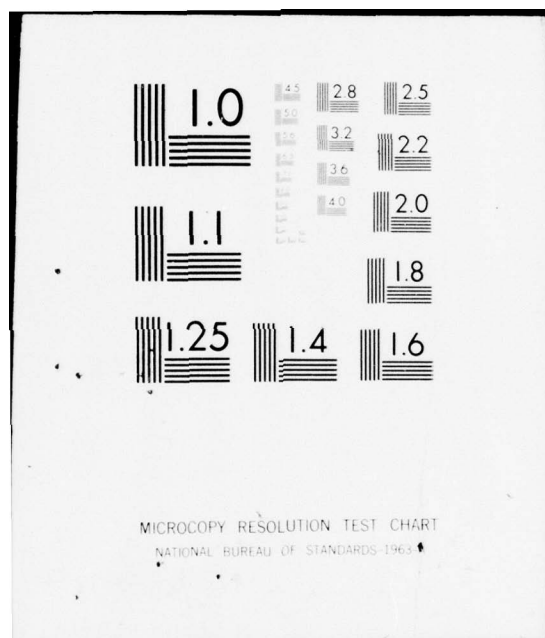
AD-A043 547

GENERAL RESEARCH CORP SANTA BARBARA CALIF
THE ROSCOE MANUAL, VOLUME 17. HIGH-ALTITUDE DEBRIS-ENERGY DEPOS--ETC(U)
SEP 75 D A HAMLIN, J Y WANG, M R SCHOONOVER DNA001-74-C-0182
DNA-3964F-17 NL

UNCLASSIFIED

1 OF 2
AD
A043547





ADA043547

12

DNA 3964F - 17

THE ROSCOE MANUAL

Volume 17 - High Altitude Debris-Energy Deposition

Science Applications, Inc.
P. O. Box 2351
La Jolla, California 92038

22 September 1975

Final Report for Period 1 March 1974-31 January 1975

CONTRACT No. DNA 001-74-C-0182

APPROVED FOR PUBLIC RELEASE;
DISTRIBUTION UNLIMITED.



THIS WORK SPONSORED BY THE DEFENSE NUCLEAR AGENCY
UNDER RDT&E RMSS CODES B322074464 S99QAXHC06428 AND
B322075464 S99QAXHC06432 H2590D.

DDC FILE COPY

Prepared for

Director

DEFENSE NUCLEAR AGENCY

Washington, D. C. 20305

Destroy this report when it is no longer
needed. Do not return to sender.



UNCLASSIFIED

SECURITY CLASSIFICATION OF THIS PAGE (When Data Entered)

19 REPORT DOCUMENTATION PAGE		READ INSTRUCTIONS BEFORE COMPLETING FORM
1. REPORT NUMBER DNA 3964F-17	2. GOVT ACCESSION NO.	3. RECIPIENT'S CATALOG NUMBER
4. TITLE (and Subtitle) THE ROSCOE MANUAL Volume 17—High-Altitude Debris-Energy Deposition	5. TYPE OF REPORT & PERIOD COVERED Final Report for Period 1 Mar 74—31 Jan 75	
7. AUTHOR(s) Daniel A. Hamlin Melvin R. Schoonover John I. Valerio	6. PERFORMING ORG. REPORT NUMBER SAI-75-609-LJ, Vol. 5	
9. PERFORMING ORGANIZATION NAME AND ADDRESS Science Applications, Inc. P.O. Box 2351 La Jolla, California 92038	8. CONTRACT OR GRANT NUMBER(s) DNA 001-74-C-0182	
11. CONTROLLING OFFICE NAME AND ADDRESS Director Defense Nuclear Agency Washington, D.C. 20305	10. PROGRAM ELEMENT, PROJECT, TASK AREA & WORK UNIT NUMBERS NWED Subtasks S99QAXHC064-28/32	
14. MONITORING AGENCY NAME & ADDRESS (if different from Controlling Office)	12. REPORT DATE 22 September 1975	
	13. NUMBER OF PAGES 126	
	15. SECURITY CLASS (of this report) UNCLASSIFIED	
15a. DECLASSIFICATION DOWNGRADING SCHEDULE		
16. DISTRIBUTION STATEMENT (of this Report) Approved for public release; distribution unlimited.		
17. DISTRIBUTION STATEMENT (of the abstract entered in Block 20, if different from Report)		
18. SUPPLEMENTARY NOTES This work sponsored by the Defense Nuclear Agency under RDT&E RMSS Codes B322074464 S99QAXHC06428 and B322075464 S99QAXHC06432 H2590D.		
19. KEY WORDS (Continue on reverse side if necessary and identify by block number) ROSCOE Radar Blackout Code Energy Deposition by X-Rays Energy Depositions by Ultraviolet Radiation Energy Deposition by Debris Particles (Loss-Cone, Ion-Leak, and Charge Exchange)		
20. ABSTRACT (Continue on reverse side if necessary and identify by block number) Models of the high-altitude debris-energy partition and deposition have been adopted for use in ROSCOE. The models for the debris-energy partition and heavy-particle source spectra incorporate the work of Crevier and Kilb for the loss-cone and ion-leak particles. The determi- nation of the total (and spectrum of the) UV portion of the kinetic yield remaining after that assigned to all the heavy-particle motion is based on the work of Fajen and Sappenfield. Representative points in the spatial		

DD FORM 1 JAN 73 1473 EDITION OF 1 NOV 65 IS OBSOLETE

UNCLASSIFIED

SECURITY CLASSIFICATION OF THIS PAGE (When Data Entered)

402754

Jmic

UNCLASSIFIED

SECURITY CLASSIFICATION OF THIS PAGE(When Data Entered)

18. SUPPLEMENTARY NOTES (Continued)

EDITORS NOTE

Volumes 13 to 17 were originally published by SAI to describe the atmospheric, geomagnetic, and high-altitude energy deposition and neutral heave models for ROSCOE. This whole section of code, when associated with an appropriate DRIVER subroutine, operated as a package that ran independently of the rest of the ROSCOE structure. Provision was also made, within this high-altitude package, for two completely independent descriptions of atmospheric heave, each with its own description of atmospheric chemistry.

When GRC incorporated this section of code within the ROSCOE framework, some modifications were necessary, which means that some of the descriptions in Volumes 13 to 17 are inappropriate to ROSCOE as it now exists. In particular, the NRL heave routines (deck NRLHYD) and associated chemistry (deck NRLCHM) are not presently used in ROSCOE. Three other subroutines are different: subroutines ATMOSU, EIF, and XTCOEf correspond to the ROSCOE subroutines ATMOS, EXPINT, and WDXP respectively. With these exceptions, the subroutines described in Volumes 13 to 17 correspond exactly to those currently in ROSCOE.

20. ABSTRACT (Continued)

distribution function specified for the loss-cone and ion-leak particles are used as effective source points through which magnetic field lines are traced in the downward direction through the intercepted grid cells in the geocentric quadrupole coordinate system. Conventional heavy-particle range-energy theory is employed along these paths, without regard to spiralling effects, to deposit the energy of these heavy particles in the traversed cells. Charge-exchange particles are deposited without regard to the magnetic field. The total heavy-particle energies deposited by inelastic and by elastic collisions in each cell are partitioned into various modes and species which are ultimately made compatible with the late-time grid chemistry. The UV energy groups, as well as the x-ray energy, are deposited by tracing ray paths (and constructing line integrals of relevant species) from the event point to each cell in the high-altitude grid treated as a target cell. The portion of all the deposited energy available for hydro is computed as well as the instantaneously-produced species to be used as starting conditions for the subsequent hydrodynamics and chemistry. Herein are presented details of the models for the debris-energy partition and deposition, including detailed flow charts for the more complicated routines.

UNCLASSIFIED

SECURITY CLASSIFICATION OF THIS PAGE(When Data Entered)

CONTENTS

	<u>Page</u>
1. CONTROL ROUTINE FOR DEPOSITION OF THE ENERGY IN THE HIGH-ALTITUDE GRID (SUBROUTINE PROMPG)	7
2. SOME AUXILIARY ROUTINES	12
2.1 Subroutine BOUNDY	12
2.2 Subroutine INDEX	13
2.3 Subroutine PROPTY	13
3. DEBRIS ENERGY PARTITION AND PARTICLE-SOURCE SPECTRA	15
3.1 Introduction	15
3.2 Hydro-Energy Partitioning	16
3.2.1 Loss-Cone Energy	17
3.2.2 Ion-Leak Energy	18
3.2.3 CHEX Energy	20
3.2.4 Residual Energy for UV and Thermal Modes	23
3.3 Particle Energy Distribution	23
3.3.1 Loss-Cone Spectrum	23
3.3.2 Ion-Leak Spectrum	26
3.3.3 CHEX Spectrum	27
4. UV SOURCE CHARACTERISTICS	28
5. X-RAY SOURCE CHARACTERISTICS AND ENERGY DEPOSITION	30
6. DEPOSITION OF DEBRIS PARTICLES	32
6.1 Introduction	32
6.2 Heavy-Particle Energy Loss	32
6.3 Energy Deposition Over a Distribution Function	35

RE: Classified references-
DNA-3964F-17
Document should remain for unlimited
distribution per Mrs. McCleary, DNA

	<u>Page</u>
6.4 Practical Implementation	35
6.4.1 Histogram Representation	36
6.4.2 Loss-Cone Histogram	37
6.4.3 Ion-Leak Histogram	37
6.4.4 CHEX Histogram	38
6.5 Particle Spatial Distributions	38
6.5.1 Representation of the Spatial Distribution at 100-km Altitude	39
6.5.2 Particle Allocations	41
6.6 Starting Coordinates of the Field Lines	42
6.7 Field-Line Tracing	45
6.8 Loss-Cone and Ion-Leak Particle Deposition	46
6.9 CHEX-Particle Deposition	47
7. PARTITIONING OF THE DEPOSITED DEBRIS ENERGY AND CONSEQUENT SPECIES (SUBROUTINE HPCHEM)	49
8. ORGANIZATION OF THE HEAVY-PARTICLE RELATED ROUTINES	60
9. UV DEPOSITION	74
9.1 Computation of Ray Paths Through the HAG (Subroutine PLINE)	74
9.1.1 Introduction	74
9.1.2 Transformation from the Quadrupole Coordinate System to the Associated Geocentric Cartesian System	75
9.1.3 Cell Shape	77
9.1.4 Basic Formulas for Slant Range from a Given Point to a Cell Boundary	77
9.1.5 A Caution for Energy Deposition in the Event-Point Cell	80
9.1.6 Directional Flags and Indices of Next Set of Boundaries to be Intersected	83
9.1.7 Flow Charts of Subroutine PLINE	84
9.1.8 Miscellaneous Functions of Subroutine PLINE	84

	<u>Page</u>
9.2 Computation of Integrals of Species Number Densities and Mass Densities Along the Ray Path (Subroutine PINT)	84
9.3 Computation of the Atomic-Ion Region (B-Edge) for Group-U Photons (Subroutine BEDGE)	90
9.3.1 Introduction	90
9.3.2 Simplified Description of the Essence of Subroutine BEDGE	90
9.3.3 Flow Charts of Subroutine BEDGE	92
9.4 Computation of Group-U Subgroup Fluences and Prompt Heating (Subroutine PHEAT)	92
9.4.1 Group-U Energy Deposition and Fluences	97
9.4.2 Pressure to be Used for Hydro	101
9.4.3 Flow Chart for Subroutine PHEAT	102
10. PROMPT CHEMISTRY ASSOCIATED WITH GROUP-X AND GROUP-U ENERGY DEPOSITION (SUBROUTINE PCHEM).	105
10.1 Determination of Initial Species for Computing the Prompt Chemistry Associated with Group-X and Group-U Energy Depositions	105
10.2 Ionization and Species Densities from Group-X Deposition	108
10.3 Ionization, Species Densities, and Resultant Pressure from Group-U Deposition	114
11. REFERENCES	121

ILLUSTRATIONS

	<u>Page</u>
1. Simplified Flow Chart for Subroutine PROMPG Which Controls the Energy-Deposition Routines	4
2. Simplified Flow Chart for the Subroutine PROMPG Triple DO-Loop Over All Cells in the High-Altitude Grid	11
3. Illustration of the Order of Partitioning of the Total Kinetic Yield into Loss-Cone, Ion-Leak, CHEX, and UV-plus-Thermal Energies	16
4. Fraction of the Total Kinetic Yield Escaping the Event-Point Region by the Loss-Cone Mechanism, for Several Event Altitudes	19
5. Fraction of the Total Kinetic Yield Escaping the Event-Point Region by the Ion-Leak Mechanism, for Several Event Altitudes	21
6. Fraction of Total Kinetic Yield Escaping the Event-Point Region by the Charge-Exchange Mechanism, for Several Event Altitudes	24
7. Fraction of the Total Kinetic Yield Remaining for the UV and Thermal Modes (f_R) After the Subtraction of the Loss-Cone, Ion-Leak, and Charge-Exchange Fractions	25
8. Four Annular Rings, Four Characteristic Circles, and 21 Representative Points Used to Approximate the Radial Distribution of Downward-Moving Loss-Cone and Ion-Leak Energies	43
9. Simplified Flow Chart of Debris-Related Routines	61
10. Flow Chart for Subroutine BLINE(NXCEL, RR)	64
11. Flow Chart for Subroutine DEPO(ZETA, DIV, ANEE, ANEI) . . .	70
12. Flow Chart for Subroutine CHXDEP(NCEL)	72
13. Diagram Illustrating the Transformation from the Quadrupole Coordinate System to the Corresponding Geocentric Cartesian System	76

	<u>Page</u>
14. Geometry Used in Deriving Slant Range of a Ray Intersecting a Cell Top- or Bottom-Boundary	79
15. Geometry Used in Deriving Slant Range of a Ray Inter- secting a Cell North- or South-Boundary (Specified by Quadrupole Colatitude θ_2	81
16. Geometry Used in Deriving Slant Range of a Ray Intersecting a Cell East- or West-Boundary (Specified by Quadrupole East Longitude θ_2)	82
17. Simplified Flow Chart of Subroutine PLINE, Including Calls to Subroutines PINT and BEDGE	85
18. Simplified Flow Chart of Subroutine PLINE	86
19. Simplified Flow Chart of Subroutine BEDGE	93
20. Detailed Flow Chart of Subroutine BEDGE	94
21. Flow Chart of Subroutine PHEAT	103
22. Flow Chart of Subroutine PCHEM	109

TABLES

	<u>Page</u>
1. Radii of Annular Rings and Characteristic Circles Used to Approximate the Radial Distribution Function of Downward-Moving Loss-Cone and Ion-Leak Energies	42
2. Heavy-Particle Prompt-Chemistry Reactions from Inelastic and Elastic Collisions	50
3. Inputs to Subroutine PCHEM from BUF2 Array for Those Cell Quantities Updated by Subroutine HPCHEM as a Result of Debris Deposition	106
4. UV Absorption Cross-Sections SIGU(L, J)	116

1. CONTROL ROUTINE FOR DEPOSITION OF THE ENERGY IN THE HIGH-ALTITUDE GRID (SUBROUTINE PROMPG)

Subroutine PROMPG, called by DRIVER, controls the deposition of the energy in the high-altitude grid (HAG). The overall procedure is complicated, as Subroutine PROMPG directly calls 12 subroutines which in turn call an additional 26 subroutines. The tasks performed by Subroutine PROMPG include the following:

a. Tests whether or not the event point is above the bottom of the grid. If it is, the program proceeds to the next task; if not, the program returns to DRIVER after printing an appropriate message. It may be desirable to deposit at least the Group- γ and possibly the Group-X energy for certain events below the bottom of the grid, but this feature has not been implemented yet.

b. Calls Subroutine BOUNDY to set up the array GR(NCEL) for the geocentric radius to the top boundary of each cell NCEL in the HAG. Subroutine BOUNDY is different in SAIHYD than in NRLHYD because the definitions of a cell boundary are different in the two versions of the hydrodynamics.

c. Sets up the array RHOKK(NCEL) for the mass density of each cell in the HAG by appropriately calling Subroutine ECRD to get successive columns.

d. Changes the geographic location of the event point by a small amount so that if the event point is inputted on a cell boundary, as it would be if it were placed, e. g., at the origin of the quadrupole coordinate system, the event point would be moved off the boundary to facilitate the code's assigning the event point to the proper cell in the

grid. This movement of the event point is made by (1) converting the geographic coordinates of the event point to quadrupole coordinates by calling Subroutine GEOQUA, (2) multiplying the quadrupole coordinates by the fraction 0.999997 to obtain the new quadrupole coordinates, and (3) converting the new quadrupole coordinates to geographic coordinates by calling Subroutine QUAGEO.

e. Calls Subroutine INDEX to obtain the indices (IEC, JEC, KEC) of the event cell and the vertical fractional-position parameter (FRACB) for the event point within the event cell. Again, Subroutine INDEX is different in SAIHYD than in NRLHYD. The event-point indices are printed and stored in EVENTX Common as members of arrays.

f. Calls Subroutine PROPTY to obtain, print, and store in array PP(7) the following event-point properties: mass density, mass-density scale height, heavy-particle temperature, and magnetic-field strength, dip angle, declination angle, and dipole colatitude.

g. Moves the event point slightly away from the center or boundary of a cell if either of the quadrupole coordinates or the geocentric radius of the event point differs from that of the cell center or boundary by less than the fraction 10^{-5} . The new coordinate is made to differ from the cell-center or boundary coordinate by the fraction 3×10^{-5} .

h. Computes the geocentric cartesian coordinates (X1, Y1, Z1) of the event point, given the quadrupole coordinates and the geocentric radius of the event point. The Z-axis is through the quadrupole north pole; the X-axis is through the quadrupole west pole.

i. Calls Subroutine DEBRIS which serves as the principal control routine for computing the partitioning and deposition of the Group-D (debris) energy. Subroutine DEBRIS controls 16 subroutines, including direct calls to Subroutines HDPART, CONSPC, LEKSPC, CHXSPC, and BLINE.

j. Sets up the Group-U (ultraviolet) properties by (1) calling Subroutine EUXFIT to get the energy in each of the five Subgroups L, (2) establishing pressure efficiencies PREFF(L,I) for Subgroup-L photons incident on Species I, and (3) establishing absorption coefficients XMU1 of O₂ for Subgroup 1 of Group U. (These latter two functions should probably be done elsewhere.) The calculated pressure efficiencies follow the somewhat arbitrary assumption in FS-73 that all photoelectron kinetic energies below 10 eV, and 0.80 of the kinetic energy of photoelectrons more energetic than 10 eV, are thermalized; the remaining energy is discarded, as having been lost in radiative processes.

k. Computes the deposition of the Group-X (x ray), Group-U, and Group-CHEX (charge exchange) energies by making a triple DO-loop over all the cells in the HAG, during which calls are made to the following subroutines:

- PLINE - Computes line integrals, with aid of Subroutines PINT and BEDGE.
- CHXDEP - Computes deposition of CHEX energy.
- HPCHEM - Computes prompt chemistry due to Group-D energy deposition.
- PHEAT - Computes heating due to Group-D, -X, and -U energies.
- PCHEM - Combines results of Subroutines HPCHEM with prompt chemistry due to Groups X and U.

l. Stores in array BUF those cell quantities updated in Subroutine PCHEM and stored in the temporary scratch area.

Figure 1 is a simplified flow chart that summarizes the functions performed by Subroutine PROMPG. Figure 2 is a simplified flow chart of the triple DO-loop within Subroutine PROMPG that loops over all cells in the HAG.

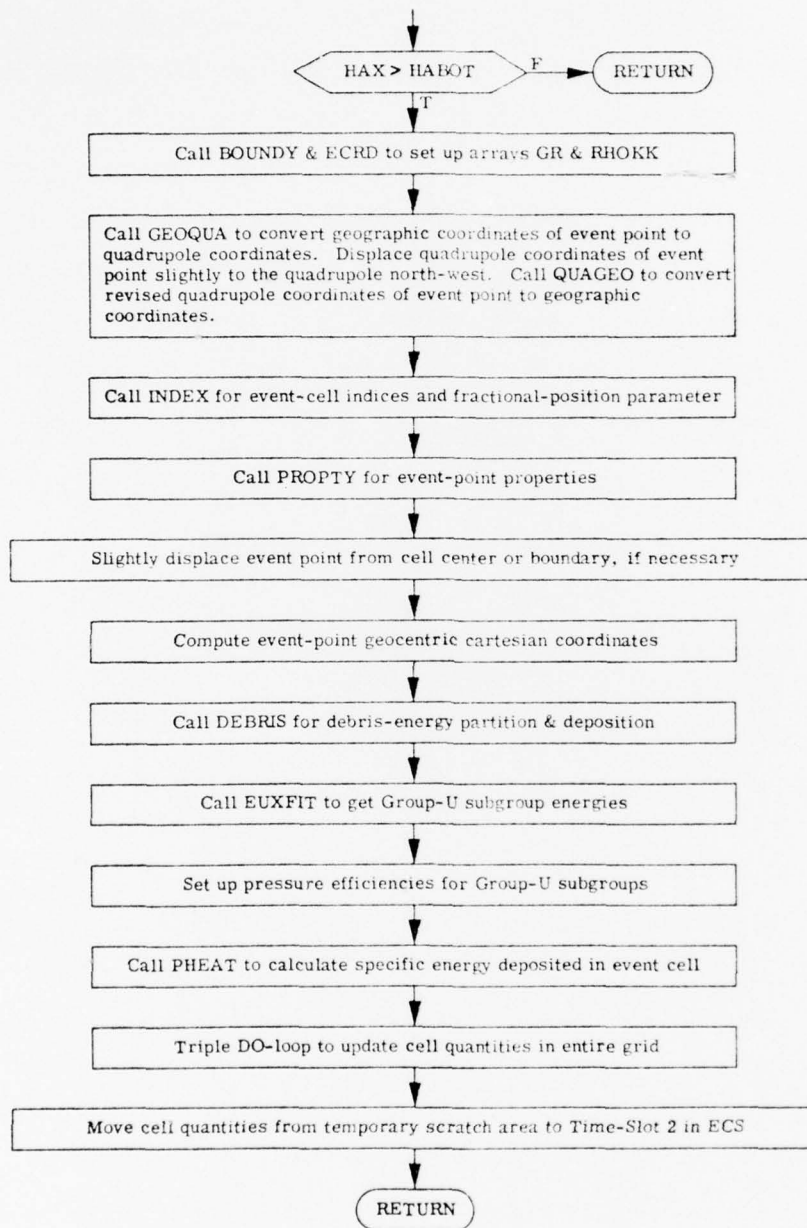


Fig. 1. Simplified Flow Chart for Subroutine PROMPG Which Controls the Energy-Deposition Routines.

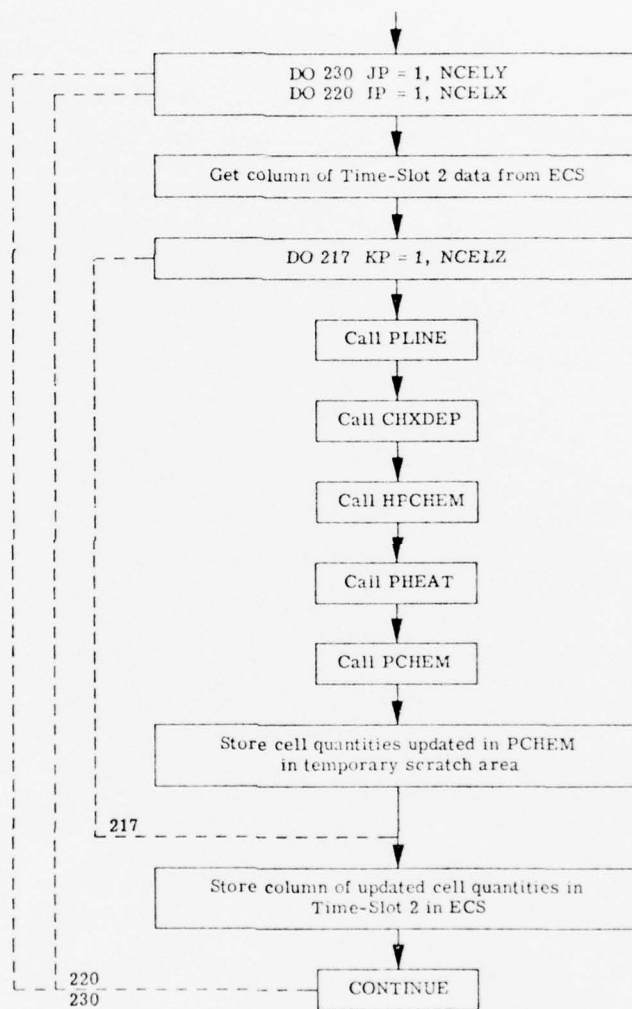


Fig. 2. Simplified Flow Chart for the Subroutine PROMPG Triple DO-Loop Over All Cells in the High-Altitude Grid.

2. SOME AUXILIARY ROUTINES

2.1 SUBROUTINE BOUNDY

Subroutine BOUNDY establishes a one-dimensional array GR(NCEL) of the geocentric radii to all the cell top-boundaries in the HAG. This information is developed by using the cell-center heights stored as cell properties and obtained by calling Subroutine ECRD.

Subroutine BOUNDY is different in SAIHYD and NRLHYD. As discussed in Volume 16, the differential-quadrature formulation of the Lagrangian hydrodynamics (NRLHYD) does not employ the concept of a cell in computing the hydrodynamic motion, as is done in the difference-equation formulation of the Lagrangian hydrodynamics (SAIHYD). However, the deposition of energy (in SAIROS) has been formulated in terms of a cellular grid for use with SAIHYD. To make use of this energy deposition procedure with NRLHYD, it is necessary to establish cells and cell boundaries in NRLHYD to correspond to the same quantities in SAIHYD. Subroutine BOUNDY in NRLHYD establishes such cell boundaries.

For N Lagrangian points (initially specified in Subroutine ATMOSG to be at the N-1 SAIHYD cell centers plus one more point at the SAIHYD grid bottom), the N-1 interior boundaries are defined to be midway between the adjacent Lagrangian points. For the top cell, the outer boundary is placed so that the top Lagrangian point is at the center of the top cell. The parameter HABOT, originally read in by DRIVER in SETUP1 as the bottom of the grid for SAIHYD, is reset in ATMOSG to be the bottom boundary of the lowest NRLHYD cell. Since the value of HABOT is not allowed to change with time, the bottom Lagrangian point does not remain at the center of the bottom cell despite its not moving.

2.2 SUBROUTINE INDEX

For a given Point X in geographic coordinates (GCX, GLX), Subroutine INDEX calls Subroutine GEOQUA to compute the quadrupole coordinates (QCX, Q LX) of the point. Subroutine INDEX then finds the indices IX, JX, and KX of the Point X. If the Point X is to the quadrupole-north of, quadrupole-west of, or below the grid boundary, index IX, JX, or KX is set equal to zero. If the Point X is to the quadrupole-south of, quadrupole-east of, or above the grid boundaries, the index IX, JX, or KX is set equal to (NCELX+1), (NCELY+1), or (NCELZ+1), respectively, and an appropriate warning message is printed. Subroutine INDEX also computes the fractional-height position of the Point X within the cell at the time the subroutine is called.

If the Point X is on a quadrupole colatitude or east longitude boundary, Subroutine INDEX identifies Point X as being in the cell for which the boundary is the south or east boundary of the cell.

The version of Subroutine INDEX used with NRLHYD differs from that used with SAIHYD mainly in that (1) the vertical-direction index (KX) has a plus or minus sign associated with it to denote whether the Point X is above or below the Lagrangian Point KX, respectively, and (2) the fractional-height parameter refers to the fractional distance between the two adjacent Lagrangian points instead of the fractional distance within the cell (with both fractional distances being measured upward from the bottom).

2.3 SUBROUTINE PROPTY

Subroutine PROPTY computes the mass density [PP(1)], the density scale height [PP(2)], and the heavy-particle temperature [PP(3)] of a given Point X inside the HAG. By calling Subroutine BFIELD,

Subroutine PROPTY also obtains the local dip angle [PP(4)], declination angle [PP(5)], strength [PP(6)], and cosine of the dipole colatitude [PP(7)] of the dipole magnetic field line passing through the point.

3. DEBRIS ENERGY PARTITION AND PARTICLE-SOURCE SPECTRA

3.1 INTRODUCTION

Certain overall partitioning of the total yield for three selected devices is given by Knapp et al. [in Volume 12] as part of the GET ROSCOE Model 3. This partitioning includes statements for the fractional yields of x rays and hydrodynamics. The additional partitioning of the hydrodynamics yield into several types of heavy-particle emissions and UV emission, needed for computing the energy deposition in the HAG, is not completely understood. We have, of necessity, adopted a specific procedure, but it certainly deserves review and improvement.

It is convenient to classify the heavy-particle emission from the expanding weapon debris-air mixture into loss-cone, ion-leak, and charge-exchange (CHEX) particles even though the division among these three groups is not unique. For our purposes, we consider loss-cone particles to be debris ions that escape the burst region along the magnetic field direction. Ion-leak particles are also emitted along magnetic field lines but they are composed mainly of air ions heated by the weapon debris expansion. CHEX particles are mainly fast neutral air atoms born through ion-to-neutral charge-exchange reactions within the debris-air mixture.

Partitioning of the weapon kinetic yield into loss-cone and ion-leak energies follows the prescription given by Crevier and Kilb [in Volume 10] as part of the MRC ROSCOE Model 12a. The fraction of the remaining kinetic yield emitted as CHEX particles is computed from the RANC-IV formulation [GE-70]. Thus, the sum of the loss-cone, ion-leak, and charge-exchange yields is subtracted from the total

hydrodynamic yield before the UV yield is determined by the prescription of Fajen and Sappenfield [FS-71a, FS-73]. We do not discuss the physical validity of our modeling of the hydro-yield partitioning; we do discuss and provide Fortran energy-deposition routines. Hopefully, future modifications of the hydro-yield partitioning will require only minor modifications of these routines.

3.2 HYDRO-ENERGY PARTITIONING

Partitioning of the weapon kinetic yield is summarized in Fig. 3; the directed dashed line shows the computational order. The energy indicated in each energy block is successively subtracted from the remaining energy until the residual UV-plus-thermal energy is obtained. The partitioning into the three heavy-particle modes is performed by calls from Subroutine HDPART to Subroutines LOSCON, IONLEK, and CHXLOS. The final division into UV and thermal energies is performed in Subroutine EUXFIT.

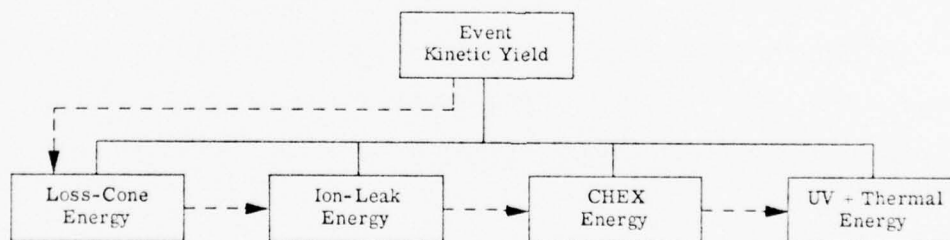


Fig. 3. Illustration of the Order of Partitioning of the Total Kinetic Yield into Loss-Cone, Ion-Leak, CHEX, and UV-plus-Thermal Energies.

3.2.1 Loss-Cone Energy

The energy fraction in the loss cones, with neglect of collisions, is [Vol. 10, Eq. (2-23)]

$$F_{\ell c} = 1 - (1 - \epsilon_1)^{\frac{5}{2}} - \left[2 - (1 - \epsilon_1)^{\frac{5}{2}} (2 + \epsilon_1 - 3\epsilon_1^2) \right] / 5\epsilon \quad (1)$$

where

$$\epsilon = \frac{1.40 \times 10^{-20}}{B^2} \left[\frac{v_d^5 n_a}{W_K Z_d^{5/2} Z_a^{1/2}} \right]^{(2)} \quad , \quad [\text{Vol. 10, Eq. (2-26)}] \quad (2)$$

and

$$\epsilon_1 = \min(\epsilon, 1) \quad . \quad [\text{Vol. 10, Eq. (2-22)}] \quad (3)$$

Here, W_K is the weapon kinetic energy in MT, B is the burst-point magnetic field in gauss, v_d is the debris velocity in cm/sec, n_a is the air-ion density in cm^{-3} , Z_d is the debris-ion charge state, and Z_a is the air-ion charge state. However, with collisions included, the energy in MT leaving the burst region in the downward direction is given by [Vol. 10, p. 14]

$$W_{\ell cd} = \frac{1}{2} W_K F_{\ell c} \left[\max \left\{ 0, \left[1 - (\rho_a / 2 \times 10^{-12})^2 \right] \right\} \right] \quad , \quad (4)$$

where ρ_a is the burst-point mass density, and the energy leaving in the upward direction is given by [Vol. 10, p. 14]

$$W_{\ell cu} = \frac{1}{2} W_K F_{\ell c} \left[\max \left\{ 0, \left[1 - (\rho_a / 2 \times 10^{-11})^2 \right] \right\} \right] \quad . \quad (5)$$

The total energy in MT leaving the burst region through the loss cones is [Vol. 10, Subroutine LOSCON]

$$W_{\ell c} = W_{\ell cd} + W_{\ell cu} \quad . \quad (6)$$

For more information about this formulation the reader is referred to ,
Volume 10.

The total fraction of the weapon kinetic energy (with collisions included) leaving the burst region in the loss cones is

$$f_{\ell c} = W_{\ell c} / W_K \quad (7a)$$

which, for burst-point densities less than $\rho_a \approx 2 \times 10^{-12} \text{ g/cm}^3$, is very nearly equal to the fraction $F_{\ell c}$ for neglect of collisions. For the downward direction the fraction corresponding to $f_{\ell c}$ is

$$f_{\ell cd} = W_{\ell cd} / W_K \quad (7b)$$

For $\rho_a < 2 \times 10^{-12} \text{ g/cm}^3$,

$$f_{\ell cd} \approx 0.5 f_{\ell c} \quad (8)$$

In Fig. 4 we have plotted $f_{\ell c}$ as a function of the kinetic yield W_K . The curves have been drawn through points computed from the Subroutine LOSCON given in Vol. 10 and used in SAIROS. The altitudes correspond to densities from the CIRA-1965 Model-5 8-hr atmosphere [CI-65]; we used $B = 0.5$ gauss. For the 150-km curve, $f_{\ell cd} = 0$.

3.2.2 Ion-Leak Energy

The energy in MT moving downward from the burst region due to the ion-leak mechanism is [Vol. 10, Eq. (3-1)]

$$W_{i\ell d} = 0.45 W_1 \left[1 - \left(\rho_a / 2 \times 10^{-12} W_1^{\frac{1}{3}} \right)^{0.04 / (W_1^{0.4})} \right] \quad (9)$$

where W_1 , given by

$$W_1 = W_K - W_{\ell c} \quad (10)$$

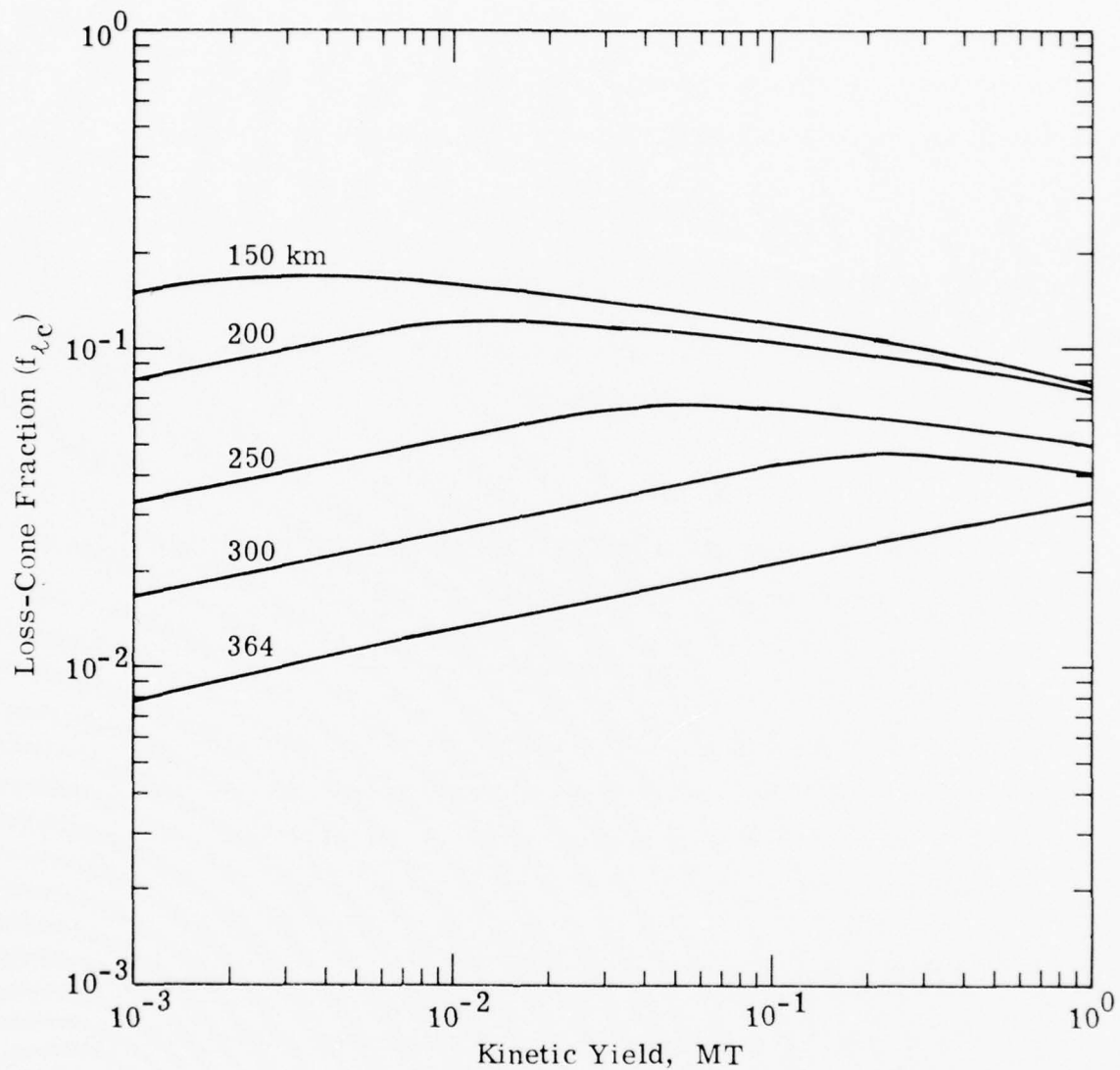


Fig. 4. Fraction of the Total Kinetic Yield Escaping the Event-Point Region by the Loss-Cone Mechanism, for Several Event Altitudes. Curves are drawn for $B = 0.5$ gauss and the CIRA-65 mean atmosphere. At 150-km, the downward fraction $f_{l,cd}$ is zero.

is the kinetic yield left after the loss-cone energy is removed. No statement is made in Vol. 10 about the magnitude of the upward-moving ion-leak energy. Since we must know the amount lost by this mechanism in all directions to estimate the kinetic yield left for subsequent yield partitioning, we arbitrarily set the total ion-leak energy loss as

$$W_{i\ell} = 2 W_{i\ell d} . \quad (11)$$

Final determination of $W_{i\ell}$ must be deferred to some future date.

The total fraction of the weapon kinetic energy leaving the burst region by the ion-leak mechanism is

$$f_{i\ell} = W_{i\ell}/W_K . \quad (12)$$

By our simplifying assumption in Eq. (11), we see that the fraction for the downward direction is

$$f_{i\ell d} = 0.5 f_{i\ell} . \quad (13)$$

In Fig. 5 we have plotted $f_{i\ell}$ as a function of the kinetic yield W_K . The curves have been drawn through points computed from the Subroutine IONLEK given in Vol. 10 and used in SAIROS. We used the same input conditions as for Fig. 4.

3.2.3 CHEX Energy

Time constraints did not allow us to develop a new model for the energy leaving the burst region via fast neutrals produced through charge exchange. As an interim procedure we have just applied the RANC IV model [GE-70] to the remaining kinetic yield so that a place for CHEX particles might be formally introduced in the code.

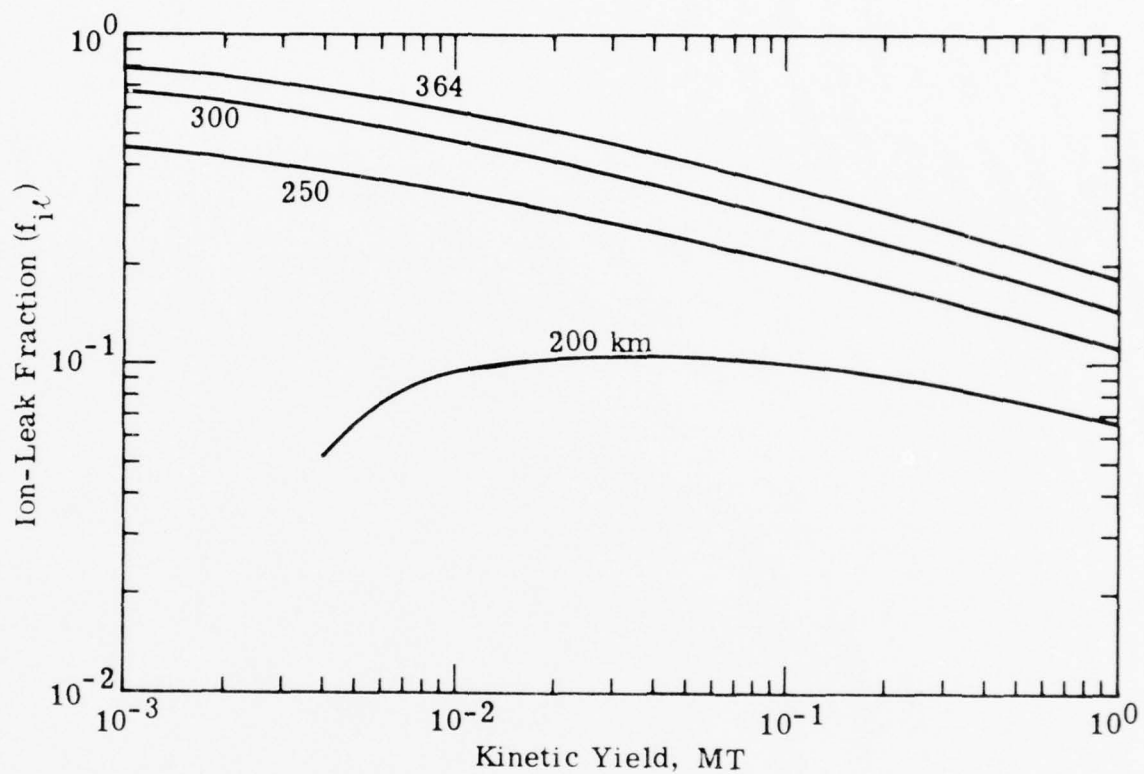


Fig. 5. Fraction of the Total Kinetic Yield Escaping the Event-Point Region by the Ion-Leak Mechanism, for Several Event Altitudes. Curves are drawn for $B = 0.5$ gauss and the CIRA-65 mean atmosphere. By our assumption the downward fraction f_{ild} equals $0.5 f_{il}$.

The RANC IV prescription for CHEX-particle energy emission (in MT), adapted to our needs, is

$$W_{\text{chex}} = \frac{1}{6} (F_{\text{CED}} + F_{\text{CEU}} + 4 F_{\text{CE}}) W_2 \quad (14a)$$

$$W_2 = W_K - W_{\ell c} - W_{i\ell} , \quad (14b)$$

where F_{CED} , F_{CEU} , and F_{CE} are coefficients associated with the downward, upward, and horizontal directions, respectively. In terms of the burst-point mass density ρ_a , their values are

$$F_{\text{CED}} = \begin{cases} 0.0 & \rho_a \geq 3 \times 10^{-13} \\ 10^{-15}/\rho_a & 3 \times 10^{-15} \leq \rho_a < 3 \times 10^{-13} \\ -0.27 \ln(10^{14} \rho_a) & 2.6 \times 10^{-16} < \rho_a < 3 \times 10^{-15} \\ 0.98 & \rho_a \leq 2.6 \times 10^{-16} \end{cases} \quad (15a)$$

$$F_{\text{CEU}} = \begin{cases} 0.25 \times 10^{-13}/\rho_a & \rho_a > 4.65 \times 10^{-14} \\ 0.25 \times 10^{14} \rho_a & \rho_a \leq 4.65 \times 10^{-14} \end{cases} \quad (15b)$$

$$F_{\text{CE}} = \begin{cases} 3 \times 10^{-15}/\rho_a & \rho_a \geq 3.16 \times 10^{-15} \\ 0.95 & 1.15 \times 10^{-15} \leq \rho_a < 3.16 \times 10^{-15} \\ 0.2 \ln(10^{17} \rho_a) & 10^{-17} < \rho_a < 1.15 \times 10^{-15} \\ 0.0 & \rho_a \leq 10^{-17} \end{cases} \quad (15c)$$

The fraction of the weapon kinetic energy leaving the burst region by the charge-exchange mechanism is

$$f_{\text{chex}} = W_{\text{chex}}/W_K . \quad (16)$$

In Fig. 6 we have plotted f_{chex} as a function of the kinetic yield W_K . We question the validity of the predicted CHEX emission for events below 150 km. Some modification of the model at low altitudes is clearly required.

3.2.4 Residual Energy for UV and Thermal Modes

After subtraction of the energies in the loss-cone, ion-leak, and CHEX particles, we obtain the energy left for the production of UV-photon and thermal energies. If the residual energy is given (in MT) by

$$W_R = W_K - W_{\ell c} - W_{i\ell} - W_{\text{chex}} , \quad (17)$$

then the fraction of the kinetic yield available is

$$f_R = W_R / W_K . \quad (18)$$

The fraction of the weapon kinetic energy available for the UV and thermal modes is plotted in Fig. 7 as a function of the kinetic yield W_K .

3.3 PARTICLE ENERGY DISTRIBUTION

Each source of fast heavy-particles has a different energy distribution. We record the distributions presently used.

3.3.1 Loss-Cone Spectrum

The velocity distribution of downward-going loss-cone particles is assumed to be [Vol. 10, Eq. (4-4)]

$$\frac{dW}{dv} = \frac{5 W_{\ell cd} v^4}{v_2^5 - v_1^5} \text{ (MT sec cm}^{-1}\text{)} . \quad (19a)$$

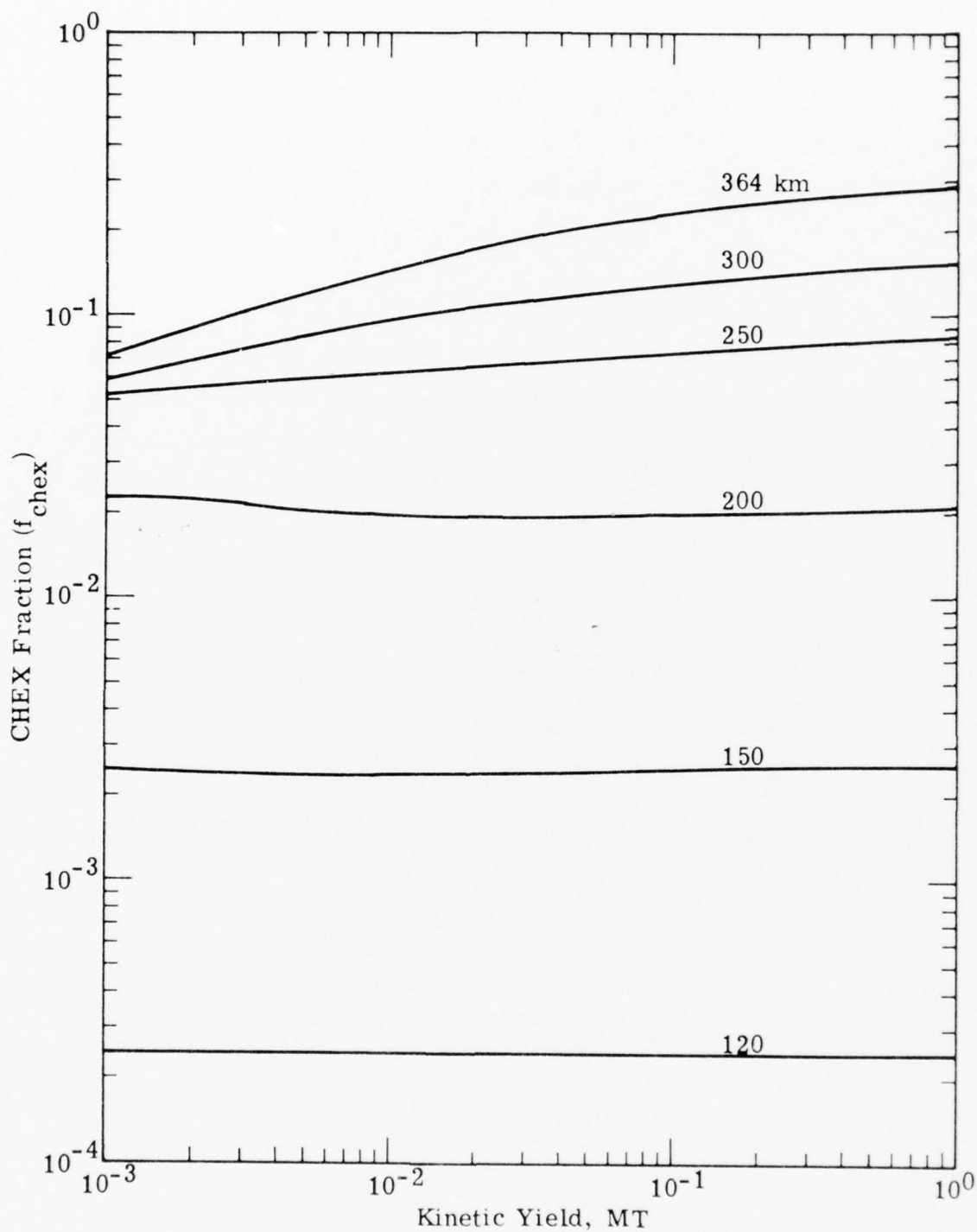


Fig. 6. Fraction of Total Kinetic Yield Escaping the Event-Point Region by the Charge-Exchange Mechanism, for Several Event Altitudes. Curves are drawn for the same conditions as in Figs. 4 and 5.

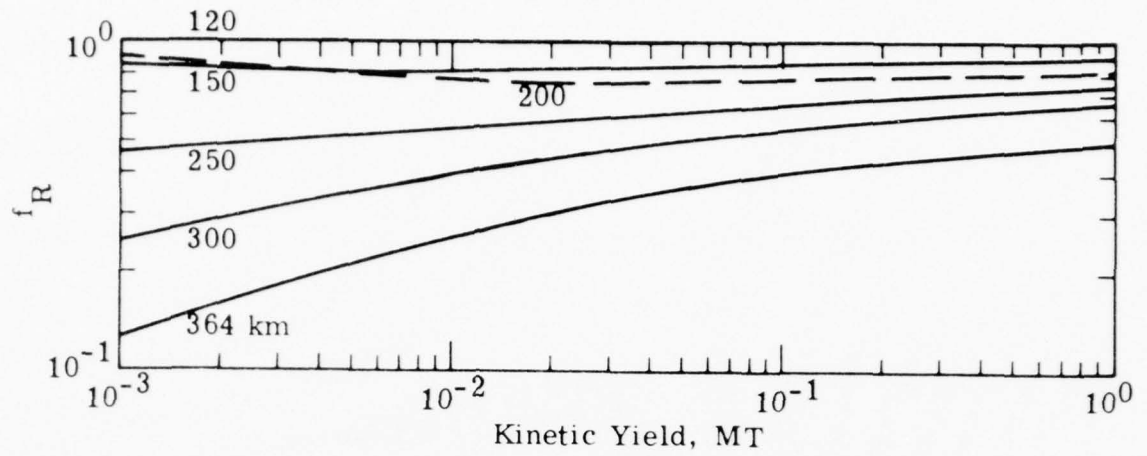


Fig. 7. Fraction of the Total Kinetic Yield Remaining for the UV and Thermal Modes (f_R) After the Subtraction of the Loss-Cone, Ion-Leak, and Charge-Exchange Fractions. Curves are drawn for the same conditions as in Figs. 4, 5, and 6.

Equation (19a) is readily integrated to give an integral velocity distribution which may be transformed to an integral energy distribution,

$$\frac{W_{tcd}(\leq E)}{W_{tcd}} = \frac{E^{5/2} - E_{\min}^{5/2}}{E_{\max}^{5/2} - E_{\min}^{5/2}}, \quad (19b)$$

where

$$E_{\min} = \frac{1}{2} m_d v_1^2 \text{ (erg)} \quad (20a)$$

$$E = \frac{1}{2} m_d v^2 \text{ (erg)} \quad (20b)$$

$$E_{\max} = \frac{1}{2} m_d v_2^2 \text{ (erg)} \quad (20c)$$

$$v_1 = \max \{0, v_2 - 4 \times 10^7\} \text{ (cm/sec)} \text{ [Vol. 10, Eq. (4-3)]} \quad (20d)$$

$$v_2 = v_d + 2 \times 10^7 \text{ (cm/sec)} \quad [\text{Vol. 10, Eq. (4-3)}] \quad (20e)$$

$$v_d = 2.7 \times 10^8 W_K^{0.27} \text{ (cm/sec)}, \quad [\text{Vol. 10, Eq. (4-1)}] \quad (20f)$$

with m_d the debris-ion mass in grams and W_K the burst kinetic energy in MT.

3.3.2 Ion-Leak Spectrum

The velocity distribution of downward-going ion-leak particles is assumed to be [Vol. 10, Eq. (4-11)]

$$\frac{dW}{dv} = \frac{W_{i\ell d}}{v_2 - v_3} \text{ (MT sec cm}^{-1}\text{)} . \quad (21)$$

Equation (21) is readily integrated to give an integral velocity distribution which may be transformed to an integral energy distribution,

$$\frac{W_{i\ell d}^{(\leq E)}}{W_{i\ell d}} = \frac{E^{1/2} - E_{\min}^{1/2}}{E_{\max}^{1/2} - E_{\min}^{1/2}} \quad (22)$$

where

$$E_{\min} = \frac{1}{2} m v_3^2 \quad (23a)$$

$$E = \frac{1}{2} m v^2 \quad (23b)$$

$$E_{\max} = \frac{1}{2} m v_2^2 \quad (23c)$$

with m the ion-leak particle mass, v_2 given by Eq. (20e), and

$$v_3 = 1.5 \times 10^7 \text{ (cm/sec)} . \quad [\text{Vol. 10, Eq. (4-11)}] \quad (24)$$

3.3.3 CHEX Spectrum

The charge-exchange particle spectrum tends to vary widely with burst altitude, direction of emission, and the weapon expansion velocity. To satisfy our immediate needs we have assumed an exponential energy distribution. Examination of earlier work [HL-71, HM-72b] tends to lend support for this functional form. Explicitly, the integral energy spectrum is

$$\frac{W_{\text{chex}}(E)}{W_{\text{chex}}} = \frac{e^{-aE_{\text{min}}} - e^{-aE}}{e^{-aE_{\text{min}}} - e^{-aE_{\text{max}}}} \quad (25a)$$

with

$$a = 10^{-4} \text{ (eV)}^{-1} \quad (25b)$$

$$E_{\text{min}}(\text{eV}) = \frac{m (10^7)^2}{2 \times 1.6 \times 10^{-12}} \quad (25c)$$

$$E_{\text{max}}(\text{eV}) = \frac{m v_2^2}{2 \times 1.6 \times 10^{-12}} \quad (25d)$$

m corresponding to a mass-15 particle, and v_2 given by Eq. (20e).

4. UV SOURCE CHARACTERISTICS

We have adopted the HARC-code prescription, given in our Subroutine EUXFIT, for the UV spectrum as a function of the event-point density and kinetic energy. This prescription, based on calculations by Fajen and Sappenfield [FS-71a, Table IV; FS-73], gives the fraction f_i ($i = 1, 5$) of the kinetic energy converted to UV in each of five spectral energy groups (with energy-bin edges at 0, 13.6, 15.6, 17, and 30 eV), according to the expression

$$f_i = (a_i x^2 + b_i x + c_i) y^2 + (d_i x^2 + e_i x + f_i) y + g_i x^2 + h_i x + p_i, \quad (26)$$

where

$$x = \ln K$$

$$y = \ln \rho$$

K (KT) = available kinetic energy

$\rho(\text{g/cm}^3)$ = event-point density .

Because of the approximate nature of the equations, the total fraction (FRU) is given [FS-71a] by Eq. (26) with another set of coefficients ($i = 7$ in the code). However, the code limits FRU to a maximum value of 0.98. If either f_i or FRU is negative for certain conditions, it is set equal to zero. The intended [FS-71a] range of validity of Eq. (26) is given by the expressions

$$8 \times 10^{-10} \leq \rho \leq 6 \times 10^{-14}$$

$$5 \leq K \leq 10^4 .$$

In the HARC Subroutine DSFIT, which we renamed EUXFIT after making minor changes, D. H. Sowle introduced a sixth energy group due to effective, low-energy x rays. The fraction f_6'' is given by

$$f_6'' = f_6' + \frac{\text{FRX} \times \text{EX}}{\text{EUX}}$$

where

$$f_6' = \frac{0.01}{0.01 + \sum_{i=1}^5 f_i} \frac{\text{FRU} \times \text{EH}}{\text{EUX}},$$

EH = K, EX is the x-ray energy, and EUX is the sum of the Group-U and an effective low-energy portion of Group X, given by

$$\text{EUX} = \text{FRU} \times \text{EH} + \text{FRX} \times \text{EX}.$$

Here, FRX is given by

$$\text{FRX} = \text{Max}[0.08(1 - \text{TBAREX}), 10^{-6}]$$

TBAREX = fraction of x-ray energy escaping a 10-km radius, obtained by calling Subroutine XTCOEF.

The fractions f_i in Eq. (26) are normalized by the expression

$$f_i' = \frac{f_i}{0.01 + \sum_{i=1}^5 f_i} \frac{\text{FRU} \times \text{EH}}{\text{EUX}}, \quad i = 1, 5.$$

One can verify that

$$\sum_{i=1}^5 f_i' + f_6'' = 1.$$

The Fortran variables for f_i' ($i = 1, 5$) and f_6'' are FR(I), $I = 1, 6$. FR(6) is not used in the HAG module.

5. X-RAY SOURCE CHARACTERISTICS AND ENERGY DEPOSITION

To facilitate development of the HAG module, we used the HARC Subroutine XTCOEF instead of the corresponding GET routines for the x-ray source and deposition characteristics. By improving the HARC procedure for x-ray energy deposition, we also eliminated use of the HARC Subroutine XDCOEF, used for x-ray energy deposition. Our calculation of the x-ray energy deposition is done in Subroutine PHEAT.

The HARC Subroutine XTCOEF(EM, TBARX) provides the effective energy transport coefficient for six spectral types, each characterized by the value of an index ($1 \leq \text{IDSX} \leq 6$). The argument EM (g/cm^2) is the intervening air mass and TBARX is the fraction of the energy reaching the depth EM. To prevent Subroutine XTCOEF from returning a physically impossible value in excess of 1.0 (due to using the same formula for extrapolation as interpolation), we revised the routine by using the formula

$$\text{TBARX} = 1 - \frac{\text{EM}}{10^{-7}} [1 - \text{COEF}(1, \text{IDSX})]$$

for values of EM less than 10^{-7} g/cm^2 , where $\text{COEF}(1, \text{IDSX})$ is the coefficient for the spectral index IDSX.

To deposit x-ray energy, we use the formula

$$\text{DAIXX}(\text{erg/g}) = \frac{\text{EX}}{4\pi} \frac{\text{TBXIN} - \text{TBXOUT}}{(\rho/3)(R_{\text{out}}^3 - R_{\text{in}}^3)},$$

where EX is the total x-ray energy, TBXIN and TBXOUT are obtained by calls to Subroutine XTCOEF(EMIN, TBXIN) and XTCOEF(EMOUT, TBXOUT), and the input arguments EMIN and EMOUT are given by

$$\text{EMIN}(\text{g/cm}^2) = \int_0^{R_{\text{in}}} \rho \, dR$$

$$\text{EMOUT}(\text{g/cm}^2) = \int_0^{R_{\text{out}}} \rho \, dR \, ,$$

with $\rho(\text{g/cm}^3)$ being the total mass density. R_{in} and R_{out} are the distances from the event point to the points of entry and exit of a cell, measured along the ray path from the event point through the cell center.

For permanent use one needs to replace the HARC Subroutine XTCOEF with the GET [Vol. 12] equivalent Subroutines WOXC(I) and WOXC(I, PMASS, FCONT) and Function EXPINTP(X1, Y1, X2, Y2, X). Our DRIVER should call WOXC(I) to read (a) the fractional x-ray energy in each of 18 energy groups (SPECX), and (b) the yield fraction in x rays (FEDX), and fill WOXC Common. One needs to change the current calls to Subroutine XTCOEF in Subroutines EUXFIT and PHEAT by calls to Subroutine WOXC, and take account of the fact that FCONT returned by Subroutine WOXC is the fraction of x-ray energy contained within PMASS (g/cm^2) rather than being the fraction transmitted beyond EM (g/cm^2) as in Subroutine XTCOEF. One also needs to get the total energy WB (MT) into DEVICE Common, as well as convert from MT to ergs.

6. DEPOSITION OF DEBRIS PARTICLES

6.1 INTRODUCTION

Before we proceed with the detailed physical and geometric considerations necessary for deposition, we will outline the overall procedure. The total weapon kinetic yield is divided into loss-cone, ion-leak, CHEX, UV, and thermal energies. Each of these energy components, except the last, is deposited separately in the HAG. First, the loss-cone particles are deposited in a field-aligned tube centered about the burst-point field line. Next, the ion-leak particles are also deposited within a field-aligned tube but of size different from the loss-cone tube. Then we deposit the CHEX particles as neutral particles without any consideration of subsequent ionization and magnetic field focusing. Deposition of UV energy is discussed in Section 9.

Changes of chemical species produced in each cell by the sum of the heavy-particle energy depositions modify the species composition that would normally be seen by the UV photon flux. Although the final species complement may differ in a heavily-dosed cell if the UV were deposited first, the differences are not expected to be large. In lightly-dosed cells, the order of irradiation is probably of minor consequence. At any rate, we found it convenient to deposit the heavy-particle energy first in our implementation.

6.2 HEAVY-PARTICLE ENERGY LOSS

According to heavy-particle stopping theory [LS-63], the differential energy loss rate of a particle traversing matter is

$$\frac{dE}{dx} = - n S(E) \quad (\text{eV/cm}) \quad (27)$$

where E is the particle energy, x the distance, and n the number density of target atoms. The stopping cross-section $S(E)$ has an elastic contribution α and an inelastic portion $\beta\sqrt{E}$; viz,

$$S(E) = \alpha + \beta\sqrt{E} \quad (\text{eV cm}^2) \quad . \quad (28)$$

Values for oxygen and aluminum atoms slowing down in nitrogen are found by direct substitution into Eqs. (2.5) and (2.7') in LS-63. If the particle energy E is measured in eV, the values of α and β are, for oxygen,

$$\alpha_{\text{O}} = 2.98 \times 10^{-14} \quad [\text{eV cm}^2 (\text{target atom})^{-1}]$$

$$\beta_{\text{O}} = 1.13 \times 10^{-16} \quad [\text{eV}^{\frac{1}{2}} \text{ cm}^2 (\text{target atom})^{-1}]$$

and, for aluminum,

$$\alpha_{\text{Al}} = 5.47 \times 10^{-14} \quad [\text{eV cm}^2 (\text{target atom})^{-1}]$$

$$\beta_{\text{Al}} = 1.52 \times 10^{-16} \quad [\text{eV}^{\frac{1}{2}} \text{ cm}^2 (\text{target atom})^{-1}] \quad .$$

Note that the value of α_{O} is much larger than that propagated into the work of HM-72b from Appendix 4A of HL-71.

In Eq. (27) it is often convenient to introduce the areal mass density (g/cm^2)

$$d\xi = mn \, dx \quad (29)$$

traversed by a particle in lieu of the rectilinear distance; i. e.,

$$m \frac{dE}{d\xi} = - S(E) \quad . \quad (30)$$

Here, m is the mass of a target atom. From Eq. (30) we can compute by straightforward integration the areal mass density required to slow a particle from energy E_1 to E_2 ,

$$\xi(E_1 \rightarrow E_2) = -m \int_{E_1}^{E_2} \frac{dE}{S(E)} \quad (31a)$$

After inserting Eq. (28) in Eq. (31a) and integrating, we obtain the result

$$\xi(E_1 \rightarrow E_2) = \frac{2m\alpha}{\beta^2} \left\{ \frac{\beta}{\alpha} \left(\sqrt{E_1} - \sqrt{E_2} \right) - \ln \frac{1 + \frac{\beta}{\alpha} \sqrt{E_1}}{1 + \frac{\beta}{\alpha} \sqrt{E_2}} \right\} \quad (31b)$$

which is required for the calculation of energy deposition in a cell.

In our application of Eq. (31b) we will normally know ξ along the particle path in a cell and the cell-entrance energy E_1 of the particle; we will then calculate the particle cell-exit energy E_2 by use of the Function Routine FZET which, given the range, iteratively solves for the energy in the range-energy equation. The difference $E_1 - E_2$ is then the total energy deposited by the particle in the cell, of which a fraction f_α is due to elastic collisions and a fraction f_β is due to inelastic collisions, where

$$f_\alpha = \delta E_\alpha / (E_1 - E_2) \quad (32a)$$

$$\delta E_\alpha = \alpha \xi(E_1 \rightarrow E_2) / m \quad (32b)$$

$$f_\beta = 1 - f_\alpha \quad (32c)$$

If the error in using the first-order Taylor expansion of Eq. (29) is less than the corresponding tolerance accepted in using the Function Routine FZET, as is the case if the traversed areal density is very small, we compute the cell-exit energy by using the (second-order) Taylor expansion of Eq. (30).

6.3 ENERGY DEPOSITION OVER A DISTRIBUTION FUNCTION

Although Eq. (28) gives the stopping cross-section for a mono-energetic particle of energy E , the particle emissions span a distribution of energies. The sum of the elastic (ϵ_e) and inelastic (ϵ_i) energy contributions per target atom (eV atom^{-1}) is

$$\epsilon_t = \frac{1}{A} \int_0^\infty dE (\alpha + \beta \sqrt{E}) \left(- \frac{dN}{dE_o} \frac{dE_o}{dE} \right)_{E_o = E_\xi + E} \quad (33a)$$

$$= \epsilon_e + \epsilon_i \quad (33b)$$

with A the cross-sectional area of the particle beam at the deposition location, E_o the particle energy at the source prior to penetration of any matter, E the particle energy at the deposition location after traversal of $\xi (\text{g/cm}^2)$ of material, and E_ξ the energy lost by the particle to reach the deposition location. The energy transformation function is just

$$\frac{dE_o}{dE} = \frac{S(E_o)}{S(E)} \quad (34)$$

and the number-vs-energy distribution is related to the integral number spectrum by

$$N(>E) = - \int_E^\infty dE_o \frac{dN}{dE_o} \quad (35)$$

6.4 PRACTICAL IMPLEMENTATION

In the practical situation where deposition must be done in hundreds of cells, it is desirable to have analytical expressions for the two integrals in Eq. (33a). Number-distribution functions for the particle sources outlined in Section 3.3 do not lead to expressions analytically integrable.

To circumvent this difficulty we have represented each continuous energy distribution by a number-vs-energy histogram of equal energy intervals. Each bar of the histogram represents a fixed number of particles at a single energy midway between the edge values. Each monoenergetic beam is then deposited as a separate source. An attractive feature of this approach is its adaptability to any distribution that may arise in the future.

6.4.1 Histogram Representation

If the number-vs-energy distribution of the source function is represented by p monoenergetic beams,

$$\frac{dN}{dE} = \sum_{k=1}^p N_k \delta(E - E_k) , \quad (36)$$

then the elastic and inelastic energies (eV atom^{-1}) deposited at a depth $\xi (\text{g/cm}^2)$ from the source location are, from Eq. (33b),

$$\epsilon_e = \frac{\alpha}{A} \int_0^\infty dE \sum_{k=1}^p N_k \delta(E - \overline{E_k - E_\xi}) \quad (37a)$$

$$= \frac{\alpha}{A} \sum_{k=1}^p N_k ; \quad E_k \geq E_\xi \quad (37b)$$

and

$$\epsilon_i = \frac{\beta}{A} \int_0^\infty dE \sqrt{E} \sum_{k=1}^p N_k \delta(E - \overline{E_k - E_\xi}) \quad (38a)$$

$$= \frac{\beta}{A} \sum_{k=1}^p N_k \sqrt{E_k - E_\xi} ; \quad E_k \geq E_\xi . \quad (38b)$$

The number of particles at energy E_k for each particle source function is found from

$$N_k = \frac{1}{p} \frac{W}{E_k} \quad (39)$$

where W assumes, in turn, each of the values (expressed in eV) of W_{lcd} , W_{ild} , and W_{chex} . Beam energies E_k are determined from the $p+1$ histogram-bar edges by

$$E_k = \frac{1}{2} (E_i + E_{i+1}) ; \quad \begin{cases} i = 1, \dots, p \\ k = i \end{cases} \quad (40)$$

6.4.2 Loss-Cone Histogram

Histogram-bar energy edges for the downward-going loss-cone yield is found by equating the right-hand side of Eq. (19b) to the fraction of the energy below E_{i+1} . Explicitly we have

$$\frac{E_{i+1}^{5/2} - E_{\min}^{5/2}}{E_{\max}^{5/2} - E_{\min}^{5/2}} = \frac{i}{p} ; \quad i = 1, \dots, p \quad (41)$$

or

$$E_{i+1} = \left[E_{\min}^{5/2} + \frac{i}{p} (E_{\max}^{5/2} - E_{\min}^{5/2}) \right]^{2/5} ; \quad i = 1, \dots, p \quad (42)$$

with

$$E_1 = E_{\min} , \quad E_{p+1} = E_{\max} .$$

6.4.3 Ion-Leak Histogram

For the ion-leak source we use Eq. (22) to find the energy edges,

$$\frac{E_{i+1}^{\frac{1}{2}} - E_{\min}^{\frac{1}{2}}}{E_{\max}^{\frac{1}{2}} - E_{\min}^{\frac{1}{2}}} = \frac{i}{p} ; \quad i = 1, \dots, p \quad (43)$$

or

$$E_i = \left[E_{\min}^{\frac{1}{2}} + \frac{i}{p} \left(E_{\max}^{\frac{1}{2}} - E_{\min}^{\frac{1}{2}} \right) \right]^2 ; \quad i = 1, \dots, p \quad (44)$$

with

$$E_1 = E_{\min} , \quad E_{p+1} = E_{\max} .$$

6.4.4 CHEX Histogram

In a similar manner we use Eq. (25a) to find the energy histogram-bar edges for the CHEX-particle source:

$$\frac{e^{-aE_{\min}} - e^{-aE_{i+1}}}{e^{-aE_{\min}} - e^{-aE_{\max}}} = \frac{i}{p} ; \quad i = 1, \dots, p \quad (45)$$

or

$$E_{i+1} = -\frac{1}{a} \ln \left[e^{-aE_{\min}} - \frac{i}{p} \left(e^{-aE_{\min}} - e^{-aE_{\max}} \right) \right] ; \quad i = 1, \dots, p \quad (46)$$

with

$$E_1 = E_{\min} , \quad E_{p+1} = E_{\max} .$$

6.5 PARTICLE SPATIAL DISTRIBUTIONS

In addition to an energy distribution, each of the three heavy-particle sources has its own spatial distribution. Since we did not have time to introduce the re-direction effects of the geomagnetic field in the

deposition of CHEX particles, we assumed the particles to be emitted with spherical symmetry. However, the loss-cone and ion-leak particles are guided by the geomagnetic field in the deposition processes within tubes about the burst-point field line. In this section we discuss the deposition and the particle spatial distribution within these tubes; we ignore spiralling effects.

Before presenting the formulas, we describe the overall procedure. The differential form for the radial distribution of the downward-moving loss-cone and ion-leak energies has been specified at 100-km altitude by Crevier and Kilb [Vol. 10]. We consider the corresponding integral distribution function and form q concentric rings in the tangent plane so that each ring contains $1/q$ of the total energy for either the loss-cone or ion-leak particles. We compute the location (geographic colatitude and east longitude) of the center of the distribution function, i. e., the origin of the tangent-plane coordinate system at 100-km altitude, by tracing the event-point field line. The source points (in the vicinity of the event point) corresponding to representative points in the concentric rings are determined by tracing the field lines passing through the representative points to their intersections with the equipotential surface through the event point.

6.5.1 Representation of the Spatial Distribution at 100-km Altitude

The spatial distribution suggested by Vol. 10 for the downward-going particle-energy in the loss-cone and ion-leak tubes is of the form

$$dW_d = \frac{W_d}{\pi R_o^2} \frac{r}{[1 + (r/R_o)^2]^2} dr d\varphi, \quad (47)$$

such that the integration over the cross-sectional area of the tube,

$$\frac{W_d}{\pi R_o^2} \int_0^{2\pi} d\varphi \int_0^\infty dr \frac{r}{[1 + (r/R_o)^2]^2} = W_d , \quad (48)$$

is just the downward-going energy. In these expressions r and φ are the coordinates in the tube's cross-sectional area, W_d acquires the value W_{lcd} or W_{ild} , and R_o acquires the characteristic tube radius R_{lc} or R_{il} for the loss-cone and ion-leak particles, respectively. The variable r is ultimately defined in Vol. 10 as the horizontal distance, at 100-km altitude, from the burst-point field line to the field line through a representative point.

The integral distribution function for the particle energy passing within a distance r of the event-point field line is found from Eq. (48) by integrating from 0 to radius r , i. e. ,

$$\frac{W_d(0, r)}{W_d} = 1 - \frac{1}{1 + r^2/R_o^2} . \quad (49)$$

To avoid the concept of a tube with infinite radius, we limit the radius of the tube to $3R_o$. According to Eq. (49), $W_d(0, 3R_o)/W_d = 0.90$, i. e. , 0.90 of the energy lies within the radius $3R_o$. However, we will re-normalize the distribution function so that the entire energy W_d is within the radius $3R_o$. Our new integral distribution function for the radial distribution of the particle energy is

$$f = \frac{1}{0.9} \frac{\rho^2}{1 + \rho^2} \quad (50a)$$

where

$$\rho \equiv r/R_o . \quad (50b)$$

If we solve Eq. (50a) for ρ ,

$$\rho = \left[\frac{0.9f}{1 - 0.9f} \right]^{\frac{1}{2}} \quad (51a)$$

or

$$r = R_o \left[\frac{0.9f}{1 - 0.9f} \right]^{\frac{1}{2}}, \quad (51b)$$

we then can compute the radius for a given value of f . For the present we are using four annular rings, with outer radii corresponding to values of f equal to $1/4$, $1/2$, $3/4$, and 1 , and characteristic circles within these annular rings with radii corresponding to values of f equal to $1/8$, $3/8$, $5/8$, and $7/8$. These radii are tabulated in Table 1. On each characteristic circle we place four representative points at 90-deg intervals except that we also place a representative point at the center and on the fourth characteristic circle we double the number of points. To the set of s equally-spaced representative points on alternate characteristic circles, we apply a rotation about the event-point field line equal to π/s . The weight assigned to each of the s representative points within one of the q annular rings is $1/(qs)$. The annular rings, characteristic circles, and representative points currently used are shown in Fig. 8.

6.5.2 Particle Allocations

The spatial allocation of the source particles N_k (cf. Eq. (39)) at energy E_k is simply $N_k/(qs)$ for every field line traced.

Table 1. Radii of Annular Rings and Characteristic Circles Used to Approximate the Radial Distribution Function of Downward-Moving Loss-Cone and Ion-Leak Energies.

Integral Fraction of Energy, f	Outer Radius of Annular Ring ^a	Radius of Characteristic Circle ^a
0	0	
0.125		0.356
0.250	0.539	
0.375		0.713
0.500	0.904	
0.625		1.134
0.750	1.441	
0.875		1.925
1.000	3.000	

^aIn units of the characteristic tube radius R_0 .

6.6 STARTING COORDINATES OF THE FIELD LINES

It remains to establish the geocentric coordinates (longitude, colatitude, and geocentric-radius) of each of the particle source points in the vicinity of the event point. As mentioned above, these source points, corresponding to the representative points in the tangent plane at 100-km altitude, are determined by tracing the field lines passing through the representative points to their intersection with the equipotential surface through the event point. We now derive the equations to determine these intersections.

The equation for a dipole field line is

$$r = r_0 \sin^2 \chi \quad (52)$$

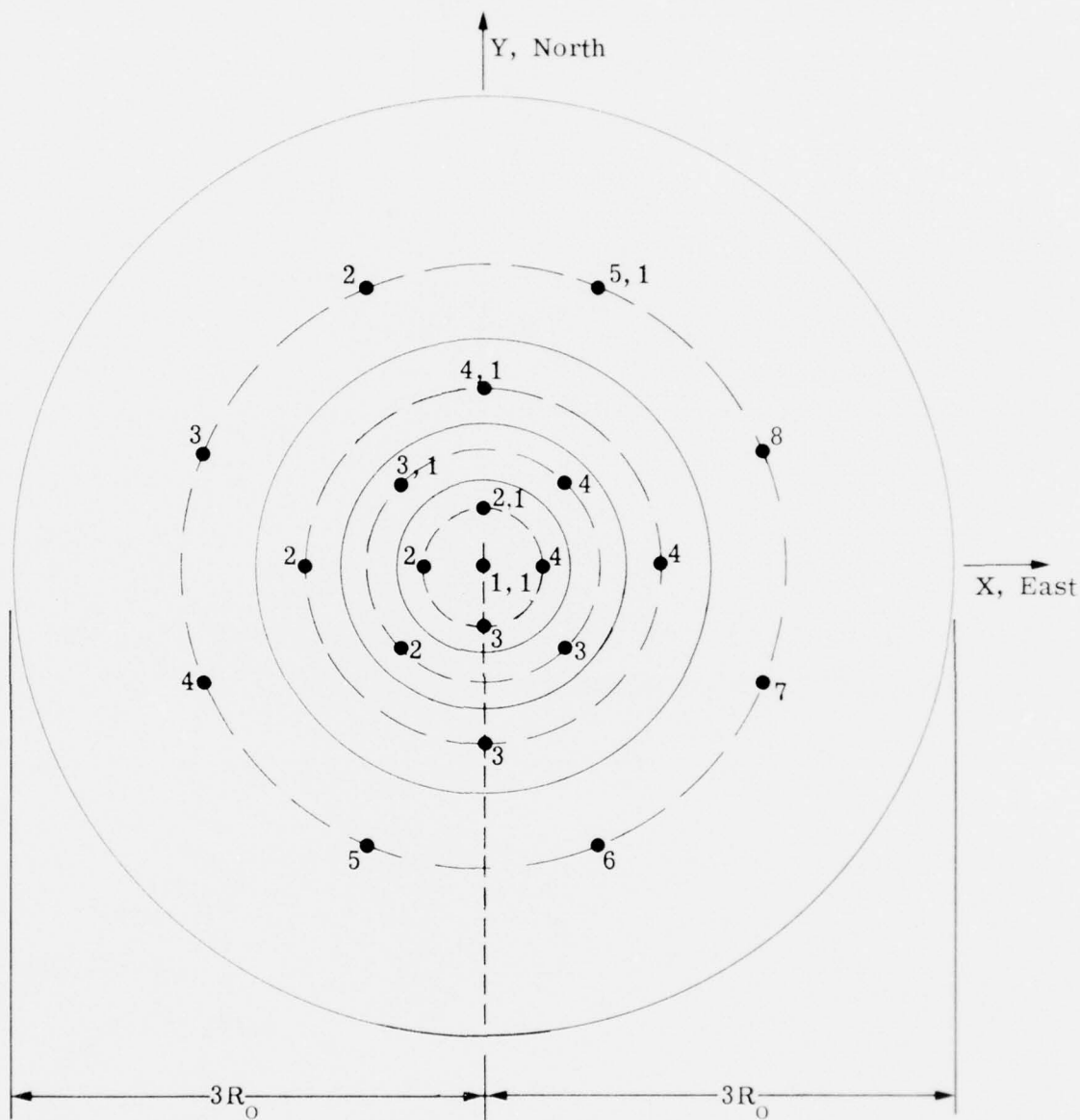


Fig. 8. Four Annular Rings, Four Characteristic Circles, and 21 Representative Points Used to Approximate the Radial Distribution of Downward-Moving Loss-Cone and Ion-Leak Energies. The plane of the paper represents a tangent plane at 100-km altitude with origin at the event-point field line. East on the diagram corresponds to the tangent-plane X axis.

where r_0 is the equatorial radius and χ is the dipole colatitude. (The r in Eq. (52) should not be confused with the r in Section 6.5.1.) The potential function for a magnetic dipole is

$$V = |M| r^{-2} \cos \chi \quad (53)$$

where $|M|$ is the magnitude of the magnetic dipole moment. For a constant value of V ,

$$|M| r^{-2} \cos \chi = |M| r_1^{-2} \cos \chi_1, \quad (54)$$

where the subscript 1 denotes the event point, so that the equation for the equipotential curve is

$$r = r_1 \left[\frac{\cos \chi}{\cos \chi_1} \right]^{\frac{1}{2}}. \quad (55)$$

The equation for the field line through a source point is given by Eq. (52) which we rewrite as

$$\cos^2 \chi = 1 - r/r_0. \quad (56)$$

By eliminating $\cos^2 \chi$ between Eqs. (55) and (56), we get

$$r_s^4 = \frac{r_1^4}{\cos^2 \chi_1} \left[1 - \frac{r_s}{r_0} \right] \quad (57)$$

or

$$x^4 + AB^{-1}x - A = 0 \quad (58)$$

where

$$x = 1 + h_s/R_e \quad (59a)$$

$$A = \frac{(1 + h_1/R_e)^4}{\cos^2 \chi_1} \quad (59b)$$

$$B = 1 + h_o/R_e . \quad (59c)$$

We use Newton's method of iteration to solve the quartic, Eq. (58), for the (reduced) geocentric radius at which the source-point field line intersects the event-point equipotential surface. Given the geographic coordinates of a representative point in the tangent plane at 100-km altitude, Subroutine CONJUG will trace the field line through the point to an altitude h_s and return the desired geocentric coordinates (latitude and longitude) of the intersection of the source-point field line and the event-point equipotential surface.

6.7 FIELD-LINE TRACING

We need to know the heavy-particle energy deposited in each cell, which can be found if we know the areal mass density along the path within a cell (the product of the field-line path length within the cell and the mass density in the cell). Thus, we must trace a field line from the source point through each cell until the boundary of the HAG is reached.

To trace the field lines we start at a given source point at altitude h_s . Given the geographic coordinates of the source point and a new altitude h_v and altitude step Δh , where

$$h_v = h_s - \Delta h , \quad (60)$$

$$\Delta h = \Delta \ell \sin I , \quad (61)$$

and I is the local dip angle, Subroutine CONJUG will return the geographic coordinates of the new altitude point and Subroutine INDEX will

return the indices of the cell containing the new point. If the new point is in the same cell as the source point, a second new altitude point, lower by an amount Δh , is selected. Again, Subroutine CONJUG, given the geographic coordinates of the source point and the altitude ($h_s - 2\Delta h$) of the second point, will return the geographic coordinates of the second point on the field line and Subroutine INDEX returns the indices of the cell containing the second point. This procedure is continued until the cell indices indicate the field line has exited from the cell. An iterative backup-and-boundary-crossing procedure is then followed in which Δl , initially set to 8 km, is repeatedly halved and the boundary crossing is finally accepted when $\Delta l = 1$ km. The field-line path length from the starting point to the (approximate) exit point is also returned by Subroutine CONJUG. This exit point is then used as a new starting point with $\Delta l = 8$ km and the field line is further traced until it exits the cell from which it last started. This procedure is continued until the field line leaves the HAG or until the most energetic particle being followed has stopped. This procedure is then repeated for every source point corresponding to the set of representative points in the tangent plane at 100-km altitude.

6.8 LOSS-CONE AND ION-LEAK PARTICLE DEPOSITION

Energy deposition for loss-cone and ion-leak particles, while based on Eqs. (37b) and (38b), must be done differently to conserve energy explicitly. In particular, the specific energies (erg/g) deposited in a cell by loss-cone and ion-leak heavy-particle elastic collisions and inelastic collisions, are, respectively,

$$\epsilon'_e = \frac{\epsilon_o}{M} \sum_{k=1}^p N_k (E_{in} - E_{out})_k f_{\alpha k} \quad (62)$$

and

$$\epsilon'_i = \frac{\epsilon_o}{M} \sum_{k=1}^p N_k (E_{in} - E_{out})_k (1 - f_{\alpha k}) \quad (63)$$

where E_{in} and E_{out} are the entrance and exit energies (eV) of the particle in the k th energy group, M is the cell mass in grams, $\epsilon_o = 1.6 \times 10^{-12}$ erg/eV, and $f_{\alpha k}$ is given by Eq. (32a) with an additional subscript k .

6.9 CHEX-PARTICLE DEPOSITION

As mentioned in Section 6.5, the CHEX-particles are considered emitted with spherical symmetry, or the energy emitted per steradian is given by $W_{chex}/4\pi$. Particle paths through each cell are straight and have a direction determined by the line that connects the event point and the center of the cell. Path lengths within each cell, from entrance to exit, are found by the Subroutine PLINE and the intercepted steradian mass is given by

$$M_{\Omega} = \frac{1}{3} \rho (R_{out}^3 - R_{in}^3) \quad (64)$$

Here, ρ is the cell mass density; R_{in} and R_{out} are slant distances from the event point to the cell entrance and exit, respectively.

The specific energies deposited in a cell by CHEX heavy-particle elastic and inelastic collisions, are, respectively,

$$\epsilon'_e = \frac{\epsilon_o}{M_{\Omega}} \sum_{k=1}^p \frac{N_k}{4\pi} (E_{in} - E_{out})_k f_{\alpha k} \quad (65)$$

and

$$\epsilon'_i = \frac{\epsilon_o}{M_{\Omega}} \sum_{k=1}^p \frac{N_k}{4\pi} (E_{in} - E_{out})_k (1 - f_{\alpha k}) \quad (66)$$

where, again, E_{in} and E_{out} are the entrance and exit energies (eV) of the particle in the k th energy group.

7. PARTITIONING OF THE DEPOSITED DEBRIS ENERGY AND CONSEQUENT SPECIES (SUBROUTINE HPCHEM)

Subroutine HPCHEM partitions the total energy lost in each cell by loss-cone, ion-leak, and CHEX particles undergoing inelastic and elastic collisions. The energy is partitioned into heavy-particle thermal, electron thermal, dissociation, ionization, excitation, and radiation. A model of heavy-particle prompt chemistry is also used to compute the changes in number densities of N_2 , O_2 , $N(4S)$, $N(2D)$, O , N_2^+ , O_2^+ , N^+ , O^+ , and electrons.

One of the simplifications made in depositing the heavy-particle energies is that the range-energy relation used in Subroutines DEPO and CHXDEP is based on the total mass density of a cell whereas in Subroutine HPCHEM only the species N_2 , O_2 , and O are considered as targets. The modeling of the associated heavy-particle prompt chemistry is based on a speculative treatment [HM-72b, Section 6; HL-73b, Section 5], modified by the need to interface with the late-time grid chemistry. (The rationale for the heavy-particle prompt-chemistry modeling, to the extent it exists, will not be repeated here.) In this late-time chemistry, for atomic nitrogen only $N(^2D)$ is carried as an excited term and for atomic oxygen only $O(^1D)$ is accounted for (implicitly) as an excited term. Thus, $N(^2P)$ and $O(^1S)$ are purposely excluded as possible reaction products of the heavy-particle prompt chemistry. Conversion of N_2^+ and O_2^+ into NO^+ (the only molecular ion in the grid chemistry) is performed at the beginning of Subroutine PCHEM.

In Table 2 we summarize the reactions from inelastic and elastic collisions that are modeled in the prompt chemistry from heavy-particle energy deposition.

Table 2. Heavy-Particle Prompt-Chemistry Reactions
from Inelastic and Elastic Collisions.

	Reaction	Branching Ratio	Number of Reactions, ^a cm ⁻³
INELASTIC	$N_2 \rightarrow \begin{cases} N_2^+ + e \\ N(^4S) + N^+ + e \end{cases}$	$\begin{matrix} 1/1.35 \\ 0.35/1.35 \end{matrix}$	$\frac{2[N_2]}{n} [e]$
	$O_2 \rightarrow \begin{cases} O_2^+ + e \\ O(^3P) + O^+ + e \end{cases}$	$\begin{matrix} 1/1.35 \\ 0.35/1.35 \end{matrix}$	$\frac{2[O_2]}{n} [e]$
	$O \rightarrow O^+ + e$		$\frac{[O]}{n} [e]$
ELASTIC	$N_2 \rightarrow N(^4S) + \begin{cases} N(^4S) \\ N(^2D) \end{cases}$	$\begin{matrix} 4/14 \\ 10/14 \end{matrix}$	$\frac{2[N_2]}{n} n_c$
	$O_2 \rightarrow O(^3P) + \begin{cases} O(^3P) \\ O(^1D) \end{cases}$	$\begin{matrix} 9/14 \\ 5/14 \end{matrix}$	$\frac{2[O_2]}{n} n_c$
	$O \rightarrow \begin{cases} O(^3P) \\ O(^1D) \end{cases}$	$\begin{matrix} 9/14 \\ 5/14 \end{matrix}$	$\frac{[O]}{n} n_c$

^a $n = 2\{[N_2] + [O_2]\} + [O]$ = number density of nuclei.
 n_c = number density of particles in cascade of elastic-collision energy.

In Subroutine HPCHEM, before dealing explicitly with the partitioning of the species and energies from the inelastic and elastic collisions, we must make a number of preliminary steps and establish several parameters used in the modeling.

1. From the extended core storage for the cell of interest, obtain the total mass density $\rho(\text{g/cm}^3)$ and the number densities (cm^{-3}) of N_2 , O_2 , and O .

2. For both the inelastic and elastic-collision contributions, sum the specific energies deposited by the loss-cone (PEI and PEE), ion-leak (QEI and QEE), and CHEX (CEI and CEE) particles.

$$\epsilon_i(\text{erg/g}) = \text{PEI} + \text{QEI} + \text{CEI}$$

$$\epsilon_e(\text{erg/g}) = \text{PEE} + \text{QEE} + \text{CEE} .$$

3. Compute the number density of nuclei in N_2 , O_2 , and O .

$$n(\text{nuclei/cm}^3) = 2 \{ [\text{N}_2] + [\text{O}_2] \} + [\text{O}] .$$

4. Compute the threshold-energy parameter used in modeling the cascade of elastic energy.

$$E_t = \{ 39.04[\text{N}_2] + 20.48[\text{O}_2] + 25.40[\text{O}] \} / n .$$

In this equation the coefficient of $[\text{O}]$ includes the replacement of $\epsilon_m(\text{O})$ by $\epsilon_m(\text{O}) + \epsilon_r(\text{O})$ in Eq. (68) of HM-72b (or Eq. (40) of HL-73b).

5. Compute the weighted value of the energy removed per collision in the cascade of elastic energy.

$$\epsilon(\text{eV}) = \{ C_1[\text{N}_2] + C_2[\text{O}_2] + C_3[\text{O}] \} / n$$

where

$$C_1 = 2[9.76 + 2.37(1 - F_9) + 12.0]$$

$$C_2 = 2[5.12 + 1.96 F_{10} + 12.0]$$

$$C_3 = 1.96 F_{10} + 12.0$$

$$F_9 = 4/14$$

$$F_{10} = 5/14 .$$

6. Limit the specific energies to values less than those required, according to the model, for complete ionization and (effective) dissociation of the N_2 , O_2 , and O densities in excess of 1.0. Define

$$N_{HP}(\text{cm}^{-3}) = [N_2] + [O_2] + [O] - 3.0$$

$$\epsilon_{imax} = 28.5 \epsilon_1 N_{HP}$$

$$\epsilon_{emax} = \epsilon \epsilon_1 N_{HP}$$

where the conversion factor ϵ_1 is

$$\epsilon_1(\text{erg eV}^{-1} \text{ cm}^3 \text{ g}^{-1}) = \epsilon_o/\rho$$

$$\epsilon_o = 1.60 \times 10^{-12} \text{ erg/eV} .$$

The fractions of N_{HP} destroyed by inelastic and by elastic processes are, respectively,

$$g_i = \epsilon_i/\epsilon_{imax}$$

and

$$g_e = \epsilon_e/\epsilon_{emax} .$$

If $g_i + g_e > 1.0$, one must reduce ϵ_i and ϵ_e by the ratio $1/(g_i + g_e)$.

We are now ready to deal explicitly with the inelastic collisions.

1. Compute the electron density:

$$[e] = \epsilon_i / (28.5 \epsilon_1) .$$

2. Partition the charged species from inelastic collisions.

$$[N_2^+] = \frac{1}{1.35} \frac{2[N_2]}{n} [e]$$

$$[O_2^+] = \frac{1}{1.35} \frac{2[O_2]}{n} [e]$$

$$[N^+] = \frac{0.35}{1.35} \frac{2[N_2]}{n} [e]$$

$$[O^+]_2 = \frac{0.35}{1.35} \frac{2[O_2]}{n} [e]$$

$$[O^+]_1 = \frac{[O]}{n} [e]$$

$$[O^+] = [O^+]_2 + [O^+]_1 .$$

3. Record the corresponding neutral-atom densities produced in dissociative ionization in inelastic collisions:

$$[N(^4S)] = [N^+]$$

$$[O(^3P)] = [O^+]_2 .$$

4. Partition the energy from inelastic collisions into four modes and the fraction of energy in each mode.

Electron Thermal Energy:

$$E(\text{eV}/\text{cm}^3) = 1.5 [e]$$

$$f'_{\text{KE}} = \epsilon_1 E / \epsilon_i$$

Dissociation Energy:

$$D_i(\text{eV}/\text{cm}^3) = 9.76 [\text{N}^+] + 5.12 [\text{O}^+]_2$$

$$f'_D = \epsilon_1 D_i / \epsilon_i$$

Ionization Energy:

$$I(\text{eV}/\text{cm}^3) = 15.58 [\text{N}_2^+] + 12.06 [\text{O}_2^+] + 14.53 [\text{N}^+] + 13.62 [\text{O}^+]$$

$$f_I = \epsilon_1 I / \epsilon_i$$

$$I_1(\text{erg/g}) = \epsilon_1 I$$

Radiation Energy:

$$f'_R = 1 - (f'_{\text{KE}} + f'_D + f_I)$$

$$R_i(\text{eV}/\text{cm}^3) = f'_R \epsilon_i / \epsilon_1$$

We now deal explicitly with the elastic collisions:

1. Compute the total number density of particles from the cascade of elastic energy:

$$n_c(\text{cm}^{-3}) = \frac{4 f_{\text{KE}} \epsilon_e}{\epsilon_1 (3E_t - \epsilon)}$$

where

$$f_{KE} = \frac{E_t - \epsilon/3}{E_t + \epsilon} \cdot$$

2. Partition the neutral species from elastic collisions. The (fast) particle densities from the elastic-energy cascade are

$$[N]_c = \frac{2[N_2]}{n} n_c$$

$$[O]_{c2} = \frac{2[O_2]}{n} n_c$$

$$[O]_{c1} = \frac{[O]}{n} n_c$$

$$[O]_c = [O]_{c2} + [O]_{c1} \cdot$$

The (slow) particle densities from the elastic-energy cascade are

$$[N]_{cs} = [N]_c$$

$$[O]_{c2s} = [O]_{c2} \cdot$$

3. Partition among excited states the (total) particle densities from the elastic-energy cascade.

$$[N(^4S)] = F_9[N]_c + [N]_{cs}$$

$$[N(^2D)] = (1 - F_9) [N]_c$$

$$[O(^3P)] = (1 - F_{10}) [O]_c + [O]_{c2s}$$

$$[O(^1D)] = F_{10}[O]_c \cdot$$

4. Partition the energy from elastic collisions into four modes.

Heavy-particle thermal energy:

$$K(\text{eV}/\text{cm}^3) = f_{\text{KE}} \epsilon_e / \epsilon_1$$

$$K_1(\text{erg/g}) = \epsilon_1 K$$

Dissociation energy:

$$D_e(\text{eV}/\text{cm}^3) = 9.76[\text{N}]_c + 5.12[\text{O}]_{c2}$$

Excitation energy:

$$X_e(\text{eV}/\text{cm}^3) = 2.37 (1 - F_9)[\text{N}]_c + 1.96 F_{10} [\text{O}]_c$$

$$X_{e1}(\text{erg/g}) = \epsilon_1 X_e$$

Radiation energy:

$$R(\text{eV}/\text{cm}^3) = 12 \{ [\text{N}]_c + [\text{O}]_c \} .$$

We can now combine the results from inelastic and elastic collisions.

1. Add the contributions from the inelastic and elastic collisions to obtain the total values of dissociation and radiation energies.

$$D(\text{eV}/\text{cm}^3) = D_i + D_e$$

$$D_1(\text{erg/g}) = \epsilon_1 D$$

$$R(\text{eV}/\text{cm}^3) = R_i + R_e$$

$$R_1(\text{erg/g}) = \epsilon_1 R \quad .$$

2. Compute the total fractional partitions of energy for the six modes.

$$f_K = \epsilon_1 K / (\epsilon_i + \epsilon_e)$$

$$f_E = \epsilon_1 E / (\epsilon_i + \epsilon_e) \quad .$$

$$f_D = \epsilon_1 D / (\epsilon_i + \epsilon_e)$$

$$f_{X_e} = \epsilon_1 X_e / (\epsilon_i + \epsilon_e)$$

$$f_I = \epsilon_1 I / (\epsilon_i + \epsilon_e)$$

$$f_R = \epsilon_1 R / (\epsilon_i + \epsilon_e) \quad .$$

The fractional error in energy conservation is

$$F = f_K + f_E + f_D + f_{X_e} + f_I + f_R - 1 \quad .$$

3. Compute (and collate) the changes in species densities.

$$\delta[N_2] = - \frac{2[N_2]}{n} \{[e] + n_c\}$$

$$\delta[O_2] = - \frac{2[O_2]}{n} \{[e] + n_c\}$$

$$\delta[N(^4S)] = [N^+] + (1 + F_9) \frac{2[N_2]}{n} n_c$$

$$\delta[N(^2D)] = (1 - F_9) \frac{2[N_2]}{n} n_c$$

$$\delta[O] = -\frac{[O]}{n} [e] + [O^+]_2 + 2 \frac{2[O_2]}{n} n_c$$

$$\delta[e] = [e]$$

$$\delta[N_2^+] = \frac{1}{1.35} \frac{2[N_2]}{n} [e]$$

$$\delta[O_2^+] = \frac{1}{1.35} \frac{2[O_2]}{n} [e]$$

$$\delta[N^+] = 0.35 \delta[N_2^+]$$

$$\delta[O^+] = 0.35 \delta[O_2^+] + \frac{[O]}{n} [e]$$

4. Compute the sums of changes in densities of nitrogen nuclei, oxygen nuclei, and charged species as measures of conservation errors.

$$\sum \delta N = 2 \{ \delta[N_2] + \delta[N_2^+] \} + \delta[N(^4S)] + \delta[N(^2D)] + \delta[N^+]$$

$$\sum \delta O = 2 \{ \delta[O_2] + \delta[O_2^+] \} + \delta[O] + \delta[O^+]$$

$$\sum \delta C = \delta[N_2^+] + \delta[O_2^+] + \delta[N^+] + \delta[O^+] - \delta[e] .$$

5. Compute the sum of electron thermal and $O(^1D)$ excitation energies per newly-formed electron.

$$E_{pe}(\text{eV/electron}) = \left(E + 1.96 F_{10} \{ [O_2] + 0.5[O] \} \frac{2n_c}{n} \right) / [e] .$$

6. Store changes in cell quantities in temporary scratch area (BUF2).

$\text{BUF2}(1) = \delta[e]$	$\text{BUF2}(7) = \delta[\text{N}^+]$
$\text{BUF2}(2) = \delta[\text{N}(^4\text{S})]$	$\text{BUF2}(8) = \delta[\text{O}^+]$
$\text{BUF2}(3) = \delta[\text{N}(^2\text{D})]$	$\text{BUF2}(9) = E_{\text{pe}}$
$\text{BUF2}(4) = \delta[\text{O}]$	$\text{BUF2}(10) = K_1$
$\text{BUF2}(5) = \delta[\text{N}_2]$	$\text{BUF2}(11) = \delta[\text{N}_2^+]$
$\text{BUF2}(6) = \delta[\text{O}_2]$	$\text{BUF2}(12) = \delta[\text{O}_2^+]$

8. ORGANIZATION OF THE HEAVY-PARTICLE RELATED ROUTINES

An outline of the portion of the HAG module for kinetic-yield partitioning, heavy-particle energy deposition, and generation of consequent chemical species is shown in Fig. 9. The interface with the rest of the HAG module is through three calls by Subroutine PROMPG.

The first call (for debris) from Subroutine PROMPG is to Subroutine DEBRIS which serves as a control routine for seven subsequent steps. Subroutine HDPART is called in Step 1 for the partitioning of the kinetic yield, given the kinetic yield, event-point magnetic field, and event-point mass density. Step 1 is accomplished with the aid of Subroutines LOSCON, IONLEK, and CHXLOS. A return to Subroutine DEBRIS occurs with values for the downward-moving *loss-cone* energy (WLCD), the downward-moving ion-leak energy (WILD), the charge-exchange energy (WCHEX), the characteristic magnetic tube radii for loss-cone particles (R_{lc}) and ion-leak particles (R_{il}), the minimum (v_1) and maximum (v_2) velocities in the loss-cone energy spectrum, and the residual energy available for UV and thermal energies.

If $WLCD > 10^{-4}$ MT, then Step 2 is a call to Subroutine CONSPC to compute the histogram energy distribution for the loss-cone particles and Step 3 is a call to Subroutine BLINE to deposit the loss-cone particle energies in a spatial tube centered about the event-point field line. Subroutines CONJUG, BFIELD, and INDEX aid in the field-line tracing while Subroutine DEPO does the particle energy deposition in a grid cell and detects the stopping locations of the monoenergetic energy groups. Subroutine XYZGEO performs the necessary transformation from tangent-plane cartesian coordinates to geocentric cartesian coordinates. When

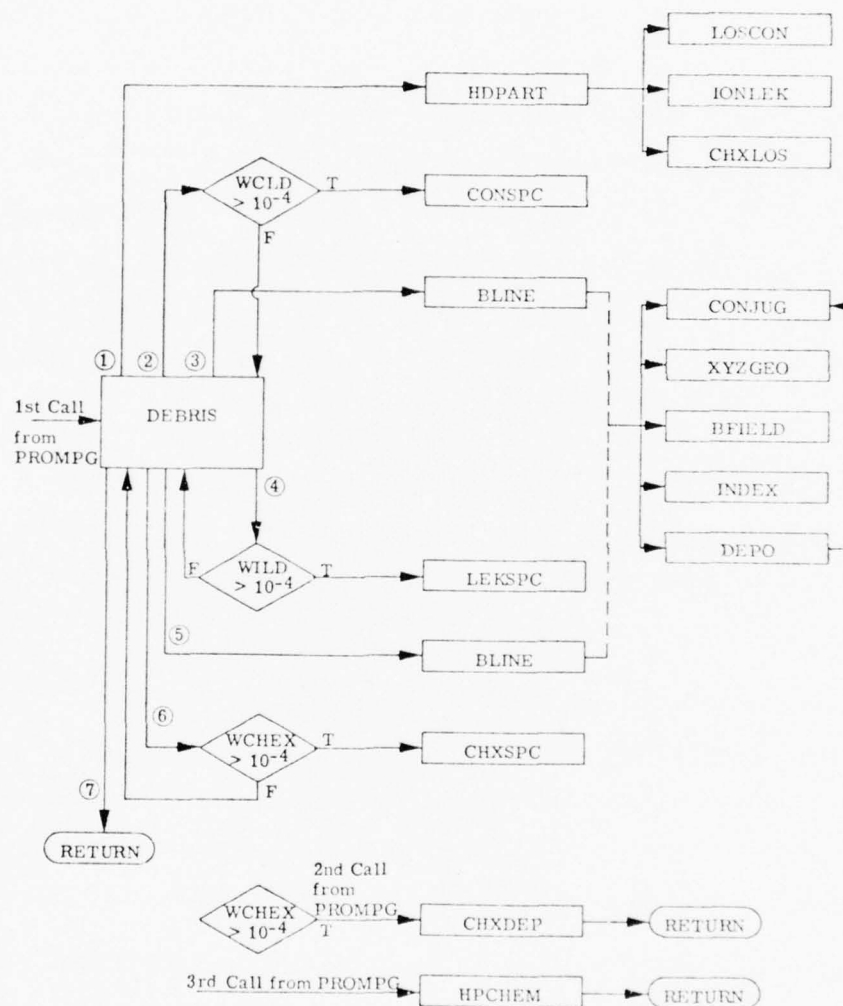


Fig. 9. Simplified Flow Chart of Debris-Related Routines.

control returns from Subroutine BLINE to Subroutine DEBRIS, every cell that is intersected by the loss-cone magnetic tube has a contribution to its specific energy.

If $WILD > 10^{-4}$ MT, then Step 4 is a call to Subroutine LEKSPC to compute the histogram energy distribution for the ion-leak particles and Step 5 is a call to Subroutine BLINE to deposit the ion-leak particle energies in a spatial tube centered about the event-point field line. The operational procedure of Subroutine BLINE is identical to the loss-cone case except that the heavy particles are considered to have mass number 16 rather than the mass number 27 of the loss-cone particles. After specific-energy contributions are added to cells intersected by the ion-leak tube, control is returned from Subroutine BLINE to Subroutine DEBRIS.

If $WCHEX > 10^{-4}$ MT, then Step 6 is a call to Subroutine CHXSPC to compute the histogram energy distribution of the CHEX particles for later use by Subroutine CHXDEP. Step 7 is the return to Subroutine PROMPG.

The second call from Subroutine PROMPG to the debris module is to Subroutine CHXDEP, provided $WCHEX > 10^{-4}$ MT; otherwise the call is bypassed. Contributions to the specific energy by CHEX particles are assigned to every grid cell, provided the areal density to the cell is less than the range of the most energetic CHEX particle.

The third call from Subroutine PROMPG is then made. Contributions to cell specific energy by the three particle sources are summed for the production of changes in the chemical species, thermal energy, and excitation energy. These latter two calls from Subroutine PROMPG are conveniently made just prior to the UV photon deposition since the necessary cell-calling logic is the same.

Detailed flow charts for Subroutines BLINE, DEPO, and CHXDEP are given in Figs. 10, 11, and 12, respectively.

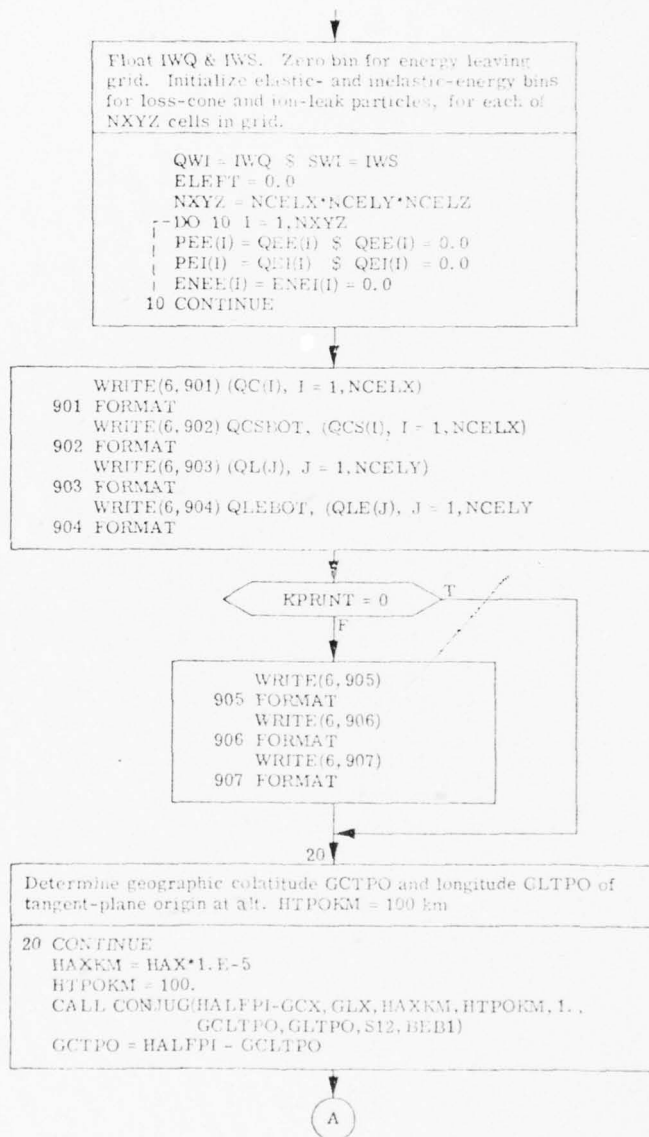


Fig. 10. Flow Chart for Subroutine BLINE(NXCEL, RR).

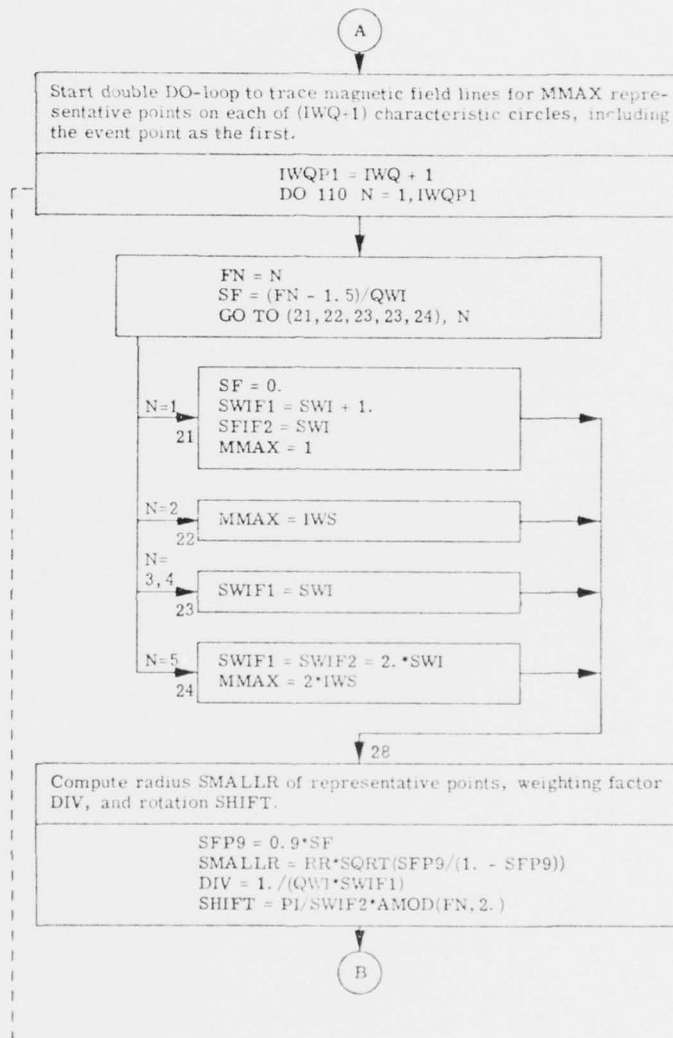


Fig. 10. (Continued).

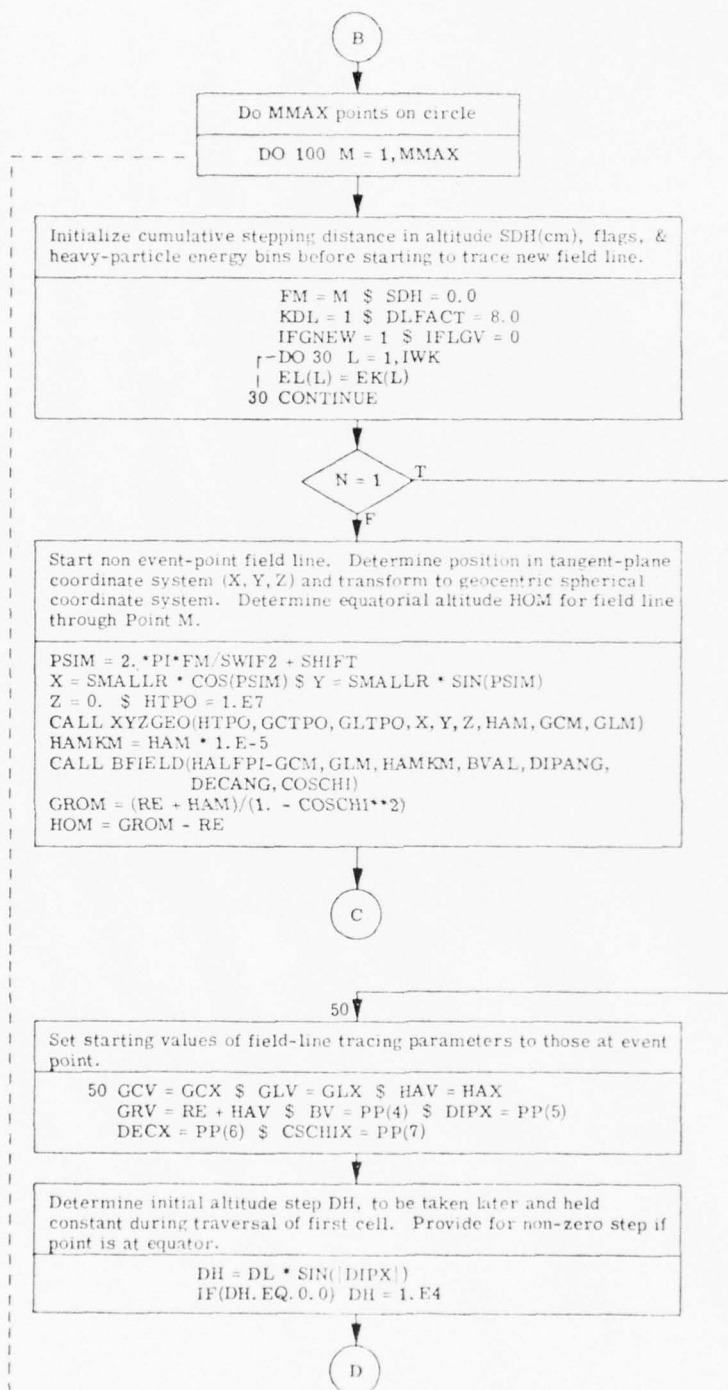


Fig. 10. (Continued).

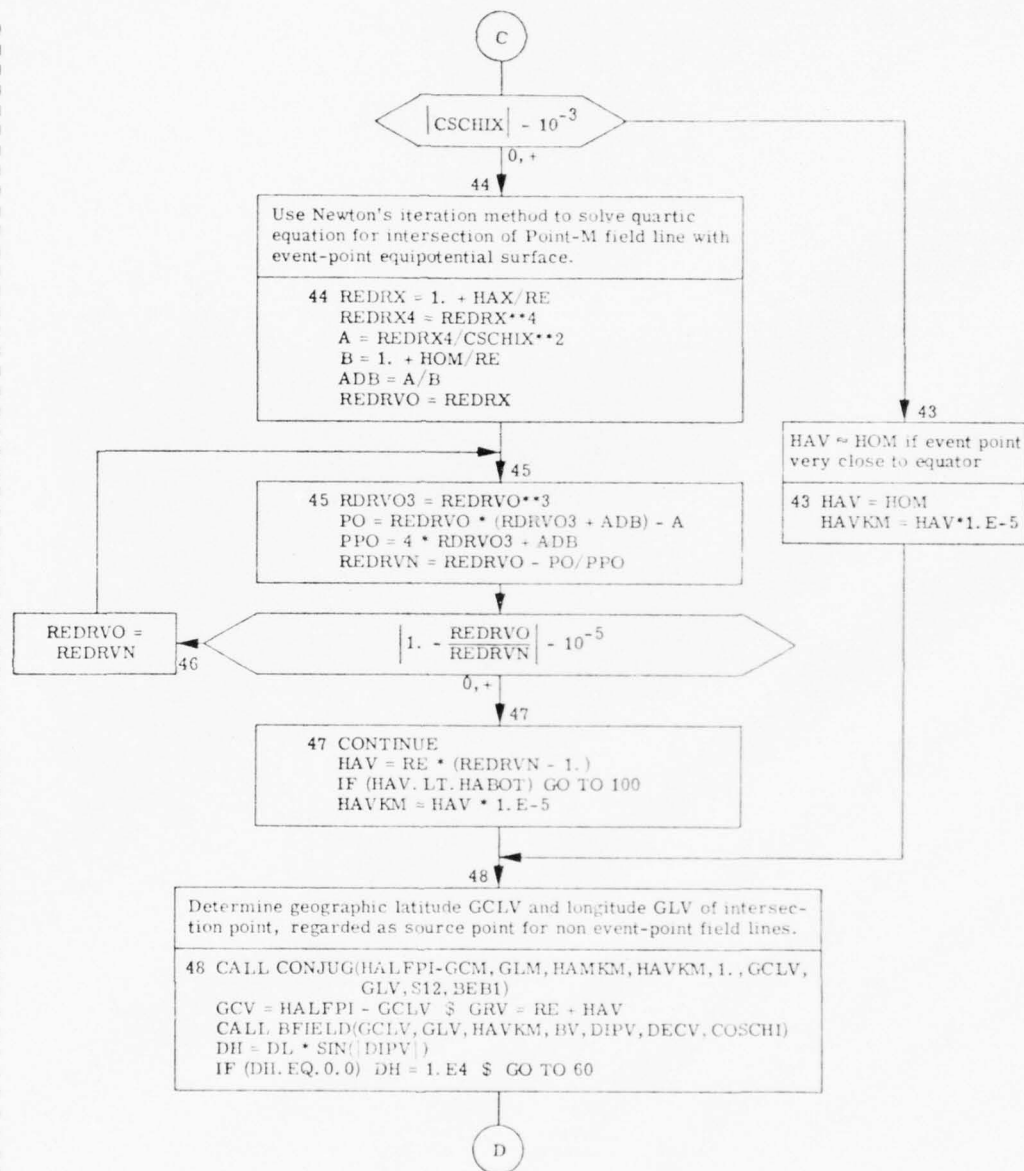


Fig. 10. (Continued).

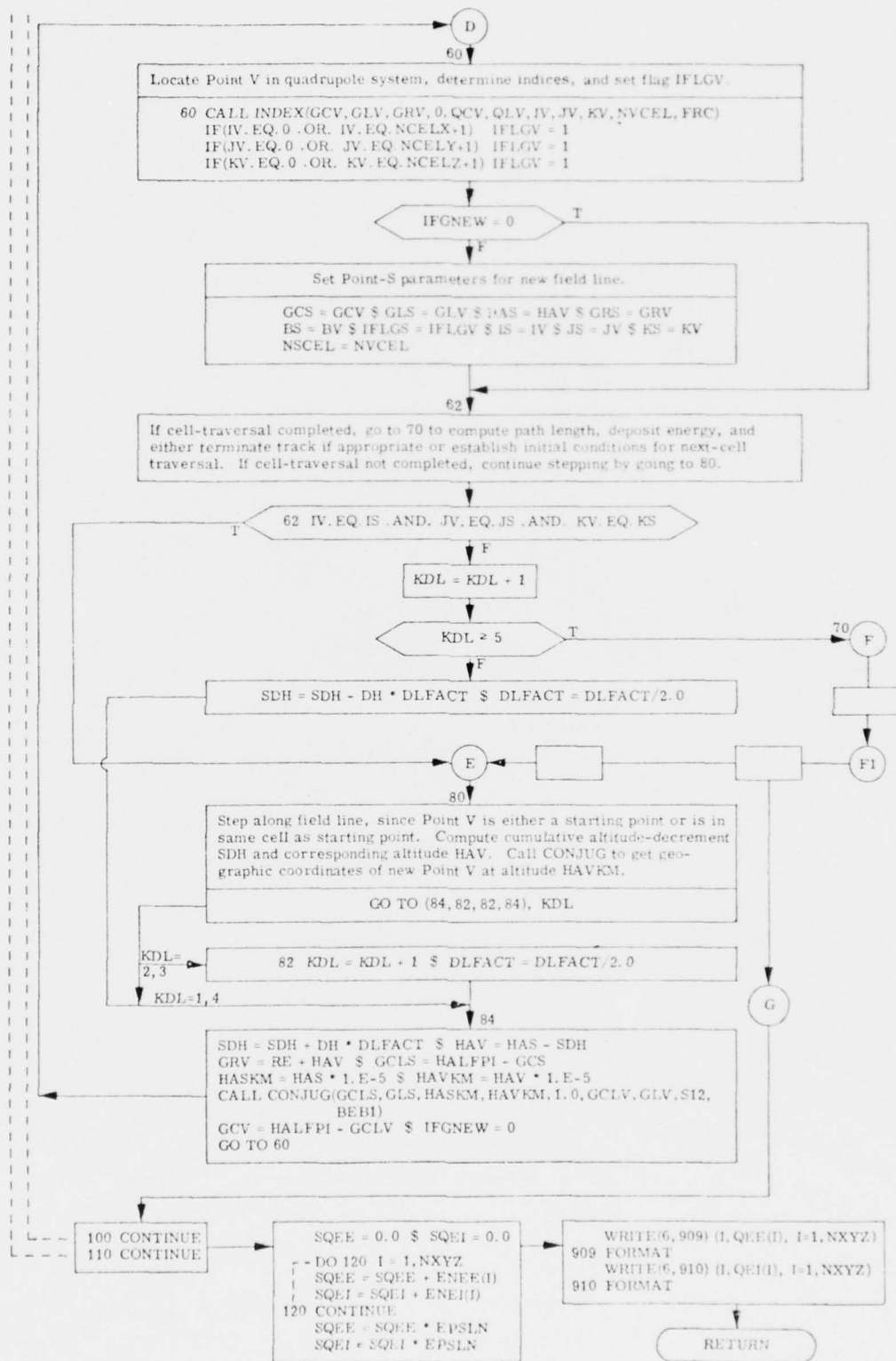


Fig. 10. (Continued).

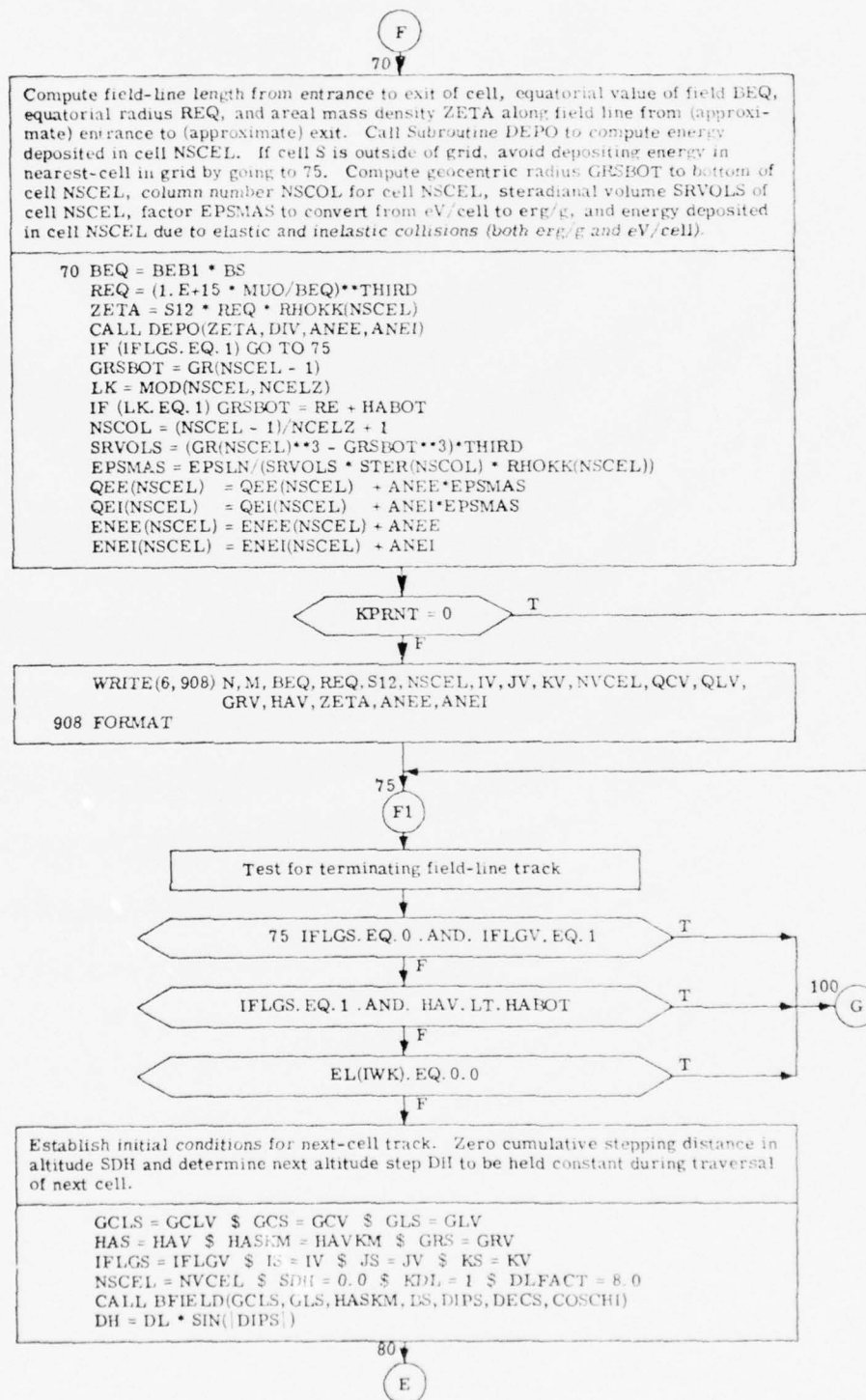


Fig. 10. (Continued).

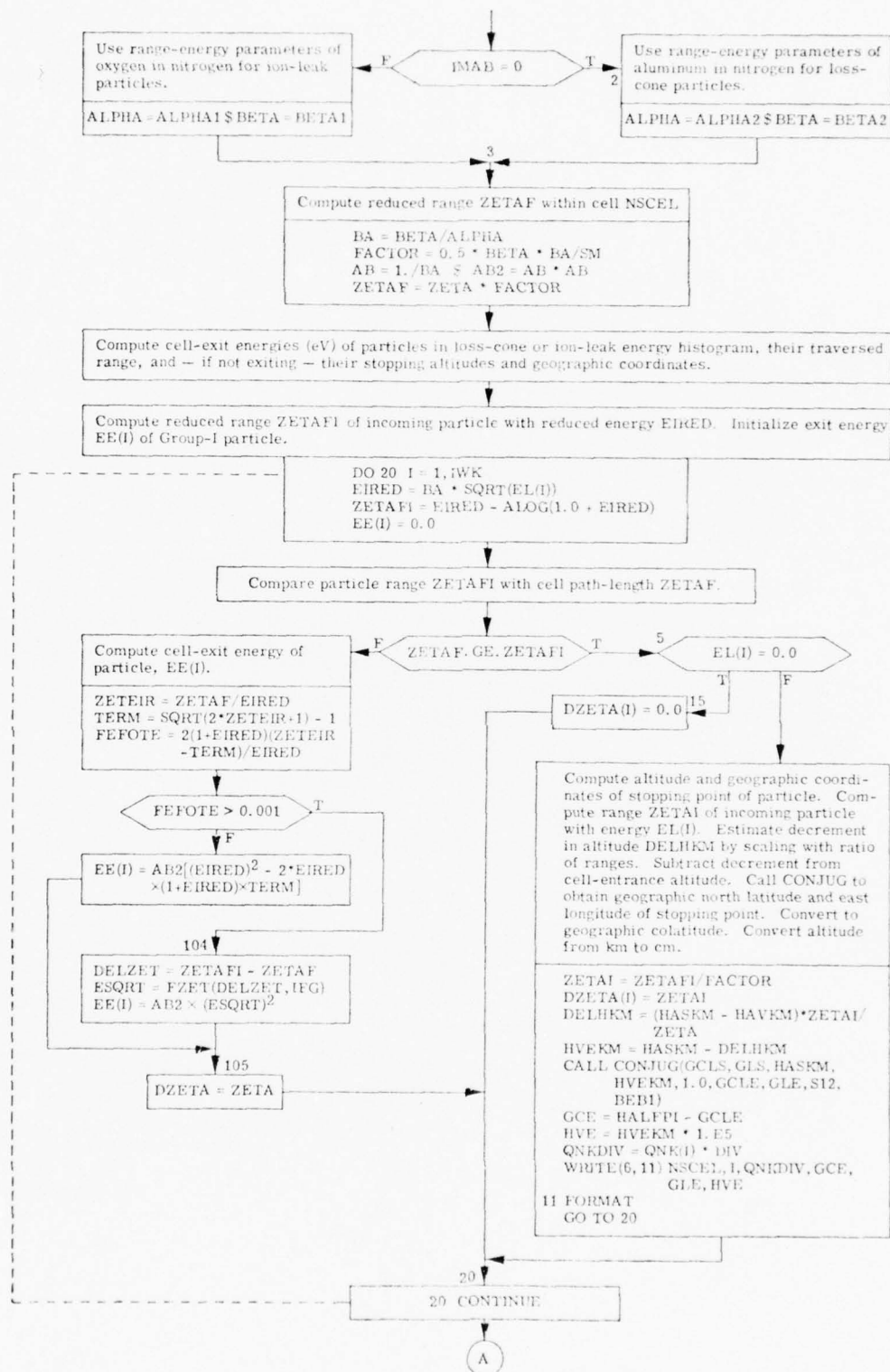


Fig. 11. Flow Chart for Subroutine DEPO(ZETA, DIV, ANEE, ANEI).

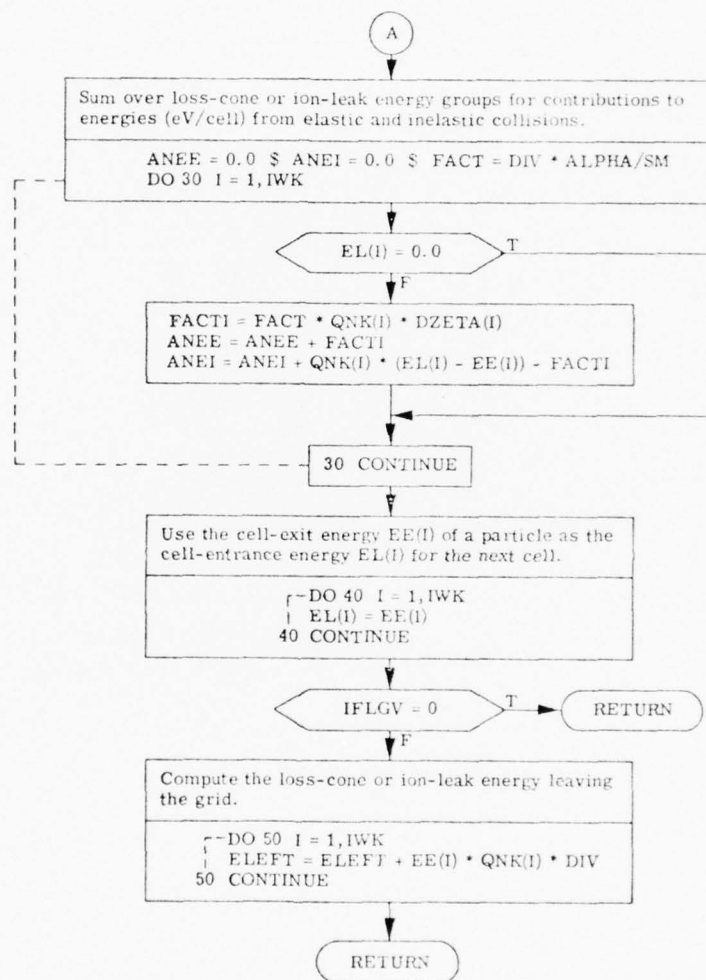


Fig. 11. (Continued)

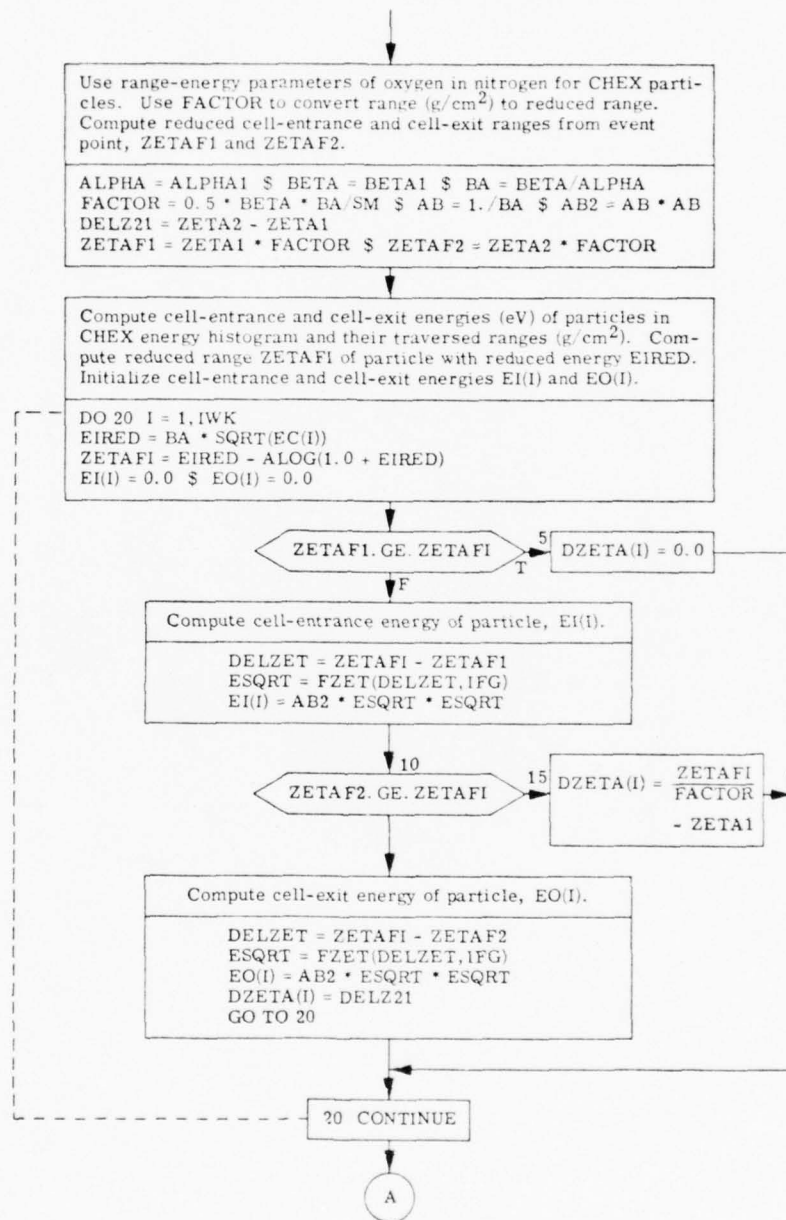


Fig. 12. Flow Chart for Subroutine CHXDEP(NCEL).

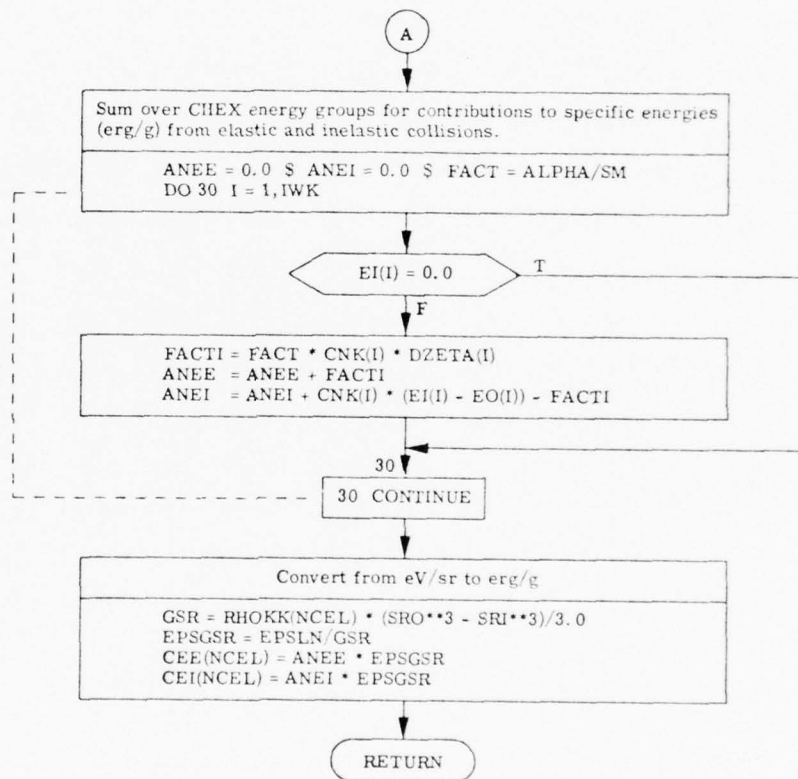


Fig. 12. (Continued).

9. UV DEPOSITION

The total computation of UV deposition requires Subroutine EUXFIT for finding the energy in each of the five Group-U subgroups, Subroutine PLINE for tracing ray paths from the event point through the center of each of the cells in the HAG, Subroutine PINT to compute integrals of mass density and species number densities along these ray paths, Subroutine BEDGE to find the radius (B-edge) within which only atomic ions are formed and to compute line integrals of species densities within the B-edge, Subroutine PHEAT to compute the photon fluences of the Group-U subgroups and to compute the total pressure due to the Group-U energy deposition (and to combine it with the original pressure and that due to Groups X and H), and Subroutine PCHEM to compute the prompt chemistry associated with the Group-U deposition (and to combine these results with those due to Groups X and H).

9.1 COMPUTATION OF RAY PATHS THROUGH THE HAG (SUBROUTINE PLINE)

9.1.1 Introduction

Subroutine PLINE traces ray paths through the HAG. A ray path starts at the event point, passes through the center of a selected HAG cell regarded as a target cell, and ends as the ray leaves the target cell. We must compute the length of each of the line segments formed by the intersection of the ray with the intervening cell boundary surfaces. Target cells are selected by Subroutine PROMPG by systematically looping over all the cells in the HAG.

9.1.2 Transformation from the Quadrupole Coordinate System to the Associated Geocentric Cartesian System

In Volume 16, we have introduced the quadrupole coordinate system and given many of the details. Here, as shown in Fig. 13, we need to convert from quadrupole coordinates (quadrupole colatitude φ and quadrupole east longitude θ) and geocentric radius r to the corresponding geocentric cartesian system in which the Z axis is through the quadrupole north pole and the X axis is through the quadrupole west pole.

The required transformation equations are

$$x = r \sin a \cos \theta$$

$$y = r \sin a \sin \theta$$

$$z = r \cos a ,$$

where $\sin a$ is obtained by first applying the law of sines to triangle P-QN-QW to obtain

$$\begin{aligned} \sin a &= \sin \varphi \sin 90^\circ / \sin \lambda \\ &= \sin \varphi / (1 - \cos^2 \lambda)^{\frac{1}{2}} \end{aligned}$$

and then the law of cosines for angles to obtain

$$\cos \lambda = -\cos \varphi \cos \theta$$

so that

$$\sin a = \sin \varphi / (1 - \cos^2 \varphi \cos^2 \theta)^{\frac{1}{2}} .$$

We also have

$$\cos a = \text{SIGN}(1.0, \cos \varphi) (1 - \sin^2 a)^{\frac{1}{2}} .$$

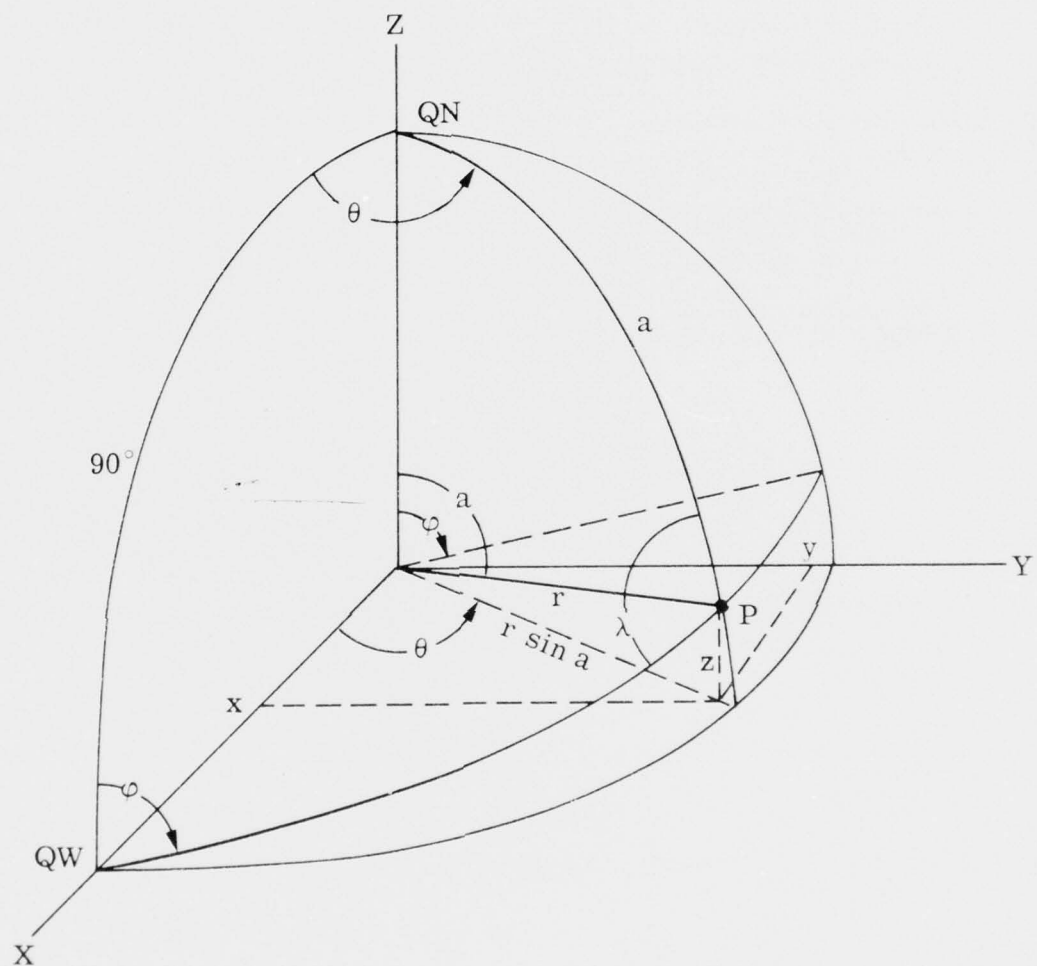


Fig. 13. Diagram Illustrating the Transformation from the Quadrupole Coordinate System to the Corresponding Geocentric Cartesian System.

9.1.3 Cell Shape

As explained in Volume 16, for a cell in the HAG, the top and bottom surfaces are geocentric spherical surfaces and the four sides are meridian planes.

9.1.4 Basic Formulas for Slant Range from a Given Point to a Cell Boundary

There are three basic formulas, each one corresponding to the intersected boundary being (a) a top or bottom boundary, (b) a quadrupole colatitude boundary, or (c) a quadrupole east longitude boundary. The first case affords more complication than either of the remaining two, each of which is similar to the other.

The quantities we have as input are:

- a. Event-point quadrupole coordinates and, hence, cartesian coordinates
- b. Target-point quadrupole coordinates and, hence, cartesian coordinates
- c. Lateral cell-boundary quadrupole coordinates and top and bottom geocentric radii.

In each of the three types of boundary cases, the ray from the starting point (usually the event point, denoted by \vec{r}_1) through the target-cell center (denoted here by \vec{r}_3) is specified by its direction cosines,

$$\cos \alpha = (x_3 - x_1)/r_{13}$$

$$\cos \beta = (y_3 - y_1)/r_{13}$$

$$\cos \gamma = (z_3 - z_1)/r_{13} ,$$

where

$$r_{13} = \left[(x_3 - x_1)^2 + (y_3 - y_1)^2 + (z_3 - z_1)^2 \right]^{\frac{1}{2}} .$$

9.1.4.1 Slant Range of a Ray Intersecting a Cell Top- or Bottom-Boundary. Consider a Point 2 with geocentric radius r_2 on the ray P_1P_3 , shown in Fig. 14. The angle δ between the vectors \vec{r}_1 and $\vec{r}_{12} = \vec{r}_2 - \vec{r}_1$ is specified in terms of the direction cosines of the unit vectors \hat{r}_1 and \hat{r}_{12} by the relation

$$\begin{aligned}\hat{r}_1 \cdot \hat{r}_{12} = \cos \delta &= \frac{x_1}{r_1} \cos \alpha + \frac{y_1}{r_1} \cos \beta + \frac{z_1}{r_1} \cos \gamma \\ &= \frac{x_1 \cos \alpha + y_1 \cos \beta + z_1 \cos \gamma}{(x_1^2 + y_1^2 + z_1^2)^{\frac{1}{2}}}\end{aligned}$$

From the right triangle OPP_2 in Fig. 14, we have

$$(r_1 \sin \delta)^2 + (r_1 \cos \delta + r_{12})^2 = r_2^2$$

or

$$DSRR \equiv r_{12} = -S2 + FGR \sqrt{WS2}$$

where

$$WS2 = (S2)^2 + (GR2)^2 - GR12$$

$$S2 = r_1 \cos \delta$$

$$GR2 = r_2$$

$$GR12 = r_1^2$$

and FGR is chosen to select the positive root or the smaller of the two positive roots.

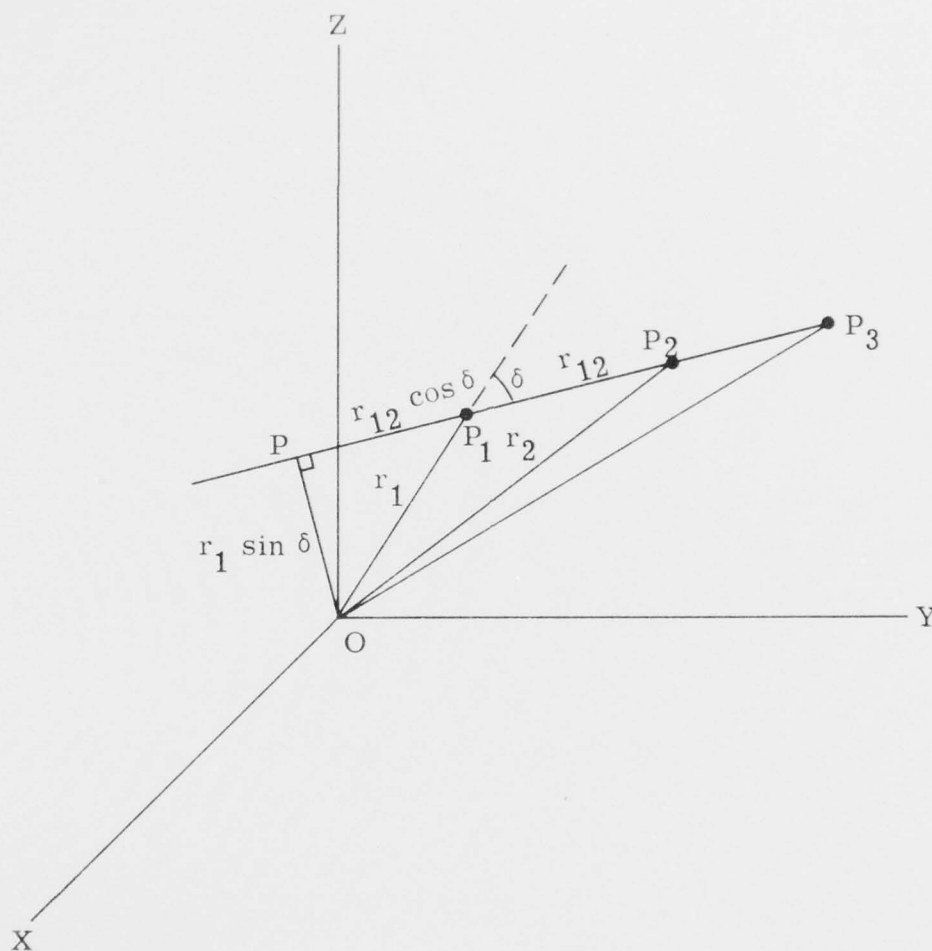


Fig. 14. Geometry Used in Deriving Slant Range of a Ray Intersecting a Cell Top- or Bottom-Boundary.

9.1.4.2 Slant Range of a Ray Intersecting a Cell North- or South-Boundary (Specified by Quadrupole Colatitude). In this case we are given the quadrupole colatitude (φ_2) of the Point 2. In Fig. 15, the line segment P_1P_2 is projected onto the YZ plane. Thus,

$$\tan \varphi_2 = \frac{\sin \varphi_2}{\cos \varphi_2} = \frac{y_2}{z_2} = \frac{y_1 + r_{12} \cos \beta}{z_1 + r_{12} \cos \gamma}$$

or

$$\text{DSRC} \equiv r_{12} = \frac{y_1 \cos \varphi_2 - z_1 \sin \varphi_2}{\cos \gamma \sin \varphi_2 - \cos \beta \cos \varphi_2}$$

9.1.4.3 Slant Range of a Ray Intersecting a Cell East- or West-Boundary (Specified by Quadrupole East Longitude). In this case we are given the quadrupole east longitude (θ_2) of the Point 2. In Fig. 16, the line segment P_1P_2 is projected onto the XY plane. Thus,

$$\tan \theta_2 = \frac{\sin \theta_2}{\cos \theta_2} = \frac{y_2}{x_2} = \frac{y_1 + r_{12} \cos \beta}{x_1 + r_{12} \cos \alpha}$$

or

$$\text{DSRL} \equiv r_{12} = \frac{y_1 \cos \theta_2 - x_1 \sin \theta_2}{\cos \alpha \sin \theta_2 - \cos \beta \cos \theta_2}$$

9.1.5 A Caution for Energy Deposition in the Event-Point Cell

The nominal cell heights for both SAIHYD and NRLHYD, under both initial and rezone conditions, are given in Tables 2 and 4 of Volume 16. From these tables it is seen that the cell thicknesses for most of the cells (and especially for the lower-altitude cells) are much smaller than the typical horizontal dimensions of the columns which may

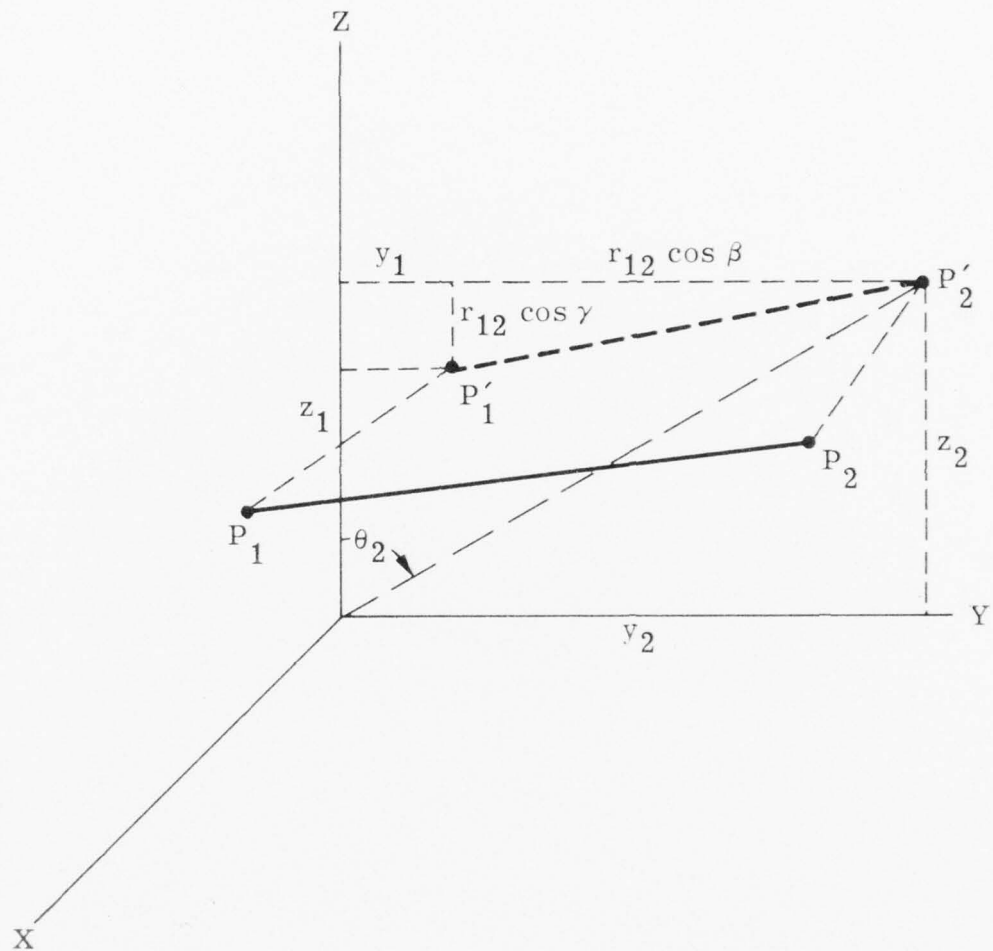


Fig. 15. Geometry Used in Deriving Slant Range of a Ray Intersecting a Cell North- or South-Boundary (Specified by Quadrupole Colatitude θ_2). The segment P_1P_2 is projected onto the YZ plane.

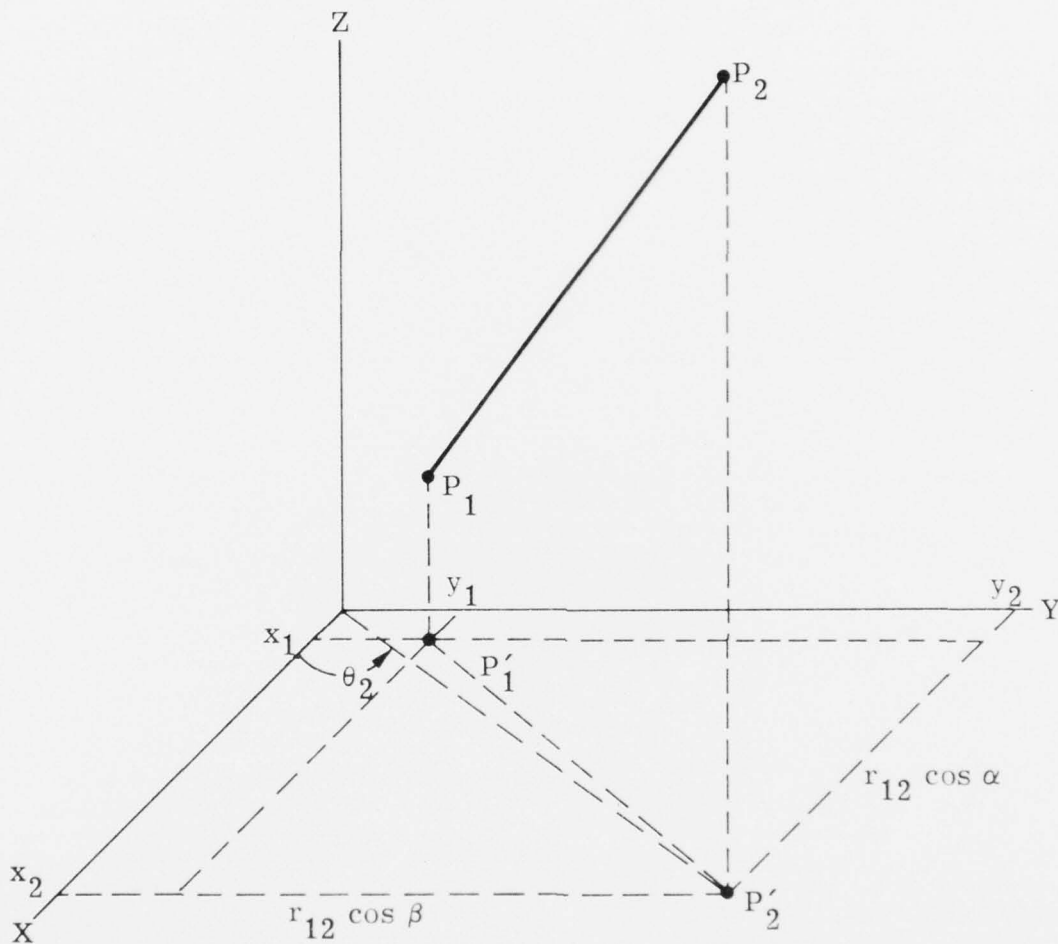


Fig. 16. Geometry Used in Deriving Slant Range of a Ray Intersecting a Cell East- or West-Boundary (Specified by Quadrupole East Longitude θ_2). The segment P_1P_2 is projected onto the XY plane.

be on the order of 100 km. For a small-energy event in the lower-altitude cells, it would be quite possible to put more energy into a cell than was available from the event, owing to using a path length that was unrepresentatively small. We tried an interim procedure to relieve this situation, but the undesirable side effects led us to delete the procedure. Thus, we alert the user to this potential problem which deserves review and more study.

9.1.6 Directional Flags and Indices of Next Set of Boundaries to be Intersected

In Subroutine PLINE we use the following directional flags:

<u>Index</u>	<u>Value</u>	<u>Ray Moves</u>
IINC	$\begin{cases} +1 \\ -1 \end{cases}$	southward northward
JINC	$\begin{cases} +1 \\ -1 \end{cases}$	eastward westward
KINC	$\begin{cases} +1 \\ -1 \end{cases}$	upward downward

The initial value of KINC is saved as the variable KINC0.

The indices I, J, K are used to denote the next possible set of boundaries to be intersected by the ray. In starting from the event cell (IEC, JEC, KEC), these boundary indices are initially defined as

$$\begin{aligned} I &= IEC - (1 - IINC)/2 \\ J &= JEC - (1 - JINC)/2 \\ K &= KEC - (1 - KINC)/2 . \end{aligned}$$

A value of 1 (instead of 0) for the flag IEND denotes that the last step in the line integral has been reached.

The index II is used to denote the number of boundaries intersected by the ray from the event point to the exit boundary of the target cell.

9.1.7 Flow Charts of Subroutine PLINE

Figure 17 is a simplified flow chart of Subroutine PLINE which includes calls to Subroutines PINT and BEDGE. Figure 18 is another simplified flow chart of Subroutine PLINE that gives information only about the computation of the ray-path segments.

9.1.8 Miscellaneous Functions of Subroutine PLINE

Other miscellaneous related tasks performed by Subroutine PLINE include the following:

- a. Set Group-U subgroup index (IGROUP) to 5.
- b. Zero integrals (SNR2(L), FLUX(L), L=1,5) computed in Subroutine BEDGE.
- c. Zero integrals (SN2INT, SO2INT, SNINT, SOINT, RHOINT, O2INT) computed in Subroutine PINT.
- d. Set flag (IUFLAG) denoting whether or not the B-edge has been passed.
- e. Zero integral (SR) for distance from event point to cell entry-point.

9.2 COMPUTATION OF INTEGRALS OF SPECIES NUMBER DENSITIES AND MASS DENSITIES ALONG THE RAY PATH (SUBROUTINE PINT)

For the line path SRN calculated by Subroutine PLINE, Subroutine PINT integrates the species number densities and mass densities as follows:

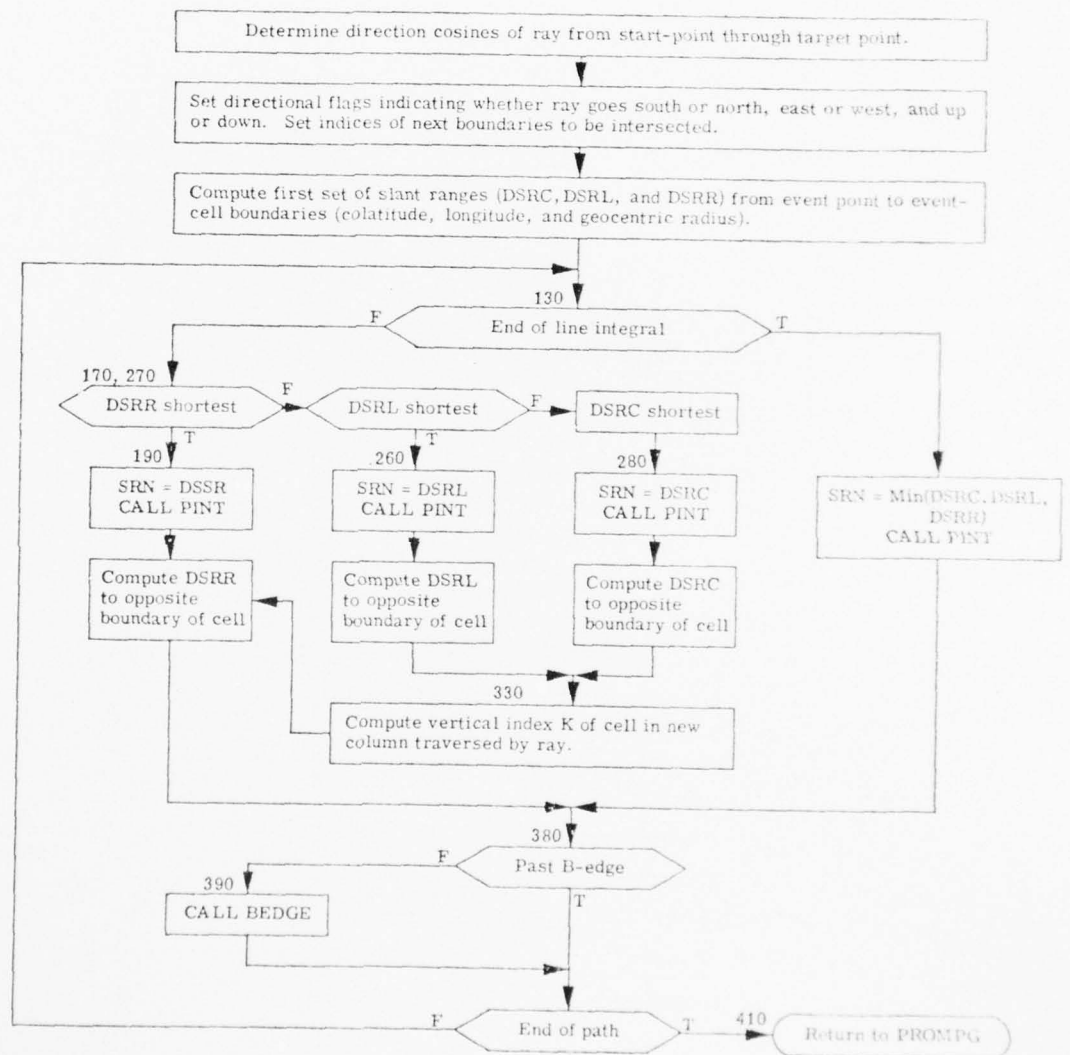


Fig. 17. Simplified Flow Chart of Subroutine PLINE, Including Calls to Subroutines PINT and BEDGE.

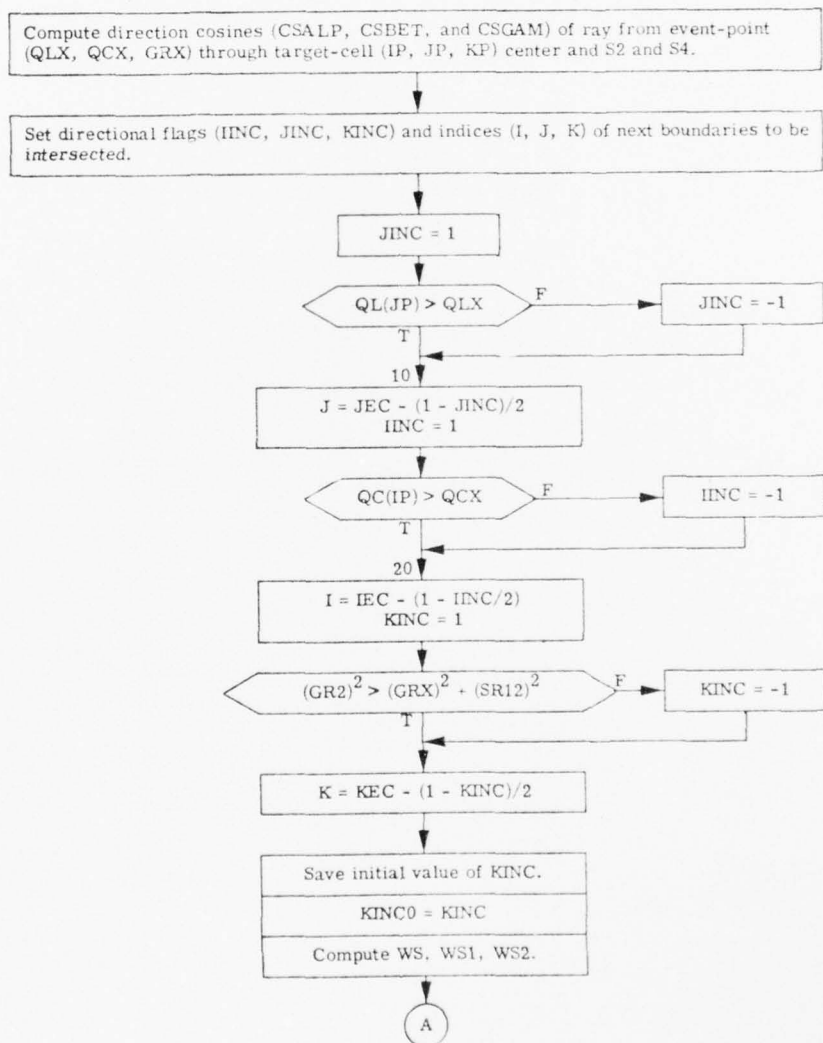


Fig. 18. Simplified Flow Chart of Subroutine PLINE. Only steps pertaining to ray-path segments are shown.

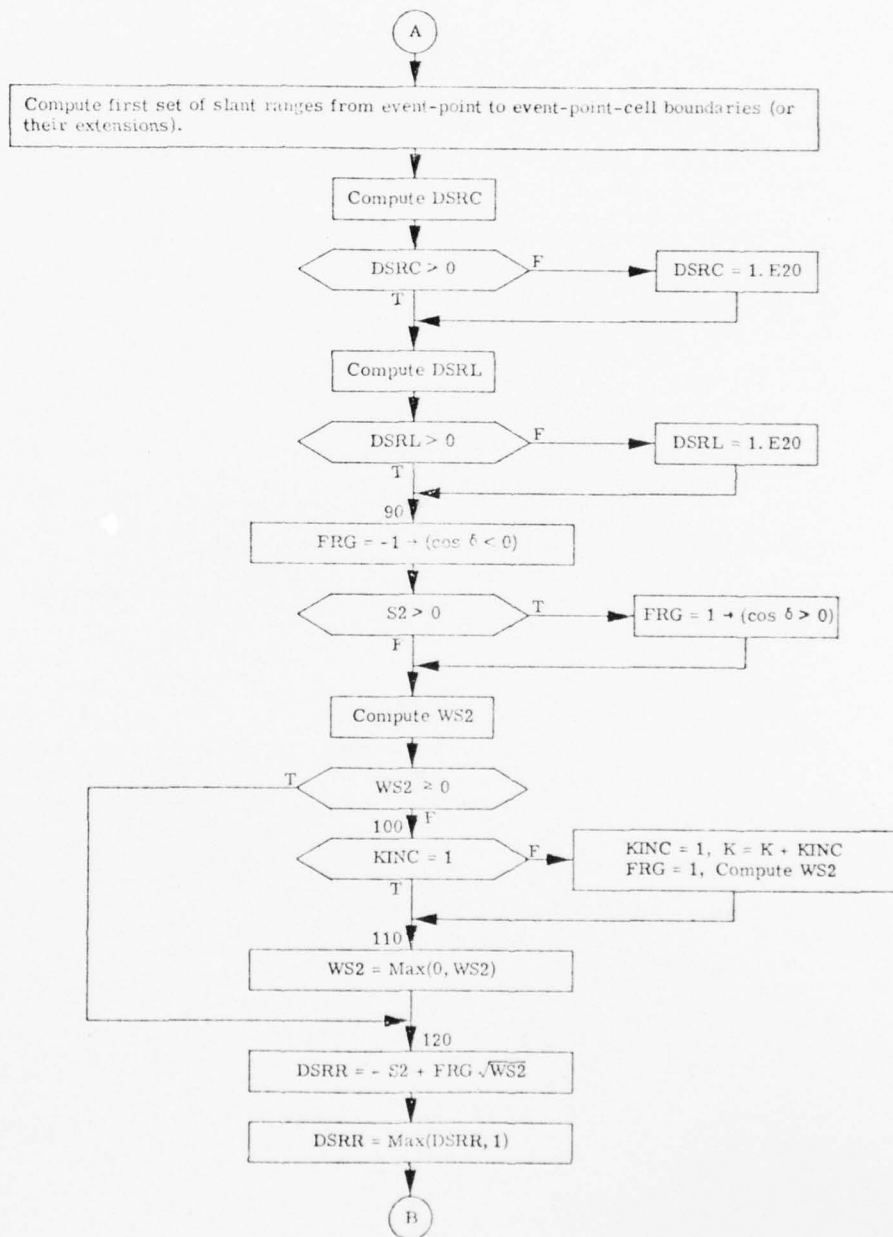
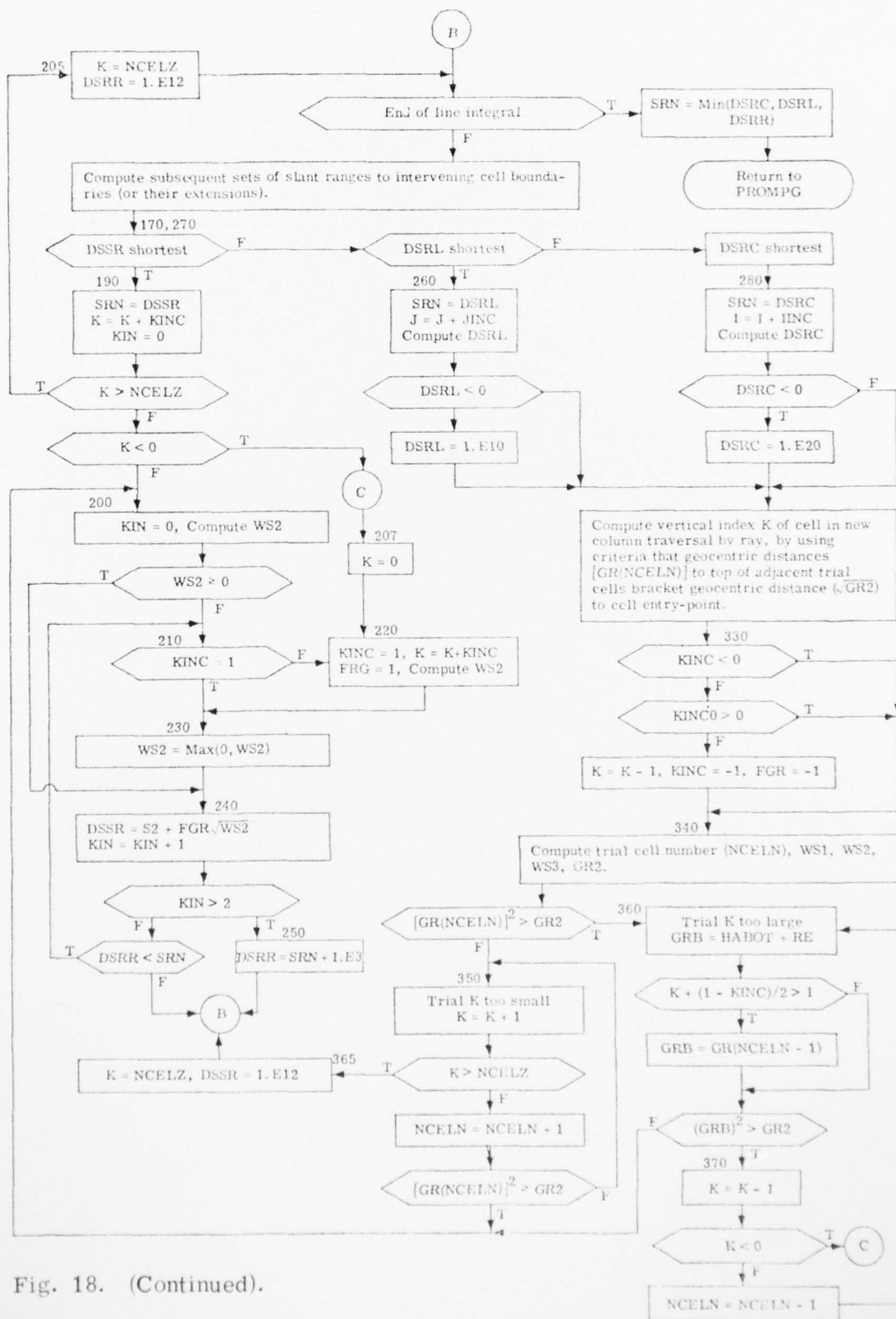


Fig. 18. (Continued).



$$\text{SN2INT} = \int_0^{\text{SRN}} [\text{N}_2] \, dr , \quad \text{cm}^{-2}$$

$$\text{SO2INT} = \int_0^{\text{SRN}} [\text{O}_2] \, dr , \quad \text{cm}^{-2}$$

$$\text{SNINT} = \int_0^{\text{SRN}} [\text{N}] \, dr , \quad \text{cm}^{-2}$$

$$\text{SOINT} = \int_0^{\text{SRN}} [\text{O}] \, dr , \quad \text{cm}^{-2}$$

$$\text{RHOINT} = \int_0^{\text{SRN}} \rho \, dr , \quad \text{g/cm}^2$$

$$\text{O2INT} = \int_0^{\text{SRN}} \rho_{\text{O}_2} \, dr , \quad \text{g/cm}^2$$

The variables for these integrals are zeroed in Subroutine PLINE. Over a ray segment between SR and SRN, the corresponding contributions to the integrals are, respectively, DSN2I, DSO2I, DSNi, DSOi, DHR0I, and DO2INT. SPECIE(I) denotes the concentration of N_2 , O_2 , N, and O, respectively, for $I = 1, 2, 3$, and 4.

When the properties of a particular cell are needed to perform the integrals Subroutine PINT calls Subroutine ECRD and transfers quantities 2 through 11 from large core memory to small core memory.

9.3 COMPUTATION OF THE ATOMIC-ION REGION (B-EDGE) FOR GROUP-U PHOTONS (SUBROUTINE BEDGE)

9.3.1 Introduction

As Subroutine PLINE computes the ray path from the event point to a target point, Subroutine BEDGE is employed to determine the radius (SRR(2)) of the edge (B-edge) of the region within which Group-U ionizing photons are very strongly absorbed and produce entirely atomic ions. Subroutine BEDGE also computes (a) the line integrals, from the event point to the B-edge, of the O_2 -mass density (O2U) and of the species densities of N_2 (SN2U), O_2 (SO2U), N (SNU), and O (SOU), and (b) the number of ionizing-photon absorptions per steradian that are required to produce atomic ions alone for Group-U Subgroup-L (SNR2(L)).

9.3.2 Simplified Description of the Essence of Subroutine BEDGE

To simplify the description of the essence of Subroutine BEDGE, we introduce some terms, not all of which are used in the routine.

PHOTON(L) = Number of Subgroup-L photons emitted per steradian from the source.

PHOTAB(L) = Number of Subgroup-L photons per steradian used in developing the radius of the B-edge up to its current radius R_c .

ABSORP = Number of ionizing-photon absorptions per steradian required to increase the radius of the B-edge from its current value R_c to R.

XMUBAR(L) = Mass attenuation coefficient (cm^2/g) for Subgroup-L photons in Cell NCELS with neutral-particle mass-density RHON(NCELS).

$$= \frac{\sum_{I=1}^4 \text{SPECIE}(I) \times \text{SIGU}(L, I)}{\text{RHON}(\text{NCELS})}$$

(I = 1, 2, 3, 4 denotes N_2 , O_2 , N, O).

EVEN = Number of absorptions per cubic centimeter required to get atomic ions.

$$= 3 \sum_{I=1}^2 \text{SPECIE}(I) + \sum_{I=3}^4 \text{SPECIE}(I)$$

EVNPG = Number of absorptions per gram required to get atomic ions.

$$= \text{EVEN}/\text{RHON}(\text{NCELS})$$

If we want the Subgroup-L photons to produce all atomic ions at radius R, then the condition to be satisfied is

$$\frac{\text{PHOTON}(L) - \text{PHOTAB}(L) - \text{ABSORP}}{R^2} \times \text{XMUBAR}(L) = \text{EVNPG} .$$

Now, multiply both sides of the equation by $R^2/(\text{XMUBAR}(L) \times \text{EVEN})$ and define a new function EDGE(L) to be the difference between the right- and left-hand sides:

$$\text{EDGE}(L) = \frac{\frac{R^2 \times \text{EVNPG}}{\text{XMUBAR}(L)} - [\text{PHOTON}(L) - \text{PHOTAB}(L) - \text{ABSORP}]}{\text{EVEN}} .$$

A positive value for EDGE(L) is the steradianal volume in excess of that for which the Subgroup-L photons can produce all atomic ions. A negative value for EDGE(L) is the steradianal volume beyond radius R that the Subgroup-L photons can produce all atomic ions. A zero value for EDGE(L) means that the Subgroup-L photons have produced atomic ions exactly to the radius R.

If we recognize the fact that

$$\frac{\text{ABSORP}}{\text{EVEN}} = \frac{R^3 - R_c^3}{3} ,$$

then we can write EDGE(L) as

$$\text{EDGE}(L) = A_3 R^3 + A_2 R^2 + A_0$$

where

$$A_3 = 1/3$$

$$A_2 = 1/[\text{RHON}(\text{NCELS}) \times \text{XMUBAR}(L)]$$

$$A_0 = \frac{\text{PHOTAB}(L) - \text{PHOTON}(L)}{\text{EVEN}} - \frac{R_c^3}{3}.$$

The equation

$$3 \times \text{EDGE}(L) = 0$$

is solved for the radius R by using the standard Newton-Raphson iteration formula:

$$R_{i+1} = R_i - \frac{\text{EDGE}(L, R_i)}{d[\text{EDGE}(L, R_i)]/dR_i}.$$

9.3.3 Flow Charts of Subroutine BEDGE

Figures 19 and 20 are simplified and detailed flow charts of Subroutine BEDGE.

9.4 COMPUTATION OF GROUP-U SUBGROUP FLUENCES AND PROMPT HEATING (SUBROUTINE PHEAT)

For each cell in the HAG, Subroutine PHEAT computes the photon fluences of the Group-U subgroups and the total pressure due to the Group-U energy deposition and then combines this pressure with the pre-event pressure and the pressures due to Group-X and -H energy depositions.

AD-A043 547

GENERAL RESEARCH CORP SANTA BARBARA CALIF
THE ROSCOE MANUAL. VOLUME 17. HIGH-ALTITUDE DEBRIS-ENERGY DEPOS--ETC(U)
SEP 75 D A HAMLIN, J Y WANG, M R SCHOONOVER DNA001-74-C-0182
DNA-3964F-17 NL

UNCLASSIFIED

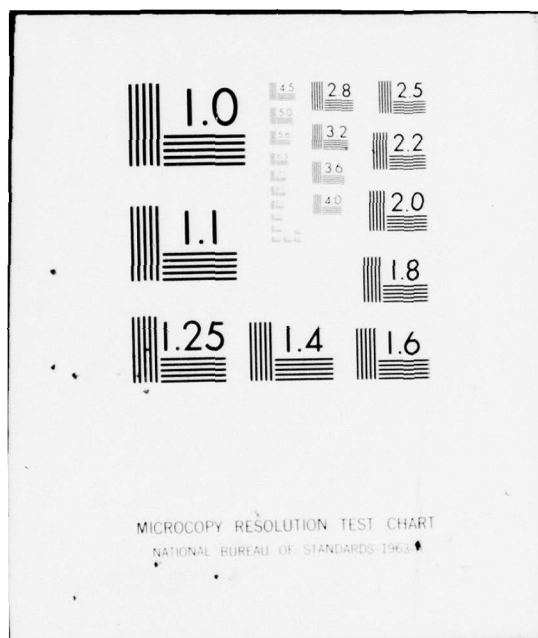
2 OF 2

AD
A043547



END
DATE
FILMED
9-77

DDC



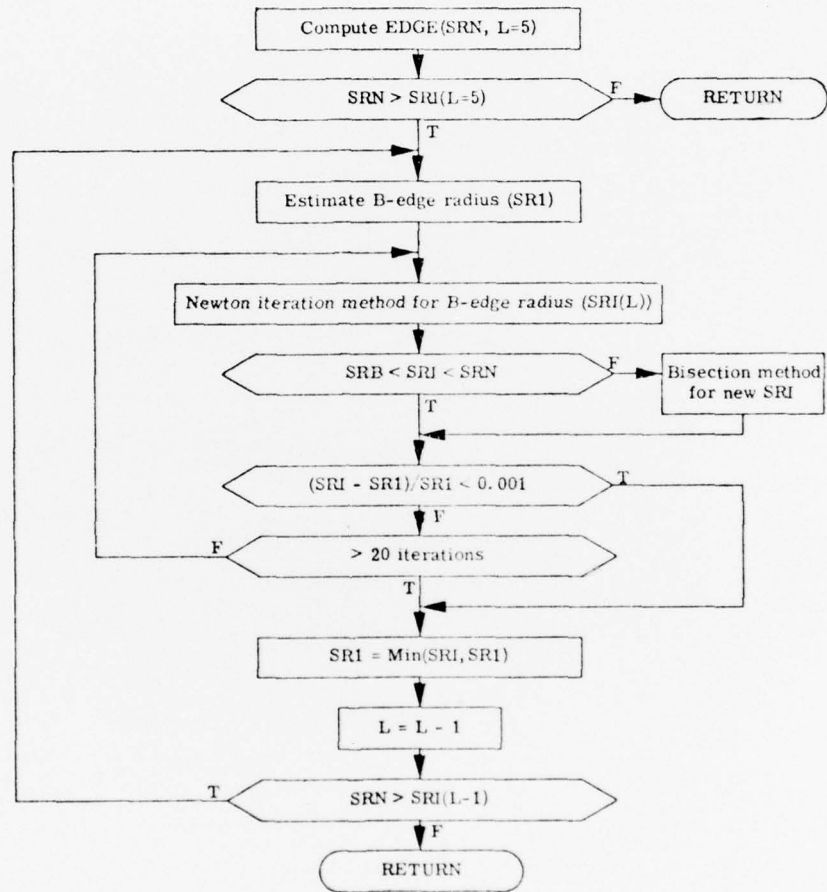


Fig. 19. Simplified Flow Chart of Subroutine BEDGE.

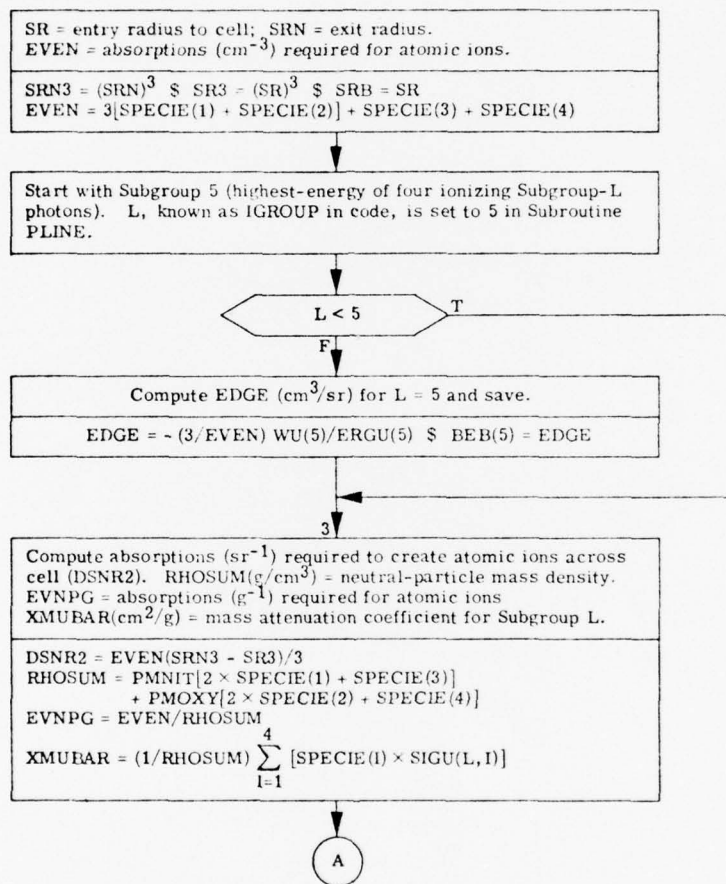


Fig. 20. Detailed Flow Chart of Subroutine BEDGE.

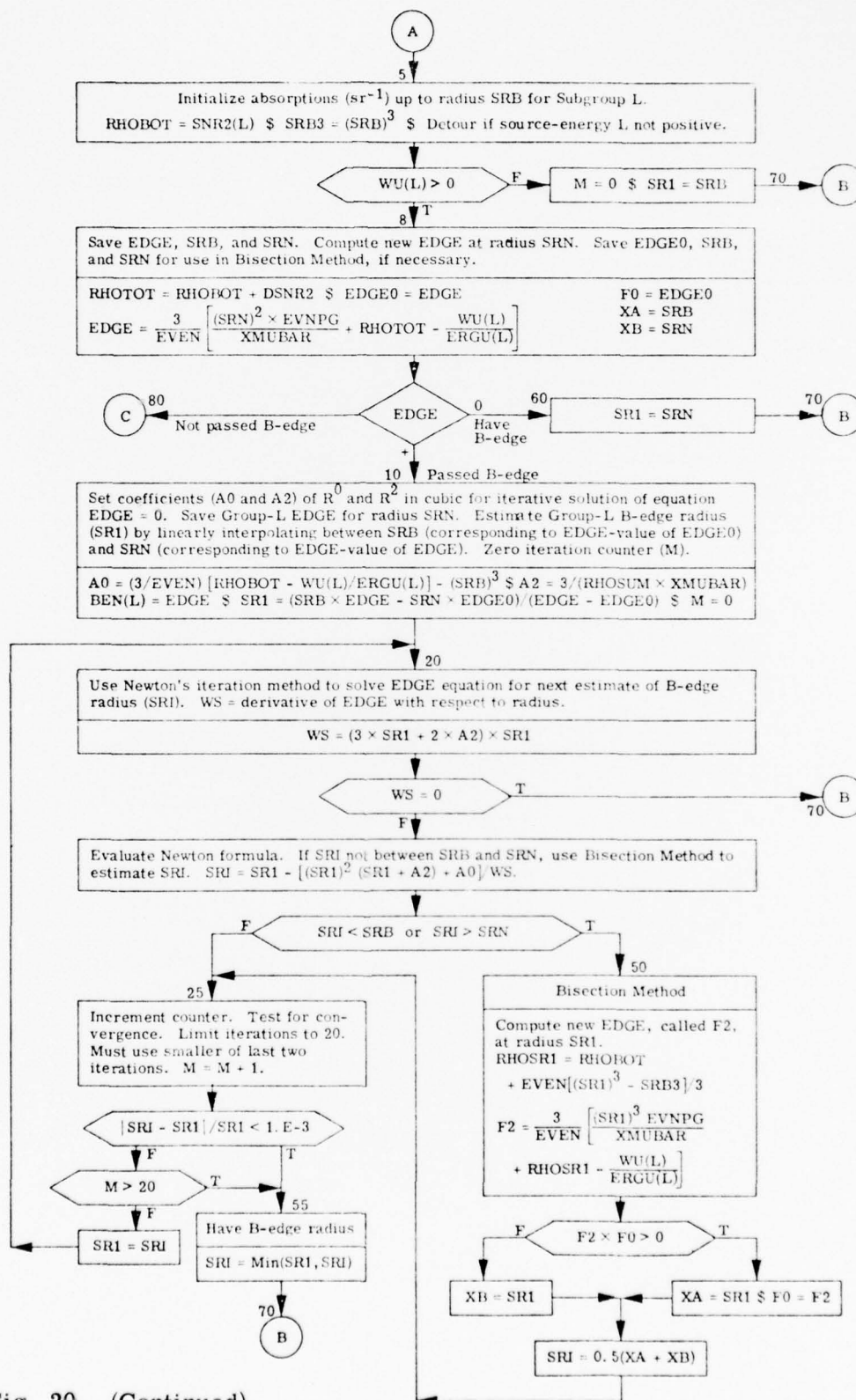


Fig. 20. (Continued).

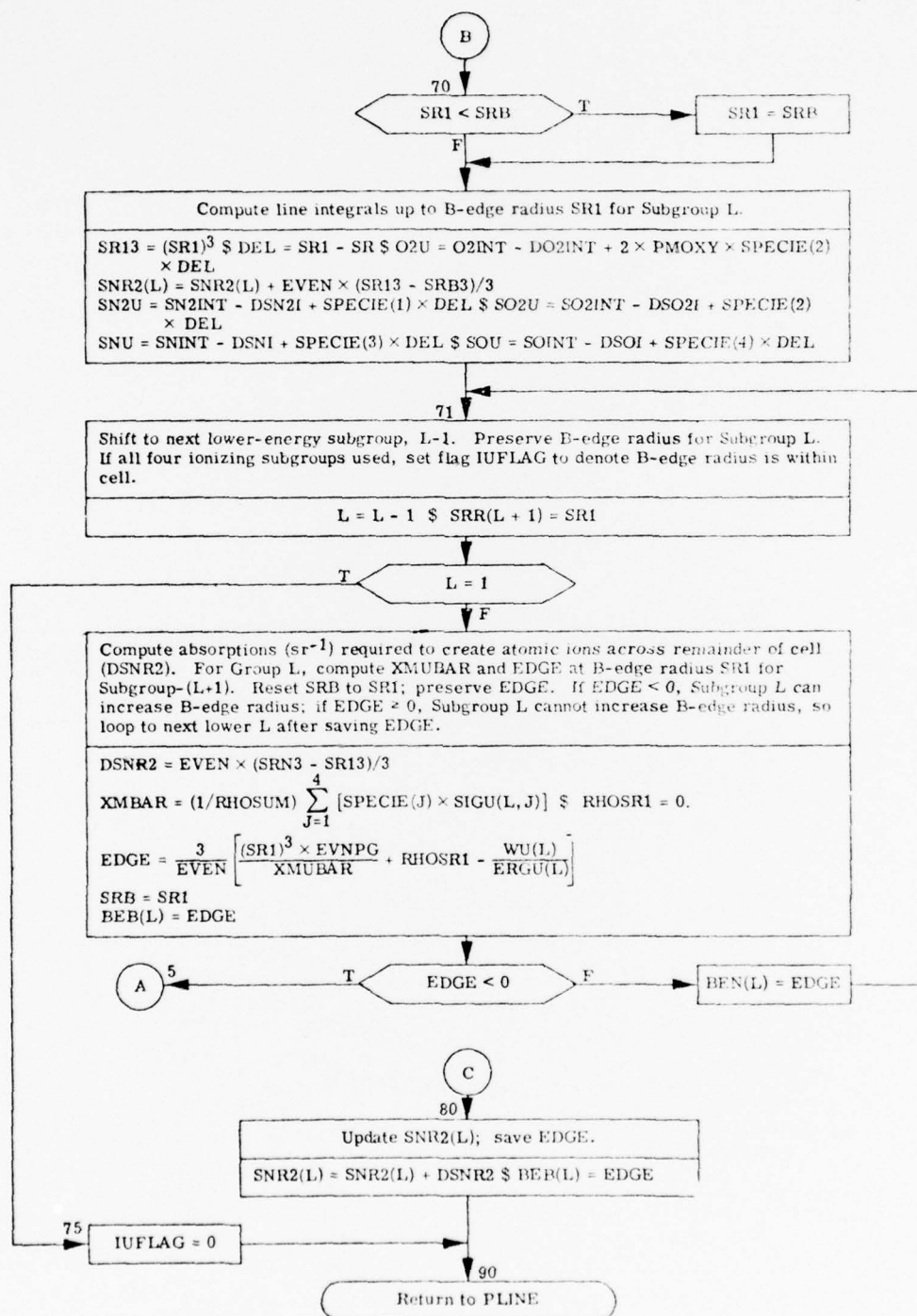


Fig. 20. (Continued).

9.4.1 Group-U Energy Deposition and Fluences

In computing the Group-U energy deposition (erg/g) in a target cell and the Group-U photon fluences (photons/cm²), we treat three cases:

Case 1 (B-edge radius (SRR(2)) smaller than target-cell entry-radius (SR))

We use the difference of the incident and exit values of the steradianal energy fluence for each Group-U subgroup, divided by the corresponding steradianal mass for the cell. We treat dissociating (Subgroup 1) and ionizing (Subgroups 2-5) separately.

For Subgroup 1,

$$\text{DAIX}(1) = \frac{\text{WU}(1)}{(\rho/3)(R_{\text{out}}^3 - R_{\text{in}}^3)} \{e^{-\text{XMU}1 \times \text{O2IN}} - e^{-\text{XMU}1 \times \text{O2OUT}}\} ,$$

where $\text{XMU}1(\text{cm}^2/\text{g})$ is the mass attenuation coefficient of O_2 for Subgroup-1 photons, O2IN and O2OUT are the areal mass densities of O_2 from the B-edge to the entry and exit points of the target cell.

The energy available for hydro due to Subgroup-1 absorption is

$$\text{DAIXU}(1) = \text{PREFF}(1, 2) \times \text{DAIX}(1) ,$$

where $\text{PREFF}(1, 2)$ is the pressure efficiency of O_2 (Species 2) absorbing Subgroup-1 photons.

For the target cell, the effective photon fluence for Subgroup 1, consistent with the energy deposition, is

$$\begin{aligned} \text{FLUX}(1) &= \frac{\rho}{\rho_{\text{O}_2}} \frac{\text{DAIX}(1) \times 2 \times \text{PMOXY}}{\text{ERGU}(1) \times \text{SIGU}(1, 2)} \\ &= \frac{\rho}{[\text{O}_2]} \frac{\text{DAIX}(1)}{\text{ERGU}(1) \times \text{SIGU}(1, 2)} , \end{aligned}$$

since

$$\frac{1}{[\text{O}_2]} = \frac{2 \times \text{PMOXY}}{\rho_{\text{O}_2}} .$$

For Subgroups 2 through 5, the Subgroup-L energy absorbed per gram is

$$\text{DAIX}(\text{L}) = \frac{\text{WU}(\text{L}) - \text{ERGU}(\text{L}) \times \text{SNR2}(\text{L})}{(\rho/3)(\text{R}_{\text{out}}^3 - \text{R}_{\text{in}}^3)} \{e^{-\text{SUMIN}(\text{L})} - e^{-\text{SUMOUT}(\text{L})}\} ,$$

where

$$\text{SUMIN}(\text{L}) = \sum_{\text{J}=1}^4 \text{SPECIN}(\text{J}) \times \text{SIGU}(\text{L}, \text{J})$$

$$\text{SUMOUT}(\text{L}) = \sum_{\text{J}=1}^4 \text{SPECOUT}(\text{J}) \times \text{SIGU}(\text{L}, \text{J})$$

and SPECIN(J) and SPECOUT(J) are the areal densities of the J-species from the B-edge to the cell entry-point and exit-point.

For Subgroup L, the average pressure efficiency for a target cell is defined as

$$\text{PEFBAR}(\text{L}) = \frac{\sum_{\text{J}=1}^4 \text{PREFF}(\text{L}, \text{J}) \times \text{SPECIE}(\text{J}) \times \text{SIGU}(\text{L}, \text{J})}{\sum_{\text{J}=1}^4 \text{SPECIE}(\text{J}) \times \text{SIGU}(\text{L}, \text{J})} .$$

The energy available for hydro due to Subgroup L is

$$\text{DAIXU}(\text{L}) = \text{DAIX}(\text{L}) \times \text{PEFBAR}(\text{L}) .$$

For the target cell the effective fluence for Subgroup-L photons, consistent with the energy deposition, is

$$\text{FLUX}(L) = \frac{\rho}{\sum_{J=1}^4 \rho_J} \frac{\text{DAIX}(L)}{\text{ERGU}(L) \times \text{XMU}(L)}$$

where

$$\text{XMU}(L) = \frac{\sum_{J=1}^4 \text{SIGU}(L, J) \times \text{SPECIE}(J)}{\sum_{J=1}^4 \rho_J} .$$

The total Group-U energy available for hydro is the sum of that for Subgroup-1 and that for Subgroups 2 to 5, i. e. ,

$$\text{DAIXU} = \sum_{L=1}^5 \text{DAIXU}(L) .$$

Case 2 (B-edge radius (SRR(2)) greater than target-cell exit-radius (SRN))

Inside the B-edge the internal energy is set by the expression

$$\text{DAIXU} = \text{SPINT}$$

where SPINT is set in Block Data BLOCKH. The HARC code used a value of 2.07×10^{12} erg/g, which we have reduced by a factor of 10, since 2.07×10^{12} erg/g corresponds to

$$\begin{aligned} \frac{2.07 \times 10^{12} \text{ erg/g}}{1.6 \times 10^{-12} \text{ erg/eV}} \cdot 2.325 \times 10^{-23} \text{ g/nitrogen atom} &= 30.08 \frac{\text{eV}}{\text{nitrogen atom}} \\ &= 15.04 \frac{\text{eV}}{\text{charged particle}} \end{aligned}$$

where $[\text{charged particle}] = \{[N^+] + [e]\}$. This energy per charged particle corresponds to a temperature of about 10 eV since the kinetic energy per particle is $(3/2) kT$. Thus, we have assumed that the particles inside the B-edge have a temperature equal to nearly 1 eV. We are neglecting the difference between the oxygen and nitrogen mass, but this approximation is satisfactory since the assumed value of about 1 eV is somewhat arbitrary.

We have no need for the Group-U fluences at a point inside the B-edge since it is assumed that only atomic ions exist there.

Case 3 (B-edge radius (SRR(2)) between target-cell entry-radius (SR) and exit-radius (SRN))

To obtain the specific energy available for hydro, we use a volume-weighted average of the values for the two portions of the cell inside and outside the B-edge. For the cell portion inside the B-edge, the specific energy is equal to SPINT, as in Case 2. For the cell portion outside the B-edge, the specific energy is determined in a manner similar to that for Case 1.

Again, we treat dissociating and ionizing subgroups separately.

For Subgroup 1 in the cell portion outside the B-edge, we have

$$DAIX(1) = \frac{WU(1)}{(\rho/3)(R_{out}^3 - R_{edge}^3)} \left\{ 1 - e^{-X_{MU1} \times O_{2OUT}} \right\}$$

where the subscript 'edge' denotes B-edge and the subscript 'out' has the same meaning as in Case 1.

For Subgroups 2 through 5 in the cell portion outside the B-edge, the Subgroup-L energy absorbed per gram is

$$\text{DAIX(L)} = \frac{\text{WU(L)} - \text{ERGU(L)} \times \text{SNR2(L)}}{(\rho/3) (R_{\text{out}}^3 - R_{\text{edge}}^3)} \left\{ 1 - e^{-\text{SUMOUT(L)}} \right\}$$

where SUMOUT(L) is computed just as in Case 1.

The energy available for hydro due to Subgroup L is computed just as in Case 1.

The total Group-U energy available for hydro in the cell portion outside the B-edge is, as in Case 1, the sum of that due to the five subgroups.

The weighted average of the values of the deposited energy available for hydro in the two portions of the cell is taken to be

$$\text{DAIXU}_{\text{average}} = \text{W1} \times \text{SPINT} + (1 - \text{W1}) \times \text{DAIXU}_{\text{total}}$$

where

$$\text{W1} = \left(R_{\text{edge}}^3 - R_{\text{in}}^3 \right) / \left(R_{\text{out}}^3 - R_{\text{in}}^3 \right) .$$

For the cell portion outside the B-edge, the effective photon fluences for Subgroup 1 and for Subgroups 2 through 5, consistent with the energy deposition, are computed just as in Case 1.

9.4.2 Pressure To Be Used for Hydro

In Subroutine PHEAT, the pressure computed from the equation of state $[p = (\gamma-1)\rho\epsilon]$ by using the total specific energy available for hydro from the deposition of the Group-X, -H, and -U energies, is currently interpreted as the total pressure. However, an electron pressure, $p_e \equiv n_e kT_e$, is implied by the computation in Subroutine PCHEM where a common temperature is found for the electron kinetic temperature, the N_2 vibrational temperature, and the $\text{O}(^1\text{D})$ -to- $\text{O}(^3\text{P})$ population ratio.

It is possible that a negative value for the heavy-particle temperature obtains when the electron pressure is subtracted from the total pressure. Our interim procedure in Subroutine PCHEM by which we insure no negative value for the heavy-particle temperature needs to be reviewed and improved.

As an interim measure we have adopted the HARC procedure for limiting the amount of specific energy when the various contributions are added to obtain SPINTN; however, the limiting term has not been derived and needs to be reviewed and improved. Another possible shortcoming is that the current procedure permits adding energy to a region within a B-edge for a previous event.

9.4.3 Flow Chart for Subroutine PHEAT

Figure 21 is a detailed flow chart for Subroutine PHEAT.

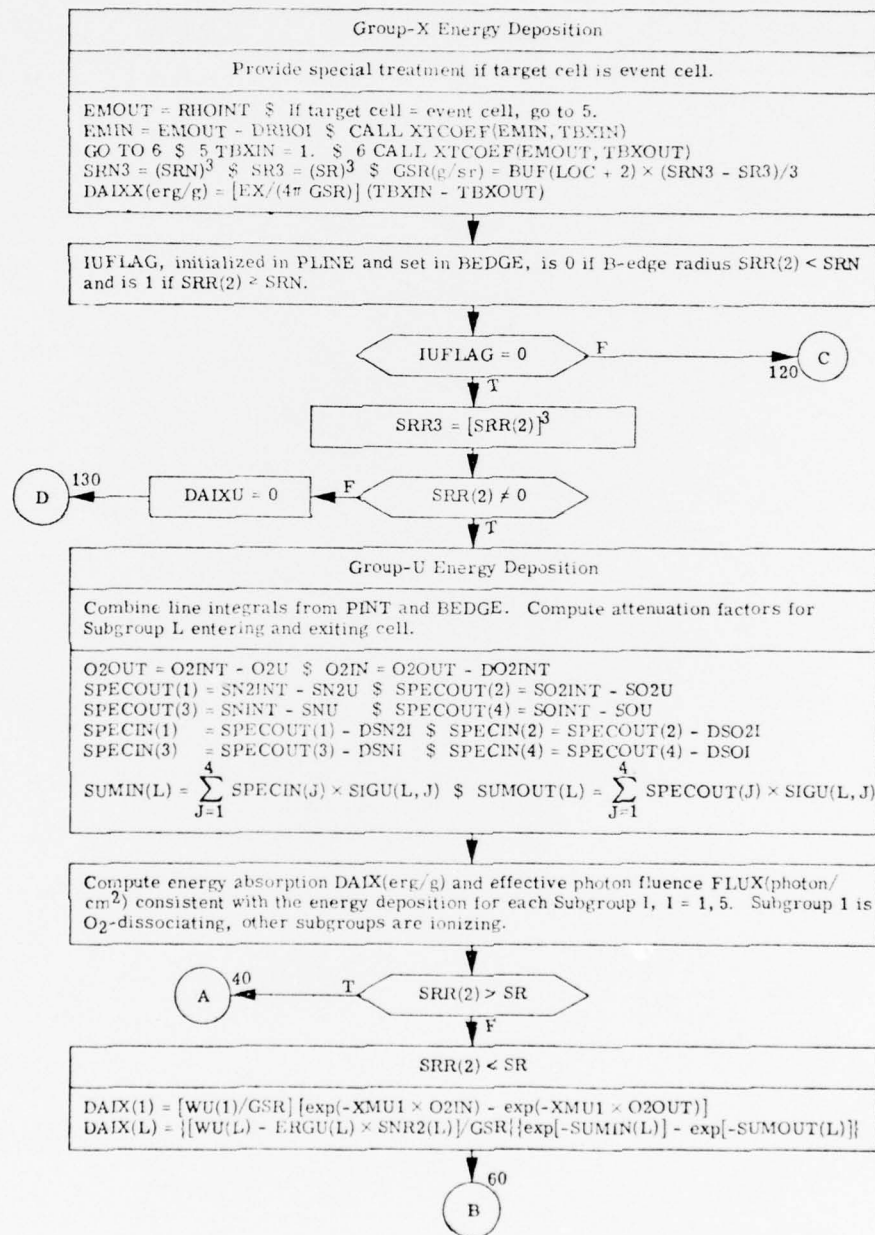


Fig. 21. Flow Chart of Subroutine PHEAT.

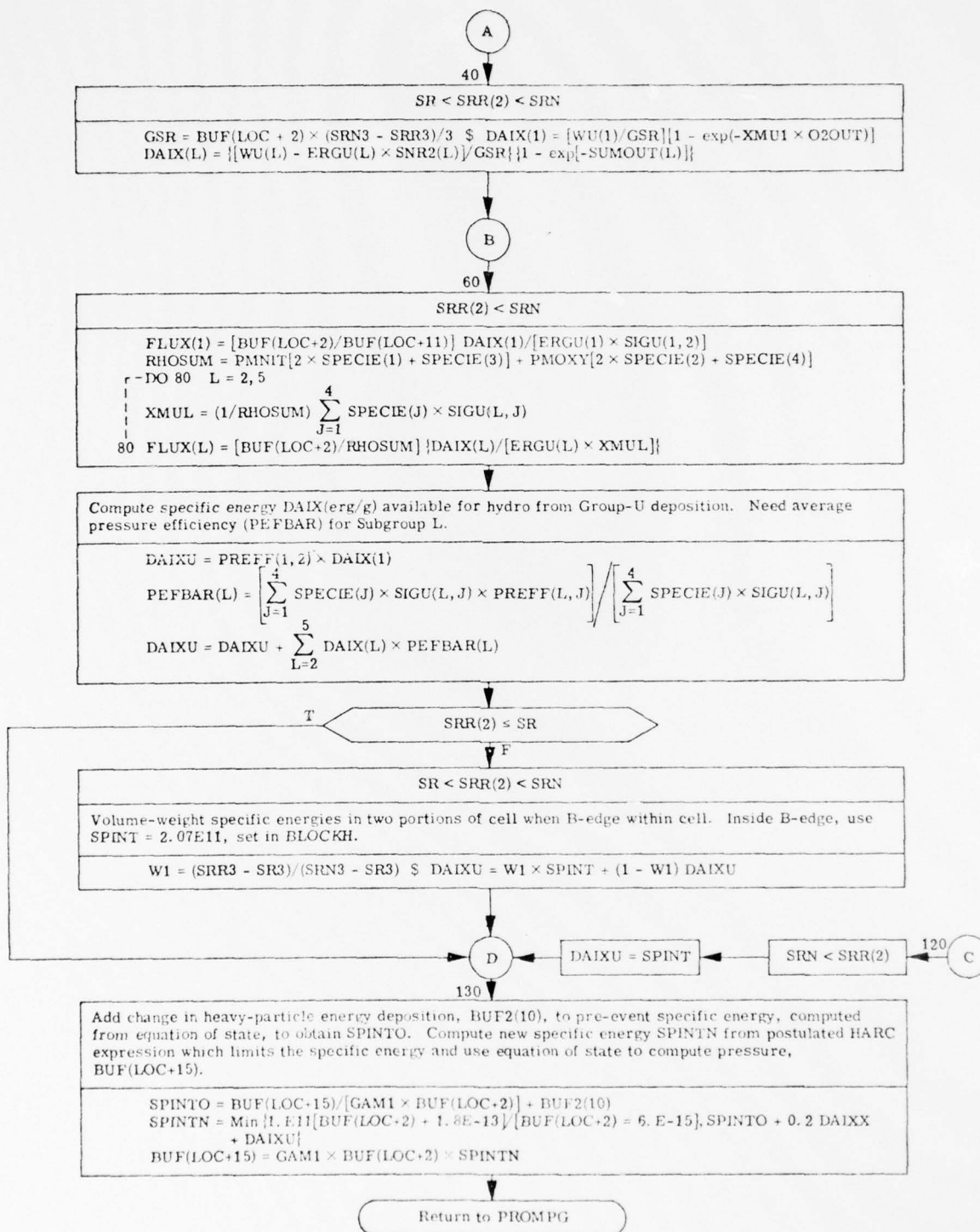


Fig. 21. (Continued).

10. PROMPT CHEMISTRY ASSOCIATED WITH GROUP-X AND GROUP-U ENERGY DEPOSITION (SUBROUTINE PCHEM)

Subroutine PCHEM first combines (a) the changes in species densities due to debris deposition, computed in Subroutine HPCHEM, with (b) the previous species densities of a cell and then computes the ionization and species densities from the Group-X and Group-U energy depositions.

Subroutine PCHEM contains numerous compromises and adjustments made necessary by using energy deposition models that are (a) instantaneous and (b) mismatched with the late-time chemistry modules.

10.1 DETERMINATION OF INITIAL SPECIES FOR COMPUTING THE PROMPT CHEMISTRY ASSOCIATED WITH GROUP-X AND GROUP-U ENERGY DEPOSITIONS

Before computing the prompt chemistry associated with the energy depositions of Groups X and U, we must combine the changes in species densities due to debris deposition with the previous species densities.

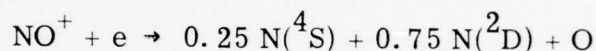
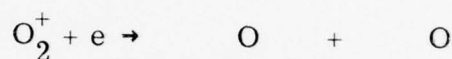
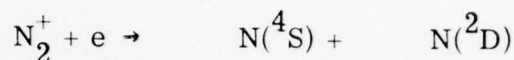
The changes in the species densities and electronic thermal and excitation energy are stored in the BUF2 array by Subroutine HPCHEM. These variables are defined in Table 3.

The incorporation of these changes may seem trivial, but it is complicated by the facts that (a) the late-time chemistry for the HAG treats all molecular ions as if they are NO^+ and (b) it is necessary to appropriately convert the N_2^+ and O_2^+ produced by the heavy-particle deposition into NO^+ . This conversion is made so as to conserve nuclei

Table 3. Inputs to Subroutine PCHEM from BUF2 Array for Those Cell Quantities Updated by Subroutine HPCHEM as a Result of Debris Deposition.

I	BUF2(I)	
1	Change in [e],	cm^{-3}
2	Change in $[\text{N}(^4\text{S})]$,	cm^{-3}
3	Change in $[\text{N}(^2\text{D})]$,	cm^{-3}
4	Change in [O],	cm^{-3}
5	Change in $[\text{N}_2]$,	cm^{-3}
6	Change in $[\text{O}_2]$,	cm^{-3}
7	Change in $[\text{N}^+]$,	cm^{-3}
8	Change in $[\text{O}^+]$,	cm^{-3}
9	Change in O excitation energy and electron thermal energy per new electron (eV/electron)	
10	Not used	
11	Change in $[\text{N}_2^+]$,	cm^{-3}
12	Change in $[\text{O}_2^+]$,	cm^{-3}

of a given mass number and electronic state but with only partial regard to energy considerations. The appropriate mass conversion coefficients are based on the same dissociative recombination products of N_2^+ , O_2^+ , and NO^+ used in the later treatment of Group-X and -U energy depositions. The assumed dissociative recombination products are as follows [Volume II]:



To illustrate this conversion process, we note that if we have a NO^+ molecular-ion density equal to $[N_2^+]$, the number of $N(^4S)$ atoms we get from dissociative recombination of NO^+ is only one-fourth as many as from dissociative recombination of N_2^+ . Thus, to the initial density of $N(^4S)$ we must add a number equal to $0.75[N_2^+]$. Similarly, if we have a NO^+ density equal to $[O_2^+]$, the number of $N(^4S)$ atoms we get from dissociative recombination of NO^+ is $0.25[NO^+]$ whereas we would get no $N(^4S)$ atoms from the dissociative recombination of $[O_2^+]$. Thus, to the initial density of $N(^4S)$ we must subtract a number equal to $0.25[O_2^+]$.

To prevent the density of $N(^4S)$, $N(^2D)$, or O from becoming negative as a result of converting N_2^+ and O_2^+ to NO^+ , we appropriately reduce either the N_2^+ or O_2^+ (produced by the heavy particles) and correspondingly increase N_2 or O_2 . Of course, the electron density must be reduced to maintain charge conservation when we reduce the density of either N_2^+ or O_2^+ .

More details of the steps in converting N_2^+ and O_2^+ to NO^+ are given on the first page of the flow chart for Subroutine PCHEM (Fig. 22).

We assume that $[CO_2]$ and $[He]$ are reduced by the debris deposition in proportion to the $[N_2]$ reduction.

10.2 IONIZATION AND SPECIES DENSITIES FROM GROUP-X DEPOSITION

Computation of the species densities from Group-X deposition is done very simply.

1. Use the specific energy absorbed from Group-X deposition ($DAIXX(\text{erg/g})$) computed in Subroutine PHEAT and the mass density ($RHO(\text{g/cm}^3)$) to get the corresponding energy density ($DELEX(\text{eV/cm}^3)$).
2. Assume 35-eV of energy is expended in forming an ion-pair.
3. Distribute the ions in proportion to the neutral species, but allow no more than one ion pair per neutral particle. Such a prescription is perhaps unduly simplistic in view of the considerable amount of information available concerning x-ray and electron energy degradation in the atmosphere (see, e.g., MS-75, SK-75, TA-74); however, no reliable prescription is yet available to predict the species for an arbitrary initial mix of species.
4. Assume the molecular ions undergo instantaneous dissociative recombination in accordance with the prescription in Section 10.1.
5. Assume that $[CO_2]$ and $[He]$ are reduced in proportion to the $[N_2]$ reduction.

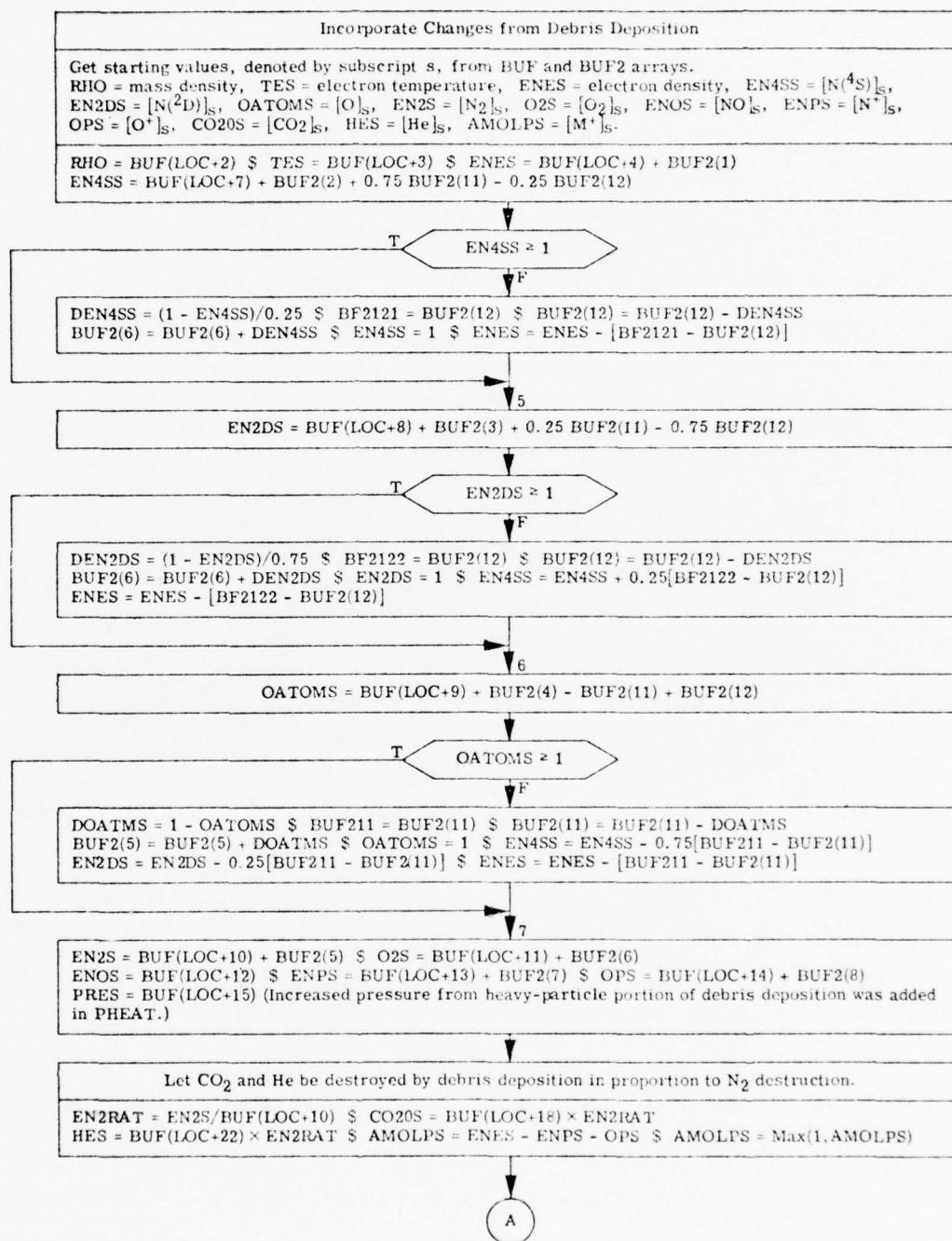


Fig. 22. Flow Chart of Subroutine PCHEM.

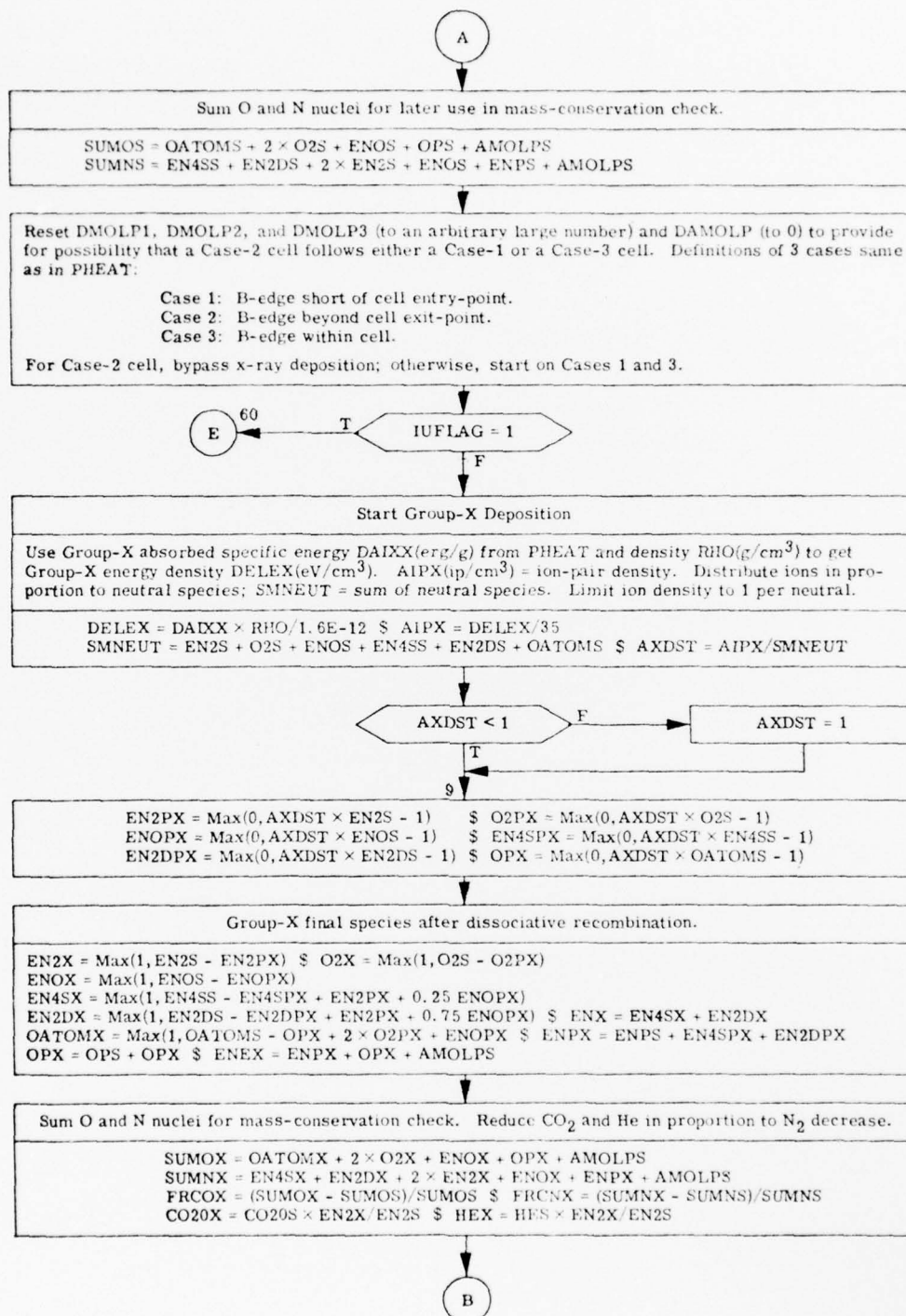


Fig. 22. (Continued).

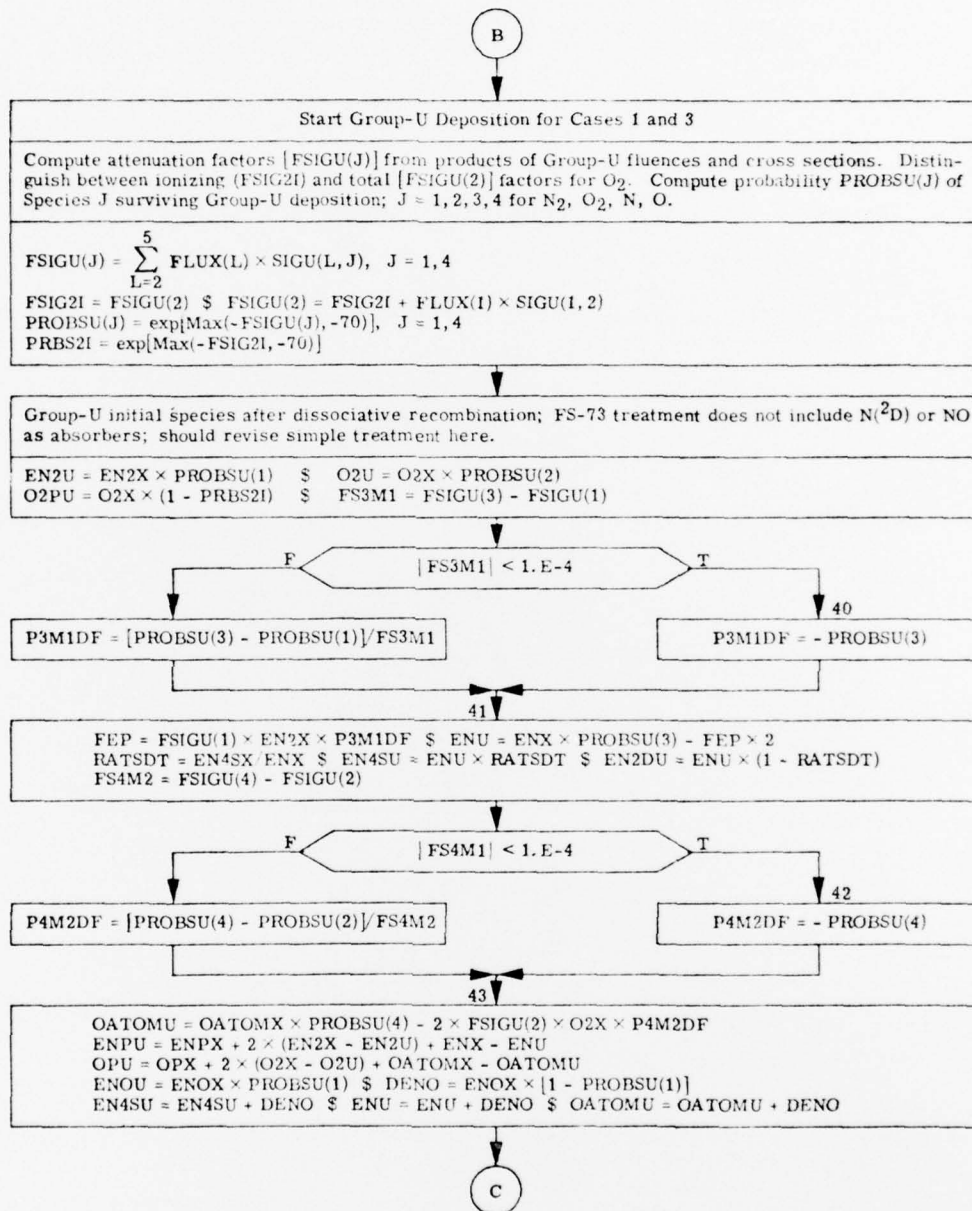


Fig. 22. (Continued).

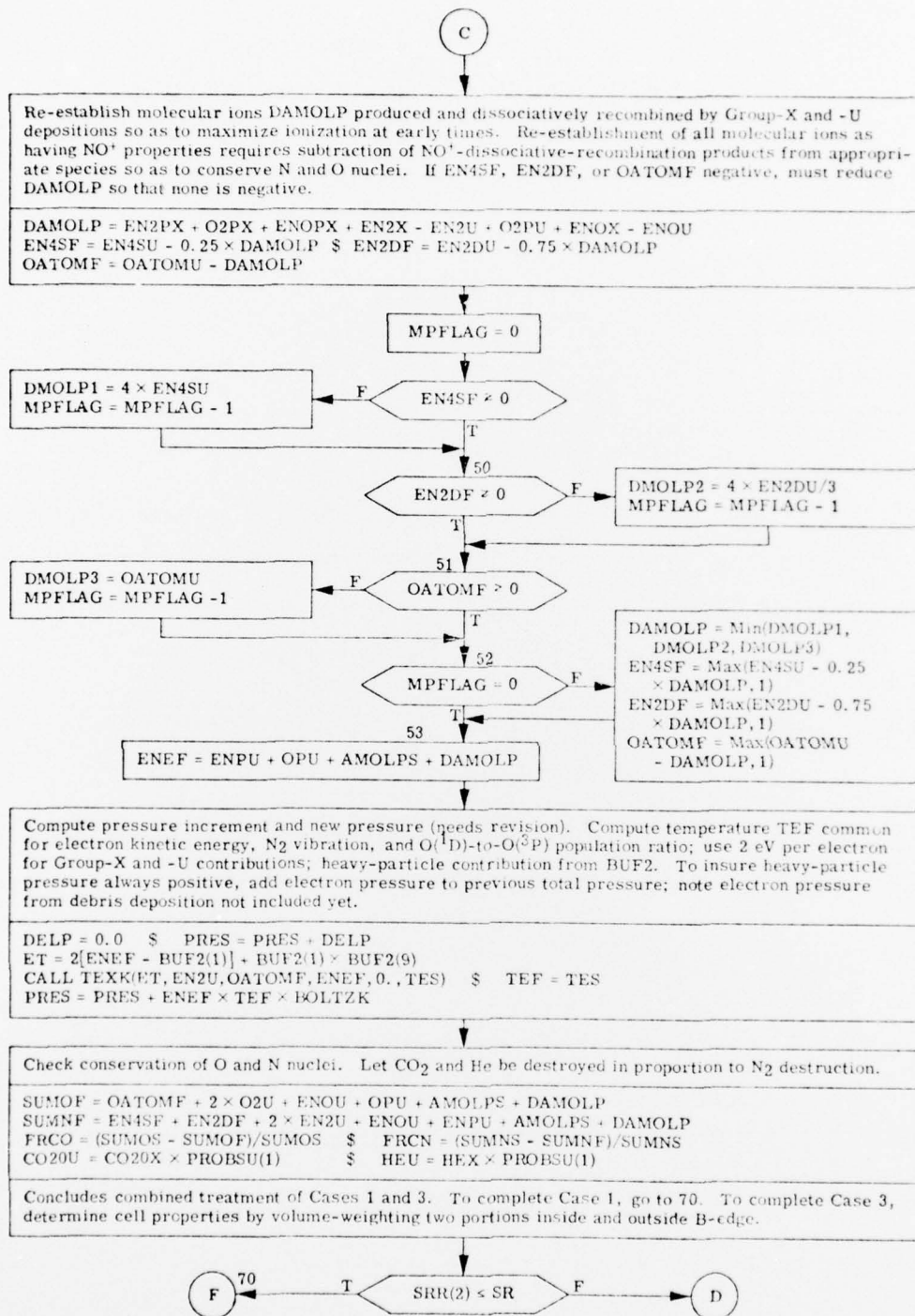


Fig. 22. (Continued).

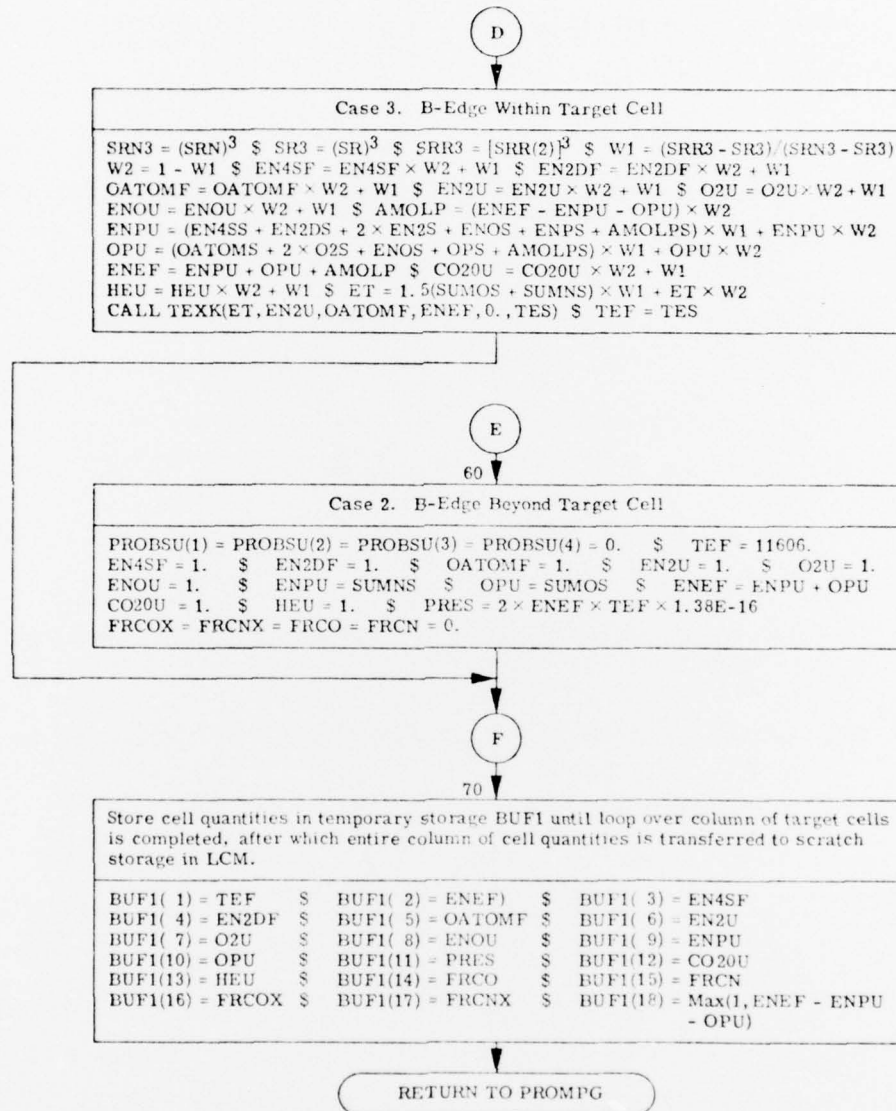


Fig. 22. (Continued).

As one of the mass conservation checks during development, we have compared the sums of the O and N nuclei after the computation of the species resulting from Group-X deposition with the sums before the deposition.

If the target cell is a Case-2 cell as defined in Section 9.4 and again below in Section 10.3, no computation is made of species resulting from Group-X deposition.

10.3 IONIZATION, SPECIES DENSITIES, AND RESULTANT PRESSURE FROM GROUP-U DEPOSITION

In computing the species from Group-U deposition, we consider three cases, just as we did in Subroutine PHEAT:

Case 1: B-edge radius (SRR(2)) is smaller than the target-cell entry radius (SR).

Case 2: B-edge radius (SRR(2)) is greater than the target-cell exit radius (SRN).

Case 3: B-edge radius (SRR(2)) is between the target-cell entry radius (SR) and the exit radius (SRN).

The total attenuation factors (FSIGU(J)) are computed from the summed products of Group-U fluences (FLUX(L), photons/cm²) and cross sections (SIGU(L, J), cm²). (Recall that the Group-U fluences computed in Subroutine PHEAT are effective fluences, consistent with the absorbed energy computed as the difference of the (steradianal) energy entering and leaving the cell.) The attenuation factors are

$$FSIGU(J) = \sum_{L=2}^5 FLUX(L) \times SIGU(L, J) , \quad J = 1, 4$$

$$FSIG2I = FSIGU(2)$$

$$\text{FSIGU}(2) = \text{FSIG2I} + \text{FLUX}(1) \times \text{SIGU}(1,2) ,$$

where $\text{SIGU}(L, J)$ is the absorption cross-section of Species J for Subgroup- L photons, tabulated in Table 4 and entered as data in Block Data BLOCKH, and where we have distinguished between the ionizing (FSIG2I) and total ($\text{FSIGU}(2)$) attenuation factors for O_2 .

The total survival probability of Species J is

$$\text{PROBSU}(J) = e^{-\text{FSIGU}(J)} .$$

The probability of O_2 not being ionized is

$$\text{PRBS2I} = e^{-\text{FSIG2I}} .$$

If the species densities after the Group- X deposition (but before the Group- U deposition) are denoted by a subscript x , the initial species after the Group- U deposition, with provision for instantaneous dissociative recombination of the molecular ions but without production of $\text{N}(^2\text{D})$, are [FS-73]

$$[\text{N}_2]_{\text{u}} = [\text{N}_2]_{\text{x}} \times \text{PROBSU}(1)$$

$$[\text{O}_2]_{\text{u}} = [\text{O}_2]_{\text{x}} \times \text{PROBSU}(2)$$

$$[\text{N}]_{\text{u}} = [\text{N}]_{\text{x}} \times \text{PROBSU}(3) + 2 \times [\text{N}_2]_{\text{x}} \times \text{FSIGU}(1) \times \frac{\text{PROBSU}(1) - \text{PROBSU}(3)}{\text{FSIGU}(3) - \text{FSIGU}(1)}$$

$$[\text{O}]_{\text{u}} = [\text{O}]_{\text{x}} \times \text{PROBSU}(4) + 2 \times [\text{O}_2]_{\text{x}} \times \text{FSIGU}(2) \times \frac{\text{PROBSU}(2) - \text{PROBSU}(4)}{\text{FSIGU}(4) - \text{FSIGU}(2)}$$

$$[\text{N}^+]_{\text{u}} = [\text{N}^+]_{\text{x}} + 2 \{ [\text{N}_2]_{\text{x}} - [\text{N}_2]_{\text{u}} \} + [\text{N}]_{\text{x}} - [\text{N}]_{\text{u}}$$

$$[\text{O}^+]_{\text{u}} = [\text{O}^+]_{\text{x}} + 2 \{ [\text{O}_2]_{\text{x}} - [\text{O}_2]_{\text{u}} \} + [\text{O}]_{\text{x}} - [\text{O}]_{\text{u}} .$$

Table 4. UV Absorption Cross-Sections $\text{SIGU}(L, J)^a$
(in units of 10^{-18} cm^2).

Species	J	$\text{SIGU}(L, J)$				
		L = 1 11.0 eV	L = 2 14.8 eV	L = 3 16.2 eV	L = 4 22.0 eV	L = 5 36.0 eV
N_2	1	0	8	20	25	20
O_2	2	2	16	20	25	20
N	3	0	10	10	10	10
O	4	0	3.2	3.2	9	9

^aFrom Table A-1 of FS-73, in turn from DD-70b.

Since the Group-U deposition procedure does not provide for either $\text{N}(^2\text{D})$ or NO , as an interim measure we partition the N atoms between $\text{N}(^4\text{S})$ and $\text{N}(^2\text{D})$ according to the prescription

$$[\text{N}(^4\text{S})]_{\text{u}} = [\text{N}]_{\text{u}} [\text{N}(^4\text{S})]_{\text{x}} / [\text{N}]_{\text{x}}$$

$$[\text{N}(^2\text{D})]_{\text{u}} = [\text{N}]_{\text{u}} \{1 - [\text{N}(^4\text{S})]_{\text{x}} / [\text{N}]_{\text{x}}\} ,$$

decrease the NO in proportion to the N_2 decrease, and increase N and O correspondingly:

$$[\text{NO}]_{\text{u}} = [\text{NO}]_{\text{x}} \times \text{PROBSU}(1)$$

$$\delta[\text{NO}] = [\text{NO}]_{\text{x}} \{1 - \text{PROBSU}(1)\}$$

$$[\text{N}(^4\text{S})]_{\text{u}} \rightarrow [\text{N}(^4\text{S})]_{\text{u}} + \delta[\text{NO}]$$

$$[\text{N}]_{\text{u}} \rightarrow [\text{N}]_{\text{u}} + \delta[\text{NO}]$$

$$[\text{O}]_{\text{u}} \rightarrow [\text{O}]_{\text{u}} + \delta[\text{NO}] .$$

To maximize the ionization at early time, as suggested by W. Knapp, we re-establish the molecular ions produced and dissociatively recombined by the Group-X and -U depositions (and allow the molecular ion decay to be predicted by the later-time chemistry module). The increment in such molecular ions is

$$\begin{aligned} \text{DAMOLP} \equiv \delta M^+ = & [N_2^+]_X + [O_2^+]_X + [NO^+]_X + [N_2]_X - [N_2]_u \\ & + [O_2^+]_u + [NO]_X - [NO]_u \end{aligned}$$

where

$$[O_2^+]_u = [O_2]_X (1 - \text{PRBS2I}) .$$

The re-establishment of all molecular ions as having the properties of NO^+ requires subtraction of all the products of NO^+ dissociative recombination from the appropriate species so as to conserve N and O nuclei:

$$[N(^4S)]_f = [N(^4S)]_u - 0.25 \times \delta M^+$$

$$[N(^2D)]_f = [N(^2D)]_u - 0.25 \times \delta M^+$$

$$[O]_f = [O]_u - \delta M^+ .$$

However, if $[N(^4S)]_f$, $[N(^2D)]_f$, or $[O]_f$ is negative, we must reduce δM^+ so that none of them is negative.

The final values for the species densities after Group-X and -U depositions and re-establishment of the molecular ions are $[N_2]_u$, $[O_2]_u$, $[NO]_u$, $[N(^4S)]_f$, $[N(^2D)]_f$, $[O]_f$, $[N^+]_u$, $[O^+]_u$, and $[e]$, the electron density,

$$[e] = [N^+]_u + [O^+]_u + \delta M^+ + M_S^+$$

where M_S^+ is the molecular-ion density prior to Group-X deposition.

There remains the task of devising a truly satisfactory procedure for computing a pressure increment in addition to that computed in Subroutine PHEAT. The treatment in Subroutine PHEAT is incomplete because the Group-U subgroups are deposited independently of each other across an appreciable path length without accounting for either species depletion by other subgroups or additional absorbers resulting from the (instantaneous) dissociative recombination that is included in Subroutine PCHEM. (Note, however, that the partial heating computed in Subroutine PHEAT does serve the purpose of defining effective fluences for the Group-U subgroups that are used in Subroutine PCHEM.) Any additional pressure increment computed in Subroutine PCHEM must be consistent with (1) that computed in Subroutine PHEAT and with (2) the return of pressure computed by the later-time chemistry in CHEMEF. The problem is further complicated because the molecular ions which are produced by the Group-X and -U depositions and which undergo dissociative recombination as part of the modeling in Subroutine PCHEM are N_2^+ and O_2^+ whereas the molecular ions that are re-established are NO^+ ions which are carried in CHEMEF. As an interim measure we set the pressure increment DELP equal to zero.

To ensure that the heavy-particle pressure will always be positive, we have added the electron pressure (computed below) to the previously-found value for the total pressure. This interim measure needs to be reviewed and improved.

To compute the temperature TEF taken to be common to the thermal electrons, the N_2 vibrational states, and the $O(^1D)$ -to- $O(^3P)$ population ratio, we use the GET-prepared Subroutine TEXK [Vol. 11] which determines such a temperature when given $[N_2]$, $[O]$,

[e], and the energy per cubic centimeter (ET) to be divided among the three modes. As an interim measure we compute ET from

$$ET = 2 \times \delta[e]_{x,u} + \delta[e]_{HP} \times E_{pe}$$

where $\delta[e]_{x,u}$ is the incremental electron density produced by the Group-X and -U depositions, the factor 2 is an interim assumption for the energy in the three modes per newly-formed electron in the Group-X and -U depositions, $\delta[e]_{HP}$ is the incremental electron density produced by the heavy-particle depositions, and E_{pe} is the sum of the electron thermal and O(¹D) excitation energies per newly-formed electron in the heavy-particle deposition, obtained from Subroutine HPCHEM.

As another of the mass conservation checks during development, we have compared the sums of the O and N nuclei after the computation of the species resulting from Group-U deposition with the sums before the deposition.

As with the Group-X deposition, we assume as an interim measure that [CO₂] and [He] are reduced in proportion to the [N₂] decrease.

The foregoing describes the combined treatment of target cells that are Case 1 or Case 3. For Case 1, the treatment is complete, but for Case 3, the final cell properties are determined by volume-weighting the two portions, one of which is inside the B-edge and the other is outside the B-edge.

For Case 2, the entire cell is inside the B-edge and the only remaining species are assumed to be N⁺, O⁺, and e. The temperature of both electrons and heavy particles is taken to be 1 eV.

The final step in Subroutine PCHEM is to store the cell quantities in temporary storage BUF1 until the loop over the entire column of target cells is completed, after which the entire column of cell quantities is transferred to scratch storage in large-core memory.

11. REFERENCES

- CI-65 CIRA 1965, COSPAR International Reference Atmosphere 1965, North-Holland Publishing Co., Amsterdam, 1965.
- DD-70b T. N. Delmer, E. P. dePlomb, et al., Effects of High Altitude Nuclear Explosions (U), DASA 2593 [Gulf Radiation Technology Gulf-RT-11010], 28 October 1970, (S/RD). ✓
- FS-71a F. E. Fajen and D. Sappenfield, Single-Burst Weapon Effects Calculations for Altitudes Between 97 and 250 km (U), Los Alamos Scientific Laboratory Report LA-4606, June 1971, (S/FRD). ✓
- FS-73 F. E. Fajen, D. S. Sappenfield, R. W. Moore, Studies in High-Altitude Weapon Phenomenology (U), DNA 3100T [MRC-R-48], June 1973, (S/FRD). ✓
- GE-70 General Electric TEMPO, RANC IV. Computer Simulation of Radar Propagation in a Nuclear Environment (U), Vol. I, Computational Models, DASA 2497-1 [70TMP-37], July 1970, (C/FRD). ✓
- HL-71 D. A. Hamlin, R. W. Lowen, B. F. Myers, M. R. Schoonover, and J. I. Valerio, Deionization Chemistry of the Disturbed E- and F-Regions (U), DNA 2724, September 1971, (S/FRD). ✓
- HL-73b D. A. Hamlin, R. W. Lowen, B. F. Myers, M. R. Schoonover, and J. I. Valerio, Theoretical High-Altitude Nuclear-Explosion Studies, Vol. 2: Resonance Trapping, Deposition, and Resulting Chemistry of Ultraviolet Radiation; Energy Deposition of Heavy Particles, DNA 3216F-2 [SAI-73-220-LJ], 15 May 1974, (U).
- HM-72b D. A. Hamlin, B. F. Myers, and M. R. Schoonover, Studies of High-Altitude Nuclear-Induced Optical-Infrared Radiation (U), DNA 3012F [SAI-72-238-LJ], February 1973, (S/RD). ✓
- LS-63 J. Lindhard, M. Scharff, and H. E. Schiott, Range Concepts and Heavy Ion Ranges, Mat. Fys. Medd. Dan. Vid. Selsk. 33, No. 14 (1963).

- MS-75 B. F. Myers and M. R. Schoonover, Electron Energy Degradation in the Atmosphere: Consequent Species and Energy Densities, Electron-Flux and Radiation Spectra, DNA 3513T [SAI-74-619-LJ], 3 January 1975, (U).
- SK-75 T. L. Stephens and A. L. Klein, Electron Energy Deposition in the Atmosphere, Vol. I, GE TEMPO Report GE75TMP-7, May 1975.
- TA-74 P. W. Tarr, D. H. Archer, and N. G. Utterback, Studies of Auroral Simulation, DNA 3297F [MRC-R-122], 11 April 1974.

DISTRIBUTION LIST

DEPARTMENT OF DEFENSE

Director
Defense Advanced Research Proj. Agency
ATTN: STO

Defense Communication Engineer Center
ATTN: Code R410, James W. McLean

Director
Defense Communications Agency
ATTN: Code 480

Defense Documentation Center
Cameron Station
12 cy ATTN: TC

Director
Defense Nuclear Agency
ATTN: DDST
ATTN: TISI, Archives
3 cy ATTN: TITL, Tech. Library
ATTN: RAAF

Dir. of Defense Research & Engineering
Department of Defense
ATTN: S&SS (OS)

Commander
Field Command
Defense Nuclear Agency
ATTN: FCPR

Director
Interservice Nuclear Weapons School
ATTN: Document Control

Director
Joint Strat. Target Planning Staff, JCS
ATTN: JPST, Captain G. D. Goetz

Chief
Livermore Division, Field Command, DNA
Lawrence Livermore Laboratory
ATTN: FCPRL

DEPARTMENT OF THE ARMY

Commander/Director
Atmospheric Sciences Laboratory
US Army Electronics Command
ATTN: DRSEL-BL-SY-S, F. E. Niles

Director
BMD Advanced Tech. Center
2 cy ATTN: ATC-T, Melvin T. Capps

Commander
Harry Diamond Laboratories
ATTN: DRXDO-NP, Francis N. Wimenitz
ATTN: DRXDO-TI

Director
TRASANA
ATTN: R. E. DeKinder, Jr.

DEPARTMENT OF THE ARMY (Continued)

Director
US Army Ballistic Research Labs.
ATTN: Lawrence J. Puckett
ATTN: Mark D. Kregel

Commander
US Army Foreign Science & Tech. Center
ATTN: P. A. Crowley

Commander
US Army Missile Intell. Agency
ATTN: Jim Gamble

Commander
US Army Missile Command
ATTN: DRSMI-XS, Chief Scientist

Commander
US Army Nuclear Agency
ATTN: MONA-WE, J. Berberet

DEPARTMENT OF THE NAVY

Chief of Naval Operations
Navy Department
ATTN: Alexander Brandt

Commander
Naval Ocean Systems Center
3 cy ATTN: Code 2200, Verne E. Hildebrand

Director
Naval Research Laboratory
3 cy ATTN: Code 7701, Jack D. Brown
ATTN: Code 7750, S. Ossakow

Commander
Naval Surface Weapons Center
ATTN: Code WA501, Navy Nuc. Prgms. Off.
ATTN: Code WX21, Tech. Lib.

Director
Strategic Systems Project Office
Navy Department
ATTN: NSSP-2722, Fred Wimberly
ATTN: NSP-2722, Marcus Meserole

DEPARTMENT OF THE AIR FORCE

AF Geophysics Laboratory, AFSC
ATTN: OPR, James C. Ulwick
ATTN: OPR, Alva T. Stair
ATTN: OPR, Harold Gardner

AF Weapons Laboratory, AFSC
ATTN: NSS, John M. Kamm
ATTN: SUL
ATTN: DYT, Capt Mark A. Fry
ATTN: DYT, Capt L. Wittwer
ATTN: DYT, Peter W. Lunn

Hq. USAF/RD
ATTN: RDQSM

DEPARTMENT OF THE AIR FORCE (Continued)

Commander
Rome Air Development Center, AFSC
ATTN: EMTLD, Doc. Library

SAMSO/SZ
ATTN: SZJ, Major Lawrence Doan

Commander in Chief
Strategic Air Command
ATTN: ADWATE, Capt Bruce Bauer
ATTN: XPFS, Maj Brian G. Stephan

Hq. USAF/SA
ATTN: AFSA, Capt Henkle

ENERGY RESEARCH & DEVELOPMENT ADMINISTRATION

University of California
Lawrence Livermore Laboratory
ATTN: Ralph S. Hager, L-31
ATTN: Donald R. Dunn, L-156

Los Alamos Scientific Laboratory
ATTN: Doc. Con. for John Zinn
ATTN: Doc. Con. for Eric Jones

OTHER GOVERNMENT AGENCIES

Department of Commerce
Office of Telecommunications
Institute for Telecom Science
ATTN: William F. Utlaut

DEPARTMENT OF DEFENSE CONTRACTORS

Aerospace Corporation
ATTN: Norman D. Stockwell
ATTN: Doug Rawcliffe

Brown Engineering Company, Inc.
ATTN: James E. Cato
ATTN: Romeo Deliberis
ATTN: Joel D. Bigley

ESL, Inc.
ATTN: James Marshall
ATTN: C. Prettie

General Electric Company
TEMPO-Center for Advanced Studies
ATTN: Warren S. Knapp
ATTN: Tim Stephens
ATTN: DASIAC

General Research Corporation
ATTN: John Ise, Jr.
ATTN: Joel Garbarino

Jaycor
ATTN: S. R. Goldman

Johns Hopkins University
Applied Physics Laboratory
ATTN: Document Librarian

DEPARTMENT OF DEFENSE CONTRACTORS (Continued)

Lockheed Missiles & Space Company, Inc.
ATTN: D. R. Churchill

M.I.T. Lincoln Laboratory
ATTN: Lib. A-082 for David M. Towle

Martin Marietta Aerospace
Orlando Division
ATTN: Roy W. Heffner

Mission Research Corporation
ATTN: D. Sappenfield
ATTN: R. Bogusch
ATTN: R. Hendrick
ATTN: Russell Christian

Physical Dynamics, Inc.
ATTN: Joseph B. Workman

R & D Associates
ATTN: Bryan Gabbard
ATTN: Robert E. LeLevier

Science Applications, Inc.
ATTN: D. Sachs
ATTN: Curtis A. Smith
ATTN: Daniel A. Hamlin
ATTN: Jon Y. Wang
ATTN: John I. Valerio
ATTN: Melvin R. Schoonover

Science Applications, Inc.
ATTN: B. F. Myers

Science Applications, Inc.
Huntsville Division
ATTN: Dale H. Divis
ATTN: Noel R. Byrn

Stanford Research Institute
ATTN: Ray L. Leadabrand
ATTN: Walter G. Chestnut

VisiDyne, Inc.
ATTN: J. W. Carpenter
ATTN: Charles Humphrey

